Solar High Temperature Water-Splitting Cycle with Quantum Boost

Final Report

Project Period:	9/1/2007 – 1/31/2014
Date of Report:	April 25, 2014
Recipient:	Science Applications International Corp. (SAIC)
Award Number:	DE-FG36-07GO17002
Working Partners:	Electrosynthesis Company, Inc (ESC) Thermochemical Engineering Solutions (TCHEME) University of California, San Diego (UCSD) Florida Solar Energy Center (FSEC) of the University of Central Florida
Cost-Sharing Partners:	SAIC, ESC, TCHEME, UCSD, Southern California Gas Co., FSEC
Principal Investigator:	Rob Taylor, SAIC, 858 826-9124, taylorro@leidos.com
DOE Managers:	Sara Dillich - DOE HQ Technology Manager, Wash., D.C. Katie Randolph - DOE Field Project Officer, Golden, CO
Authors:	Rob Taylor, Roger Davenport - SAIC David Genders, Peter Symons – ESC Jan Talbot, Richard Herz – UCSD Lloyd Brown – TCHEME

Table of Contents

List of Tables

List of Figures

1 Executive Summary

A variation of the hybrid sulfur thermochemical water splitting cycle (*aka* the "Hybrid Sulfur," or "HyS" cycle) was developed by introducing ammonia as a working reagent (thus "sulfur-ammonia," or "SA," cycle) to allow more efficient solar interface and facile product separation steps. The thermochemical cycle SA process was originally developed by the Florida Solar Energy Center [1, 2, 3, 4]. Several variations of the basic SA cycle have been evaluated, both conceptually and experimentally.

Two approaches were considered for the hydrogen production step of the SA cycle: (1) photocatalytic, and (2) electrolytic oxidation of ammonium sulfite to ammonium sulfate in aqueous solutions. Also, two sub-cycles were evaluated for the oxygen evolution side of the SA cycle: (1) zinc sulfate/zinc oxide, and (2) potassium sulfate/potassium pyrosulfate. The laboratory testing and optimization of all the process steps for each version of the SA cycle were then carried out.

The first version of the SA cycle employed a photocatalytic reaction step for generating hydrogen and a zinc sulfate/zinc oxide sub-cycle for oxygen generation as follows:

$SO_{2(g)} + 2NH_{3(g)} + H_2O_{(l)} \rightarrow (NH_4)_2SO_{3(aq)}$	(1 - chemical absorption)	25°C
$(NH_4)_2SO_{3(aq)} + H_2O_{(l)} \rightarrow (NH_4)_2SO_{4(aq)} + H_2$	(2 - solar photocatalytic)	80°C
$(NH_4)_2SO_{4(s)} + ZnO_{(s)} \rightarrow 2NH_{3(g)} + ZnSO_{4(s)} + H_2O$	(3 - solar thermocatalytic)	500°C
$ZnSO_{4(s)} \rightarrow SO_{2(g)} + ZnO_{(s)} + ½O_2$	(4 - solar thermocatalytic)	950°C

Later, an electrolytic approach was adopted in lieu of the photocatalytic step for the oxidation of aqueous ammonium sulfite as the hydrogen production half cycle. Additionally, an all-liquid potassium sulfate/potassium pyrosulfate sub-cycle was identified for the high-temperature portion. The reactions for the present cycle are presented below, and **Figure 1** shows a schematic of the electrolytic SA cycle presently being examined.

$SO_{2(}g) + 2NH_3(g) + H_2O(l) \rightarrow (NH_4)_2SO_3(aq)$	(1 - chemical absorption)	25-50 °C
$(NH_4)_2SO_3(aq) + H_2O(l) \rightarrow (NH_4)_2SO_4(aq) + H_2$	(2 - electrolytic)	80-150 °C
$(NH4)_2SO_4(aq) + K_2SO_4(l) \rightarrow 2NH_3(g) + K_2S_2O_7(l) + H_2O(g)$	(3 – adiabatic mixing)	400-450 °C
$K_2S_2O_7(l) \rightarrow SO_3(g) + K_2SO_4(l)$	(4 – stored thermal)	790 °C
$SO3(_{g)} \rightarrow SO_{2(g)} + ½O_{2(g)}$	(5 – electric heat)	850-1,200 °C

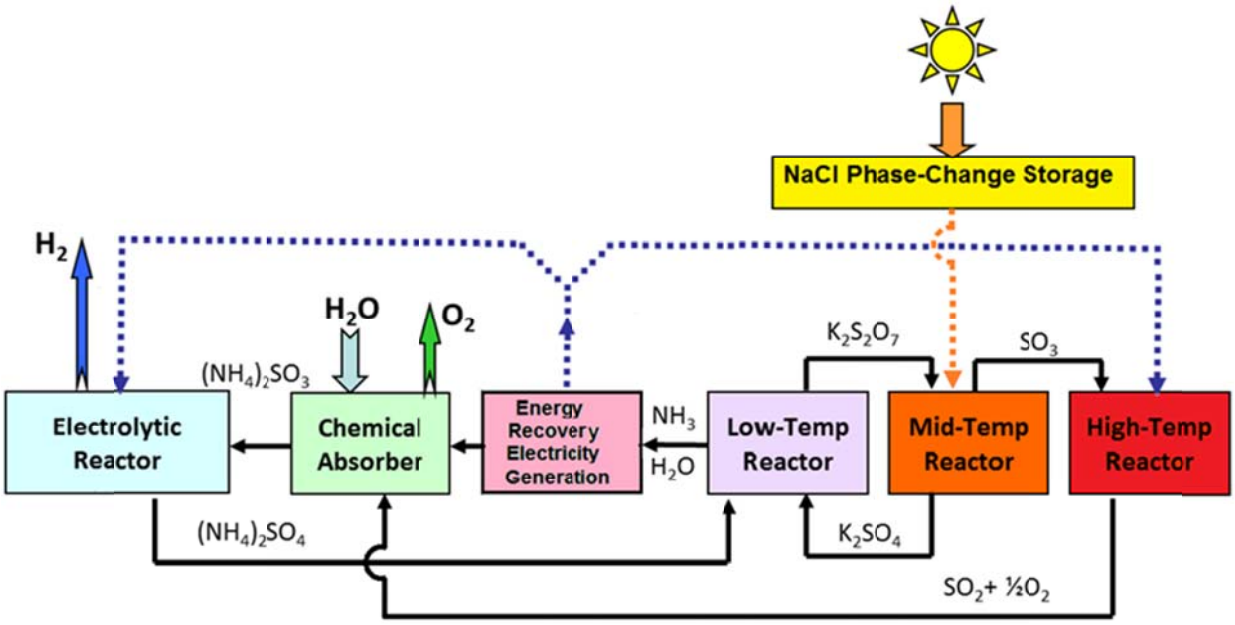

Figure 1. Schematic of the Electrolytic SA Cycle

1.1 Understanding of the Area Investigated

This nation currently produces hydrogen primarily from natural gas. The value to our nation from the implementation of hydrogen fuel cell vehicles is well documented. In order to ensure a sustainable, renewable, and environmentally beneficial source of hydrogen, a cost-effective water splitting process is a primary approach to meet these needs. The SA cycle is a moderate to high risk technology with high potential pay-off. Industry has been focused on short term solutions that are not sustainable, renewable, or environmentally beneficial. All of the competing technologies for producing hydrogen with solar water splitting processes have the challenge of meeting the cost goals primarily due to the cost of the solar central receiver system. Most of the competing technologies have longer term horizons for reaching commercialization and cost effectiveness than does the SA cycle. It can operate at a relatively low solar receiver temperature (800°C), generate all electricity needed internally, and operate continuously (24/7) with low-cost storage. Some competing technologies require direct solar energy input into chemically reacting solids at high temperatures (>1200°C). It is not apparent that these systems can be scaled up beyond the tens of kilowatt stage due to the difficulties in moving high temperature solids. Other processes require that the solar energy be directly transferred to chemically reacting gases thus requiring large scale heat transfer to be accomplished atop a solar power tower with the large radiant energy losses accompanying large aperture high temperature solar receivers. Only the SA process employs boiling heat transfer allowing small aperture high temperature solar receivers.

1.2 Technical Effectiveness & Economic Feasibility

The SA thermochemical cycle splits water into hydrogen and oxygen via three chemical reactions and three chemisorption steps. This all-fluid process is unique in that it operates at steady state around the clock when coupled to a sodium chloride phase change thermal energy storage system. Since the chemical plant operates continuously, excluding the energy storage system, it is one-third the size of a plant that operates only when the sun shines. Moreover, steady state operation requires only half the operating staff of a plant that is always starting up and shutting down to follow the availability of solar energy. The projected cost of hydrogen from the proposed modified S-A process is $10.91/kg in 2015 and down 35% by 2025 to $7.04/kg. To reach DOE target costs several actions will be needed including simplification of the chemical plant through implementation of a lower-water configuration with molten salt electrolysis. The electrolysis process conditions will need to be improved from present values, with reduction in the voltage needed as well as savings in the cost of membranes and other equipment. The amount of voltage reduction is difficult to specify because it is dependent on many other factors including the success in reducing the amount of water that needs to be vaporized. Finally, the solar field cost will need to decrease due to improvements and commercial implementation of heliostat systems that are now ongoing (e.g., the BrightSource Energy and SolarReserve, LLC central receiver plants recently constructed in California) [5].

1.3 Benefit to the Public

The SA Process for hydrogen production has the potential to benefit the public by offering an economically viable, renewable, and carbon-free means of producing hydrogen with no foreign imports of energy. The U.S. Department of Energy began the Hydrogen Fuel Initiative in 2003 with the objective of commercializing hydrogen fuel cell vehicles by 2020. The motivation for producing hydrogen on a large scale is that it can reduce our dependence on imported oil and benefit the environment by reducing greenhouse gas emissions and criteria pollutant emissions that affect our air quality. If the SA process becomes technically and economically commercial, it will provide the public with a sustainable, renewable and environmentally beneficial new source of energy that can be supplied from resources completely within the U.S. at competitive prices.

2 Project Objectives

This program was designed as a three-phase program of research and development leading to demonstration of a cost-effective high-temperature water splitting cycle for hydrogen production using concentrated solar energy. A unique aspect of this project was the goal to identify, if possible, a solar-driven water-splitting cycle that utilized not only the thermal component of the solar radiation, but also the quantum energy of the solar photons. So, a review of the thermochemical and economic characteristics of potential solar-driven water-splitting cycles was conducted, specifically considering photocatalytic and electrolytic options for the hydrogen generation step. The goal was to identify a process generating hydrogen that would meet DOE's solar high temperature H_2 production efficiency and cost goals.

After evaluation, a cycle was selected and bench-scale experiments and analysis were conducted to determine the technical feasibility of the selected cycle. As the cycle evolved, the performance of the system was evaluated using the Aspen Plus™ chemical process simulator, and economic parameters of the system were determined using the H2A economic analysis program. Demonstration of a fully-integrated pilot-scale solar H_2 production unit was planned.

2.1 Goals and Objectives

The overall objectives of the project were:

- Prove the viability of a sulfur family thermochemical water-splitting cycle for large-scale hydrogen production using solar energy
- Evaluate sulfur ammonia (SA) water-splitting cycles that employ photocatalytic (quantum boost) or electrolytic hydrogen evolution steps and perform lab testing to demonstrate feasibility of the chemistry
- Perform economic analyses of SA cycles as they evolve to document their progress toward target cost goals
- Develop a cycle that has high potential for meeting the DOE threshold cost goal of $2-4/kg and solar to hydrogen energy conversion ultimate target of 26%

Recent specific objectives were:

- Improve electrolytic H_2 production by developing better anode electrocatalysts to facilitate operation at lower temperatures (80°C) while maintaining low voltage (< 0.8V) and/or identifying alternate membranes that can operate at higher temperature (up to 130°C) to take advantage of the lower thermochemical potential at higher temperature, but without an unacceptably high flux of sulfite across the membrane (<0.1 mmole/m^2/s)
- Demonstrate the molten salt is liquid and will flow (low viscosity) so it is easily pumped
- Demonstrate the NH_3 can be separated from the SO_3 by thermal decomposition thus avoiding potentially uneconomic gas separation processes

- Use the Aspen Plus® modeling tool to optimize systems for input to the H2A economic model. Evaluate using excess electricity production to produce heat for SO_3 decomposition. Evaluate power recovery and electrical power generation alternatives
- Perform technical and economic analyses of the SA cycle systems with and without a high temperature storage system that would allow for 24/7 operation

2.2 Accomplishments

The SAIC team made significant progress toward developing a cost-effective and efficient hydrogen production technology based on a solar thermochemical water-splitting cycle. The SA cycle having ammonia as the working fluid and reagent was developed. The long term stability of the complete electrochemical system was demonstrated with a 500+ hour extended run. New membranes were identified with up to two orders of magnitude lower sulfite fluxes (the lowest flux measured to date for a used membrane was 9.2 μmol/m^2/sec – see **Table 5**). This project has also achieved a 43% reduction in cell voltage (down to 0.8V at 100 mA/cm^2) through a combination of electrocatalyst, membrane and cell design improvements.

The high-temperature oxygen generation step is an all fluid process requiring no solid particle handling. Lab tests prove the sub-cycle feasibility. The NH_3 and SO_3 can be evolved separately without complicated membrane separation. A lower salt melting temperature of 373°C was achieved and the molten salts were demonstrated to have low enough viscosity (<8 cP) to be pumped. The decomposition of SO_3 is proven technology. The entire process consists of elementary chemical engineering unit operations that have been in widespread industrial use for over 100 years.

Aspen Plus® process modeling was used to significantly optimize the SA process. Due to the variability of solar energy, a phase-change thermal-storage system with NaCl was incorporated allowing continuous plant operation at 790°C. Rankine power cycles were designed to recover excess heat to efficiently generate electricity. The solar configuration is focused on a modular 50 MW(thermal) central receiver system with NaCl molten salt storage to allow continuous operation. Parametric studies of chemical plant performance have indicated efficiencies of ~20% [6] and identified areas for further research and study for future improvements to the cycle. The H2A economic model was used to optimize and trade-off SA cycle configurations. The projected cost of hydrogen from the proposed modified S-A process is $10.91/kg in 2015 and down 35% by 2025 to $7.04/kg. To reach DOE target costs, the chemical plant needs simplification through implementation of a lower-water configuration with molten salt electrolysis. The electrolysis process conditions will also need to be improved from present values, with reduction in the voltage needed as well as savings in the cost of membranes and other equipment. Finally, the solar field will need to decrease in cost.

3 Project Activities and Results

The following table summarizes some highlights of the project, which started in September 2007.

Table 1. Project Highlights

September 2007	Program Start - FSEC proposed Sulfur-Ammonia Cycle with photocatalytic hydrogen step and SO_2 decomposition
November 2007	ZnO subcycle proposed to simplify NH_3/SO_3 separation and oxygen production step
February 2008	Low-cost glass reinforced concrete (GRC) heliostat proposed
October 2008	Electrolytic hydrogen step proposed
September 2009	Electrical heating of SO_3 reactor proposed
December 2009	K_2SO_4 subcycle proposed to make process all-fluid
October 2010	After administrative delays, project continued with modified team (UCSD replaced FSEC)
September 2011	Modular 50 MW_{th} solar field/plant proposed
March 2012	High-temperature phase-change salt storage proposed
July 2012	SoCalGas added to team as cost-sharing partner
August 2012	Completion of 500 hour electrolysis test
January 2014	Project end

When the project began, a solar thermochemical process was proposed that included a photocatalytic hydrogen production step with ammonium sulfite being oxidized to ammonium sulfate in an aqueous solution using a CdS photocatalyst. This step was followed by a thermal decomposition of the ammonium sulfate to ammonia and sulfur trioxide, and then a decomposition of the sulfur trioxide to release the oxygen and form sulfur dioxide. Finally, the ammonia, sulfur dioxide, and water were recycled into the process and mixed together to re-create the aqueous ammonium sulfite solution. Solar energy was used in the form of photons to activate the photocatalyst, and in the form of heat to thermally decompose the other chemicals.

Following project initiation, a modification was proposed in order to simplify the gas separations. By reacting the ammonium sulfate with solid ZnO, $ZnSO_4$ would be formed and the water vapor and ammonia would separate easily from the solid material. Then, the $ZnSO_4$ was thermally decomposed at higher temperature back to ZnO, releasing SO_3 gas which again would separate easily from the solid material. Finally, the SO_3 was decomposed to SO_2 and oxygen in an even higher-temperature (e.g., 900-1200°C) reactor. The resulting Sulfur-Ammonia (SA) process is summarized in the following table:

Table 2. Sulfur-Ammonia Cycle with Photocatalytic Hydrogen Production

Reaction	Description	Temperature Range
$SO_{2(g)} + 2NH_{3(g)} + H_2O_{(l)} \rightarrow (NH_4)_2SO_{3(aq)}$	Chemical Absorption	25°C
$(NH_4)_2SO_{3(aq)} + H_2O_{(l)} \rightarrow (NH_4)_2SO_{4(aq)} + H_2$	Solar Photocatalytic	80°C
$(NH_4)_2SO_{4(s)} + ZnO_{(s)} \rightarrow 2NH_{3(g)} + ZnSO_{4(s)} + H_2O$	Solar Thermocatalytic	500°C
$ZnSO_{4(s)} \rightarrow SO_{2(g)} + ZnO_{(s)} + ½O_2$	Solar Thermocatalytic	950°C

Appropriate solar configurations for the process were developed. Initial investigations suggested dish concentrators could be used to achieve high efficiency at the high temperatures envisioned for the process, but it soon became clear that the complexity and scale of the chemical plant favored a heliostat field approach. Since the cost of heliostats was the highest single component in such plants, efforts were directed on reducing the cost of the heliostat field. Therefore, a low-cost heliostat design based on a glass-reinforced concrete structure was proposed and development began.

After a year of evaluation and testing of the photocatalytic hydrogen process, the quantum efficiency of the process had been improved to almost 30%, but the techno-economic analysis indicated that although the cost might be acceptable, the efficiency for the overall process would not meet DOE requirements. Therefore, it was proposed that the photocatalytic process be replaced by an electrolytic oxidation of the ammonium sulfite solution. This would allow the process to be carried out under more controlled conditions without the need for large areas of photoreactors.

As evaluation of the sulfur-ammonia process continued in 2009, another change to the process chemistry was proposed. A potassium sulfate/potassium pyrosulfate molten salt sub-cycle was proposed to replace the $ZnO/ZnSO_4$ sub-cycle. Substitution of molten salts eliminated the more difficult processes needed to move and handle solid particles, in favor of pumping liquids and containing them in simple tanks. **Table 3** summarizes the reactions of the finalized SA cycle.

Another change considered was to perform the sulfur trioxide decomposition step with electrical heating, rather than directly with solar thermal energy. One impetus for this change was that the thermal energy needed for the sulfur trioxide decomposition was only about 10% of the total. Eliminating the requirement for solar heating of the sulfur trioxide meant that the solar heliostat field could be designed to deliver energy at a much lower temperature, enhancing its efficiency. Also, since electrical production was

included in the system as part of the energy recovery process, there was the potential for self-production of enough excess electricity to power the sulfur trioxide process.

Table 3. Sulfur-Ammonia Cycle with Electrolytic Hydrogen Production and Potassium Sulfate Sub-Cycle

Reaction	Description	Temperature Range
$SO_{2(g)} + 2NH_{3(g)} + H_2O_{(l)} \rightarrow (NH_4)_2SO_{3(aq)}$	Chemical Absorption	25-50°C
$(NH_4)_2SO_{3(aq)} + H_2O_{(l)} \rightarrow (NH_4)_2SO_{4(aq)} + H_2$	Electrolysis	80-150°C
$(NH4)_2SO_4(aq) + K_2SO_4(l) \rightarrow 2NH_3(g) + K_2S_2O_7(l) + H_2O(g)$	Adiabatic Mixing	400-450°C
$K_2S_2O_7(l) \rightarrow SO_3(g) + K_2SO_4(l)$	Thermal Decomposition	790 °C
$SO3_{(g)} \rightarrow SO_{2(g)} + ½O_{2(g)}$	Thermal Decomposition	850-1,200°C

Finally, changes to the operation and design of the system were proposed including continuous operation which meant inclusion of thermal storage into the solar field. Also, a modular approach to the solar field and chemical plants was proposed. The DOE guidelines called for production of 100,000 kg/day of hydrogen, but a single plant to produce at that rate would be enormous. Therefore, the plant design and solar field were scaled to a more reasonable 50 MW peak thermal capacity.

The following sub-sections describe the activities and results of each of the areas of research that were pursued over the course of the project.

3.1 Photocatalytic Hydrogen Production

The initial version of the SA cycle, presented in **Table 2**, incorporated a photocatalytic process for the release of hydrogen by oxidizing aqueous ammonium sulfite to ammonium sulfate. One potential physical implementation of the process is shown in schematic form in **Figure 2**.

The figure depicts the manner in which thermal, *i.e.* near infrared (NIR) and infrared (IR), and the UV-visible portions of solar radiation may be separated using a spectral splitting "hot" mirror (i.e., a dichroic mirror that reflects IR and passes UV and visible light). The thermal part of the sunlight is concentrated at a high temperature thermocatalytic reactor/receiver that operates the oxygen production step, while the photonic (UV and visible light) portion passes through the coating and drives the photocatalytic hydrogen generation reaction.

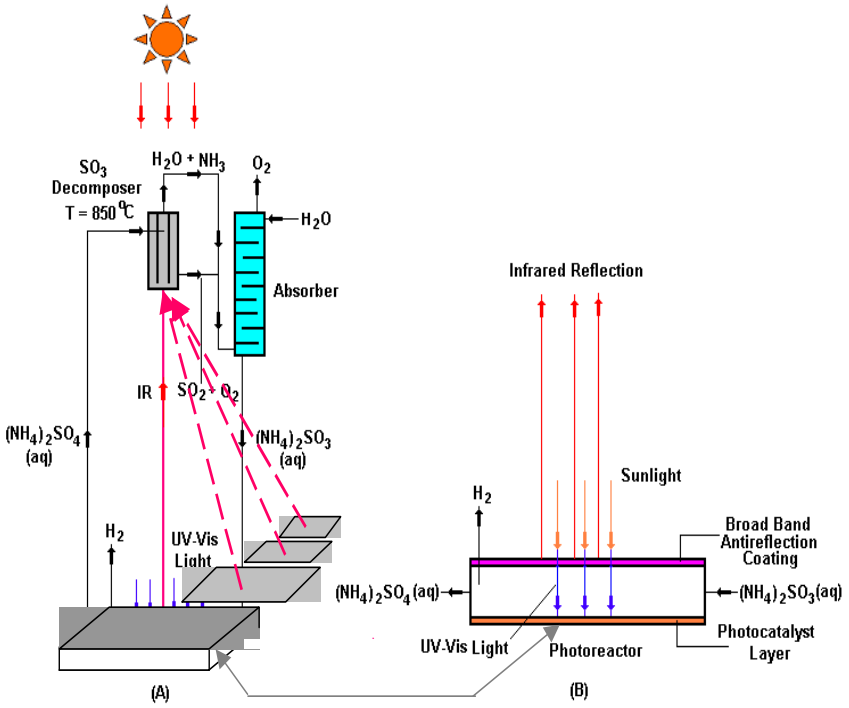

Figure 2. Schematic Diagram of SA Photo-Thermochemical Water Splitting Cycle

Initial experimental data indicated that it was possible to perform the photocatalytic reaction with an energy conversion efficiency[1] of about 12% using CdS as the photocatalyst. As an example, **Figure 3** depicts the rate of hydrogen production from an aqueous $(NH_4)_2SO_3$ solution in a 1 kW solar simulator fitted with an AM 1.5 global filter. The data of **Figure 3** show that the hydrogen production rate can be increased substantially by using polymer-stabilized, Pt-doped cadmium sulfide (CdS) photocatalyst.

[1] Defined as the energy contained in the hydrogen produced (LHV) per unit time divided by the light flux from AM1.5 solar simulator at wavelengths in the range of 300-520 nm illuminating the photolyte.

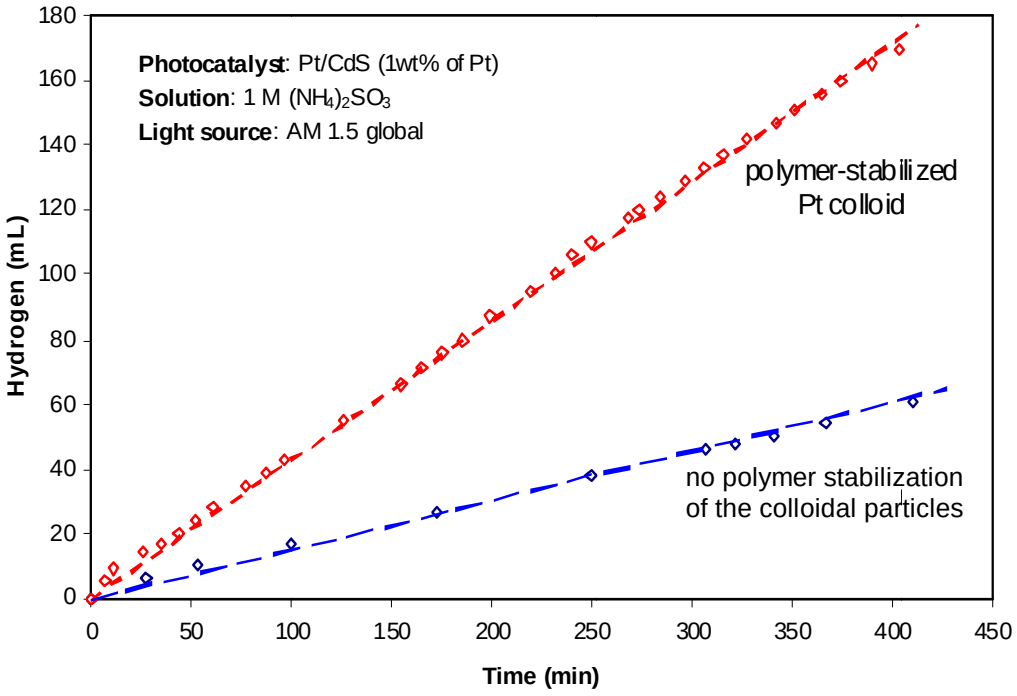

Figure 3. H_2 production from $(NH_4)_2SO_3$ aqueous solution (beam area: 33 cm^2, light intensity: ~1.5 kW/m^2, solution pH = 7.5, solution volume = 200 mL, catalyst: 0.25 g Pt doped CdS)

Further screening was conducted with single and multiple-component catalysts to increase the efficiency of the hydrogen production photo-process. A test apparatus was created with a solar simulator to provide the photons and a temperature-controlled reactor, as shown in **Figure 4**.

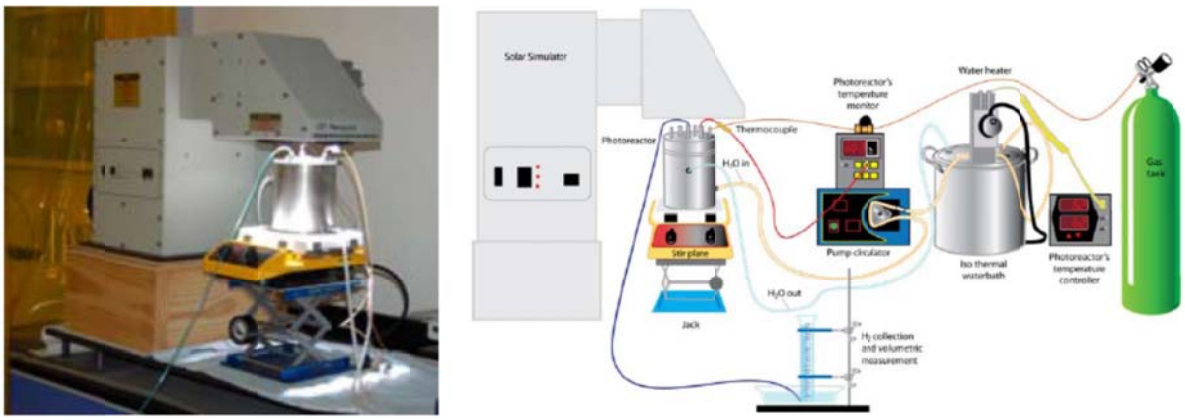

Figure 4. Setup for Photocatalytic Hydrogen Production Experiments

Figure 5 depicts the stability of the photocatalytic system for hydrogen production from an aqueous $(NH_4)_2SO_3$ solution in a 1 kW solar simulator fitted with an AM 1.5 global

filter. **Figure 6** shows the photon efficiency as a function of Pt doping of photocatalyst – indicating that the optimum CdS loading is about 0.4 wt%.

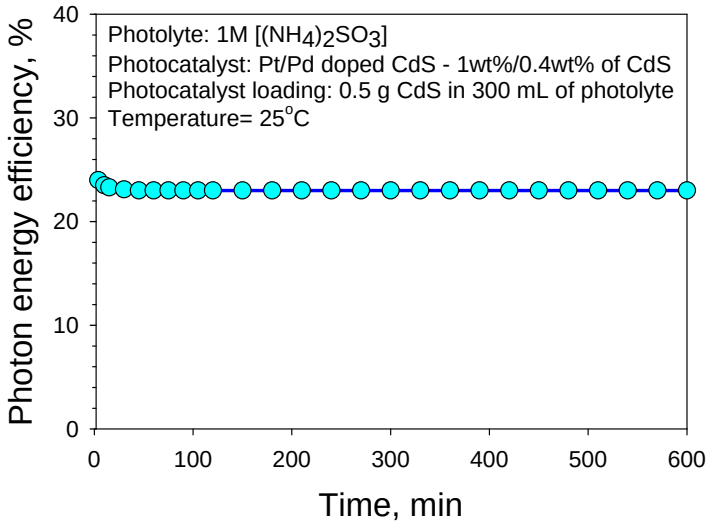

Figure 5. Stability of the Photosystem for Hydrogen Generation

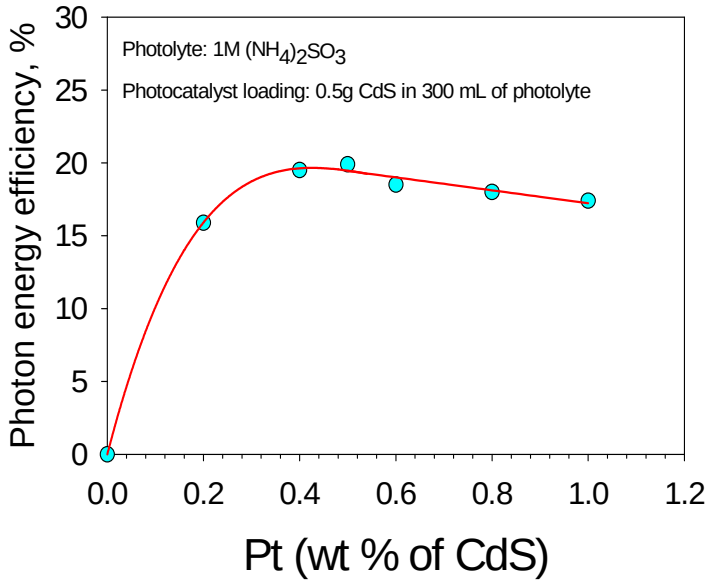

Figure 6. Photon Efficiency as a Function of Single Metal Dopant Loading

After the effects of single-metal doping were determined, testing proceeded to evaluate the effects of multiple metal dopants. The effect of photocatalyst doping with combinations of Pt, Pd, and Ru metals is presented in a ternary diagram in **Figure 7**. The most efficient photocatalyst found during this process consisted of electronic-grade cadmium sulfide doped with small amounts of Pt, Pd, and Ru. This photocatalyst

generated hydrogen with a conversion efficiency of 29.4% as shown by the labeled spot in the middle of **Figure 7**.

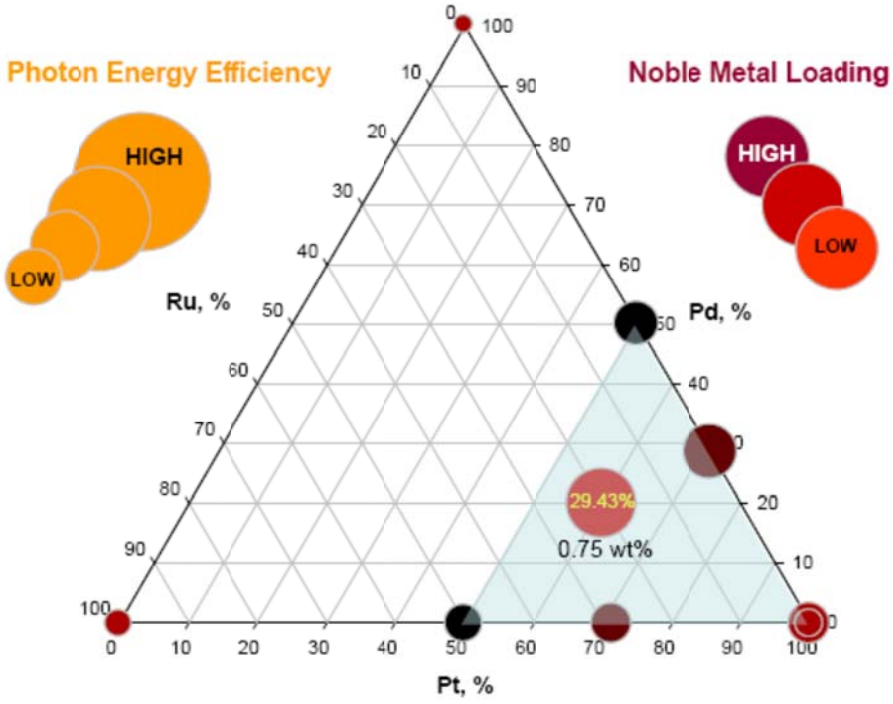

Figure 7. Effect of Photocatalyst Doping (photolyte: 1M [$(NH_4)_2SO_3$], CdS loading: 0.5g in 300 mL photolyte

Other tests were also conducted to characterize the performance of the photocatalytic system. For example, **Figure 8** depicts the effect of photolyte temperature on the photon energy efficiency of bimetallic doped CdS, showing that operation of the photoreactor at lower temperatures is preferred.

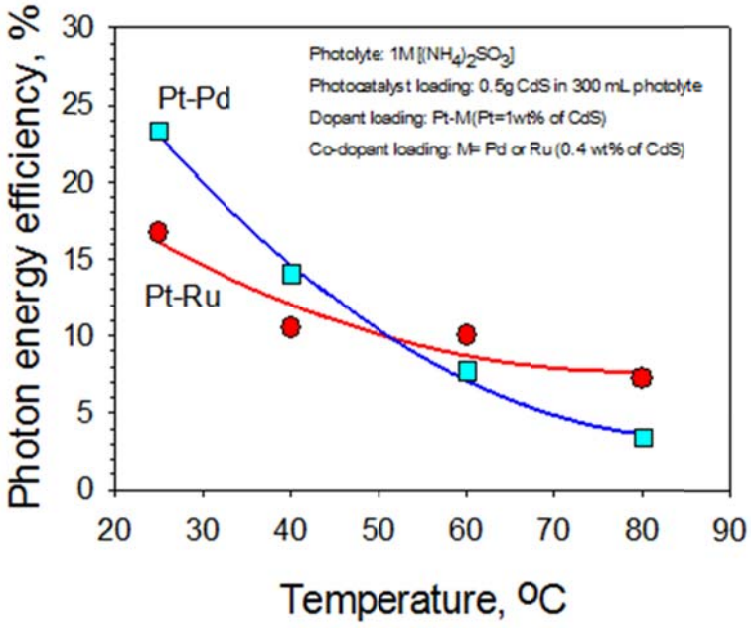

Figure 8. Effect of Photolyte Temperature on Photocatalysis

3.2 Electrolytic Hydrogen Production

The electrochemical oxidation of sulfite was investigated as an alternate process step to the photocatalytic oxidation process. The electrochemical reactions in this case are shown below. Note that the potentials at which each of these reactions occurs are pH-dependent. In basic environments the overall cell voltage should be about -0.1V indicating that if there was no voltage losses, the reactions should occur spontaneously.

Anode reaction:	$SO_3^{2-} + 2OH^- \rightarrow SO_4^{2-} + H_2O + 2e^-$	$E^o = -0.936$ V
Cathode reaction:	$2H_2O + 2e^- \rightarrow H_2 + 2OH^-$	$E^o = -0.828$ V
Overall:	$SO_3^{2-} + H_2O \rightarrow SO_4^{2-} + H_2$	$E^o_{cell} = -0.108$ V

Figure 9 shows current potential curves for the oxidation of sulfite and/or bisulfite at three different pH values at a graphite electrode. At a current density of 50 mA/cm^2 it can be seen that the potential required for sulfite oxidation is highest when the pH is lowest (in this case at a bisulfite pH of 4.9). Similarly the potential required for oxidation drops when the pH is increased to 8.9 and again when it is taken to 12.5.

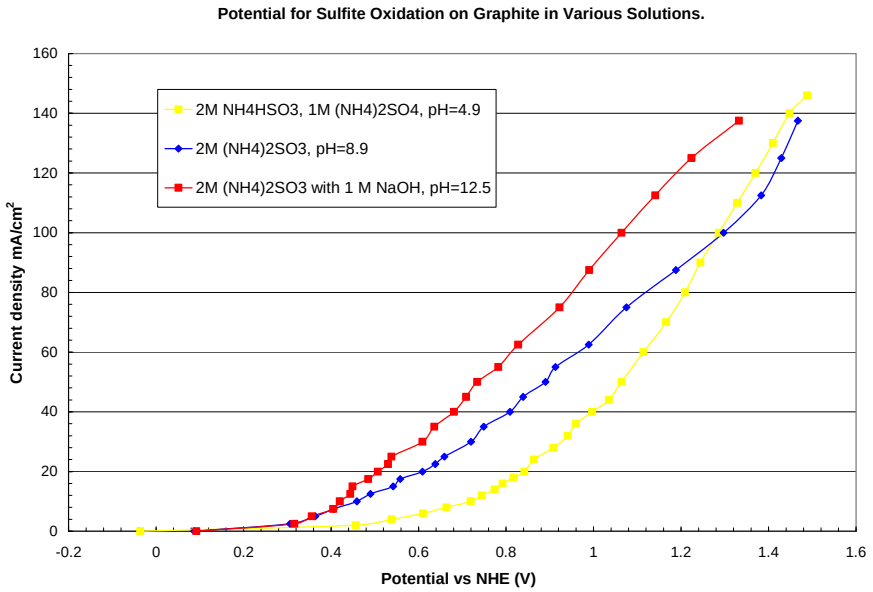

Figure 9. Current/Potential Curves for the Oxidation of Ammonium Sulfite at a Graphite Anode at Three Different pH Values

It should also be noted that the overall magnitude of the potential required for the oxidation is much higher than would be predicted from the thermodynamic values shown above. For the alkaline case, the potential is almost one Volt higher than the thermodynamic value. Some of this may be attributed to resistive (iR) losses in the solution since the experiments were run at high sulfite concentrations; however, these losses should be minimal as a three-electrode configuration was used, with a Luggin probe for the reference electrode[2].

The high potentials required for the sulfite oxidation can be largely attributed to the slow kinetics at the electrode surface; this is often referred to as an overpotential, indicating the potential that is required to drive the reaction over and above the thermodynamic potential. There are three approaches that can be considered to try and reduce this overpotential: (i) reduce the actual current density at the electrode surface; (ii) use electrocatalysts that will promote the oxidation reaction and; (iii) increase the temperature for the reaction. Over the course of this study we have investigated all three of these approaches.

In our initial testing we configured a small flow cell (MicroCell from ElectroCell, Denmark) and incorporated a high surface area carbon felt anode. This approach allows for very low current densities at the carbon fiber level while maintaining an attractive current density on a geometric area basis. The cell was configured in a "flow through" mode such that the solution was flowing perpendicular to the current. The cathode

[2] A SCE reference was used for these measurements and subsequently converted to a NHE scale for reporting purposes.

comprised of a Pt/C membrane electrode assemble (MEA) on a Nafion® 112 (DuPont™) membrane. Current connection was made to the cathode via another carbon felt. A schematic of the cell configuration is shown in **Figure 10**.

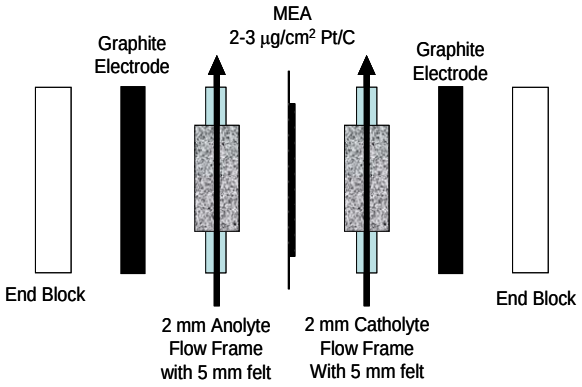

Figure 10. Schematic Showing Assembly of the MicroCell Used for Sulfite Oxidation

Figure 11 shows data from a batch electrolysis of ammonium sulfate (2 mol dm^{-3}) using a graphite felt anode. It can be seen from the pH of the anolyte that as the run progresses, the pH drops; this is caused by the fact that hydroxide is consumed in the reaction and ammonium ion is transported across the cation exchange membrane.

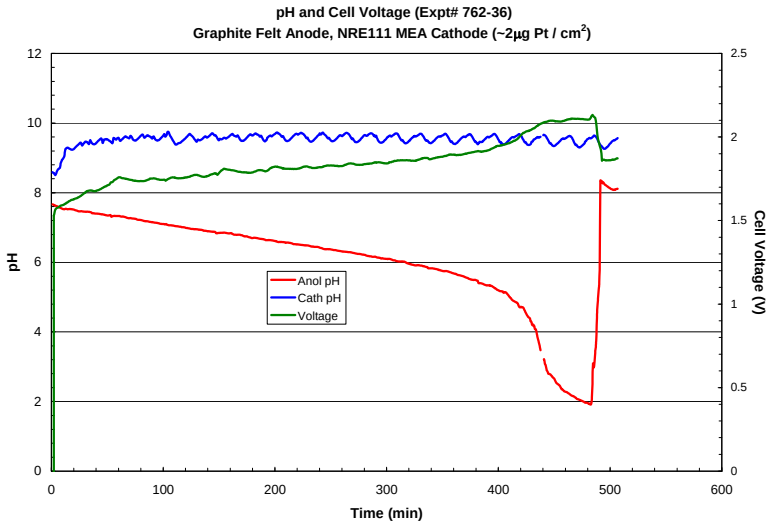

Figure 11. Plot of pH as a Function of Electrolysis Time for a Batch Electrolysis of Ammonium Sulfite; Catholyte was Ammonium Hydroxide; Current Density was 300 mA/cm²

In this experiment the transport number for ammonium transfer was measured at 0.6 (indicating that 40% of the charge is being carried by hydroxide back-migrating across the membrane). Typical of a titration curve, the transformation to all bisulfite/bisulfate can be seen at 420 minutes. At the same time that this occurs there is an increase in cell voltage as the predominant oxidation reaction becomes bisulfite oxidation. Even earlier in the batch a clear increase in cell voltage can be seen as the anolyte pH drops. These observations lead to the conclusion that a final process must be configured such that the anolyte pH is maintained; indeed, we have been able to accomplish this by simply scrubbing the ammonia that is liberated from the ammonium hydroxide catholyte back into the anolyte. This ammonia scrubbing process would be included in the operating plant and is included in the detailed Aspen Plus® model.

Using this cell configuration we were able to run at a total cell average voltage of 1.75V at a current density of 300 mA/cm^2 and a temperature of 80^{o}C. The hydrogen production was measured as 100% efficient in terms of hydrogen produced per unit of charge passed through the device. The data from this run indicate again that there is a very large overpotential at the anode for the oxidation of sulfite. The total cell voltage of 1.75V can be attributed to the potentials required for each electrode reaction (thermodynamic plus overpotential) and the resistance of the anolyte/catholyte and membrane. The latter has been measured externally to the cell using a DC technique in which the voltage drop across the membrane as a function of current passed is used to calculate the areal resistance of the membrane. Based on these measurements together with some assumptions about the cathodic overpotential, it is estimated that over half of the total cell voltage is due to the overpotential at the anode with a large contribution from solution resistance.

Figure 12 shows the approximate voltage contributions for the electrolysis cell shown above operating with a graphite felt anode at 100 mA/cm^2. At this current density the total cell voltage was 1.4V.

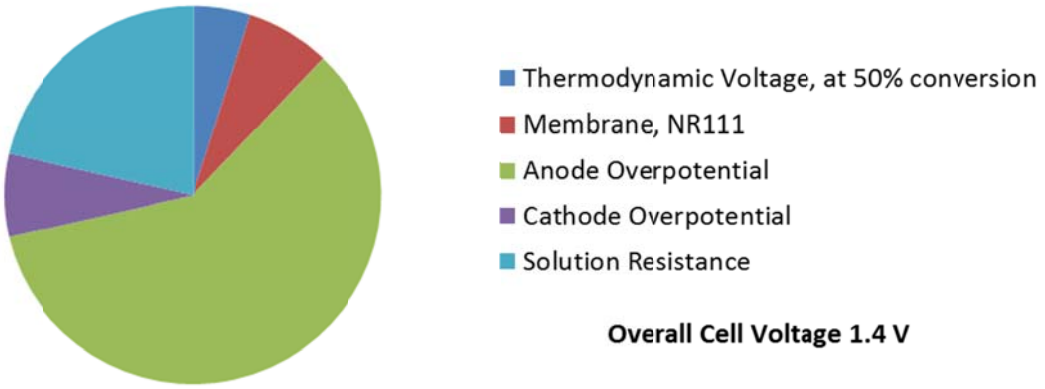

Figure 12. Approximate Breakdown of Cell Voltage for Microcell Operating at 100 mA/cm^2 and 80°C

Referring to the figure, the anode overpotential is clearly the largest contributor to the overall cell voltage, followed by the solution resistance. The latter has been calculated based on the measured solution conductivity; however, the reality is that the resistive losses in the anolyte are not as simple as that as they will be offset by the electrical conductivity of the felt. We have shown that by changing the test cell from the MicroCell to a fuel cell type of cell, the cell gap was decreased by about 50%, reducing the solution iR component and therefore the total cell voltage. This uncertainty does not change the conclusion that the anode overpotential is the major contributor to cell voltage and, if anything, it is understated.

3.2.1 Electrocatalyst Development

Several techniques have been evaluated for screening sutable catalysts for the electrooxidation of sulfite. These have included the following:

1. Electrodeposition of catalysts onto carbon subtrates (including carbon felts), including pulsed electroplating techniques [7]
2. Thermal decomposition of metal nitrates onto carbon felt materials [8]
3. Electrophoretic deposition of nano catalysts onto carbon subtrates [9]

Once the catalysts were prepared they were screened by either running current potential curves on a three-electrode configuration against a standard reference electrode, or they were run in a microcell or fuel cell paired with a Pt/C MEA so that relative performance could be assessed. This latter technique was employed to remove some of the problems associated with testing carbon felt type electrodes (i.e., making electrical connections and avoiding uncompensated iR drops in the measurements).

Many catalysts have been screened including oxides and sulfides of cobalt, tungsten, molybdenum, manganese, tin, nickel, vanadium and antimony. Various spinels (XY_2O_4) chosen from suitable oxidation states of some of these materials, metal phthalocyanine catalysts as well as known oxygen reduction catalysts (gold, platinum/cobalt and rhodium) were also investigated. **Table 4** shows some of the more promising catalysts tested together with their deposition techniques. For ease of comparison we have presented only the total cell voltage from experiments in a cell with a Pt MEA as the cathode. These measurements were made in a 25 cm^2 fuel cell that had reduced cell gap and typical serpentine flow fields. In general the Pt/Co and Rh catalysts have worked best and depositing these materials as nano-particles gives even better results. As can be seen from the table we have been successful in reducing the cell voltage significantly; however, we are still operating at voltages well above the thermodynamically predicted voltage indicating that more improvements can be expected from further catalyst development.

The effects of electrocatalysis and temperature are further illustrated in **Figure 13**. These are short-term data from a Micro flow cell incorporating graphite-felt anodes. If the data at 100 mA/cm^2 are compared, the effect of increasing the temperature from 80^oC to 130^oC is to reduce the cell voltage from 1.36 to 0.86V. Maintaining a temperature of 80^oC but incorporating a Pt/Co catalyst onto the anode felt results in a similar reduction.

Table 4. Cell Voltages Obtained for Cell Operated with 2 M Ammonium Sulfite at 80°C and 100 mA/cm^2, all Incorporating N212 MEA (with Pt Cathode Catalyst)

Catalyzed Anode Layer and Ink Composition	Cell Voltage (V) at 100 mA/cm^2
Electrophoretic Deposited Pt_3Co on felt (nano particles of catalyst on carbon support; average diameter 5 nm)	0.88
Electroplated Rhodium on felt (pulse electrodeposition from sodium hexachlororhodate solution)	0.88
Doubled Sided MEA with Rh/C Anode Catalyst Layer	0.91
1404 μg/cm^2 WO_3 ink on GCO8 cloth	0.92
Electrodeposited Pt/Co on Felt (pulsed electrodeposition from potassium tetrachloroplatinate and cobalt (II) chloride solution)	0.93
1031 μg/cm^2 $NiFe_2O_4$ ink on GC08 cloth	0.93
1334 μg/cm^2 $CoFe_2O_4$ ink on GC08 cloth	0.93
Electrophoretic Deposited Rhodium (nano particles of catalyst on carbon support, diameter unknown)	0.93
408 μg/cm^2 Pt_3Co ink on GC08 cloth	0.96
1336 μg/cm^2 Co_3O_4 ink on GC08 cloth	0.96
1294 μg/cm^2 SnO_2 ink on GC08 cloth	0.96
Electrophoretic Deposited CoPhth EPD (883-49-1)	0.96
GC08 Cloth (plain)	1.09

3.2.1.1 Electrophoretic Electrocatalyst Deposition

Since the kinetics of the sulfite oxidation reaction are very slow, we attempted to increase the available surface area of the catalyst by using nanoparticles. Electrophoretic deposition of said particles is a convenient method for putting them onto a conductive substrate. The approach for the development of potential nano-sized electrocatalysts has been to:

- Synthesize nanoparticles and characterize nanoparticle deposits by scanning electron microscopy (SEM) for electrocatalytic activity testing
- Vary electrophoretic deposition conditions in different bath chemistries for various graphite substrates in order to improve electrocatalytic activity of the deposits

- Compare anodic electrocatalytic activity of different nanoparticle deposits to determine the best electrocatalysts for the SA cycle

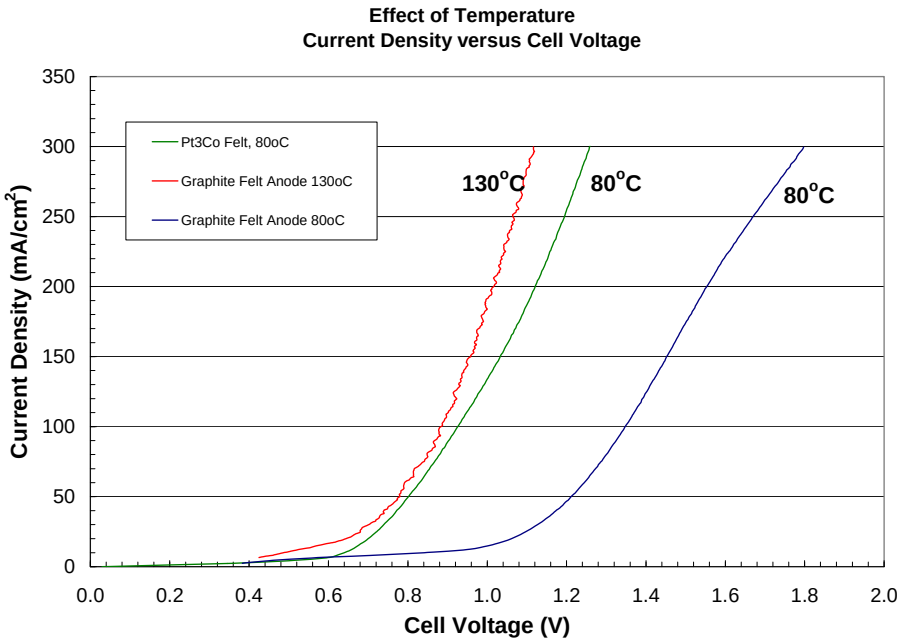

Figure 13. Plot of Current Density vs. Cell Voltage for a Micro Flow Cell with and Without Anode Catalyst at Two Temperatures

Cobalt ferrite and platinum cobalt nanoparticles were deposited via electrophoretic deposition (EPD) with two new suspension chemistries that produced thinner and more distributed layers of the catalysts [6]. Cobalt ferrite nanoparticles were synthesized using a co-precipitation method [10]. Samples were analyzed using a scanning electron microscope (SEM), which showed particles from 4-20 nm, and an energy-dispersive x-ray spectroscopy (EDX) to verify composition. Pt_3Co was synthesized using a solvothermal process [10] in which nanoparticles formed in a sealed autoclave; the particle size of 20 ± 5 nm was measured using a SEM image. Nanoparticles of 30 wt% platinum cobalt on carbon were also purchased from Sigma Aldrich (the latter are the same materials shown in **Table 4**). SEM images showed that the Pt_3Co-loaded carbon particle size was 50 ± 15 nm.

Synthesized nanoparticles of cobalt ferrite (20 nm) and purchased platinum cobalt on graphite (50 nm) were mixed into either 100% ethanol or 90% water/10% isopropanol with hexadecyltrimethylammonium bromide (CTAB). Then the nanoparticles were deposited onto either graphite paper or graphite felt using EPD. Linear sweep voltammetry (LSV) in 2 M ammonium sulfite was performed to test the electrocatalytic activity of the deposits compared to blank graphite substrates**.**

The first EPD bath contained 2 g/L particles suspended in 90 vol% water and 10 vol% isopropanol with 0.4 g/L CTAB. **Figure 14** compares the zeta potential of cobalt ferrite

in 90% water/10% isopropanol solution with and without CTAB as a function of pH as changed with the addition of nitric acid and sodium hydroxide. The zeta potential was only positive at low pH without CTAB, but remained positive with addition of CTAB over a wide range of pH values. The second bath contained 2 g/L particles suspended in 100 % ethanol. The zeta potential of the cobalt ferrite nanoparticles in the CTAB bath chemistry at a pH of 6.2 was 20 ± 2 mV.

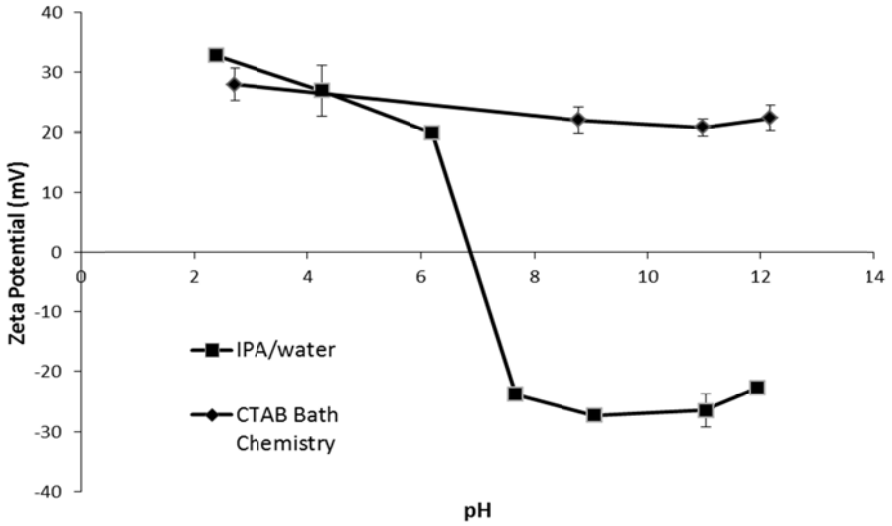

Figure 14. Zeta Potential vs pH for Cobalt Ferrite Particles in a 90 vol% Water, 10 vol% IPA Solution and in a CTAB Solution

Electrophoretic deposition (EPD) of both cobalt ferrite and platinum cobalt nanoparticles was achieved from two different bath chemistries. Cobalt ferrite deposits from a 100% ethanol bath at a pH of 5 gave a 3-5 layer deposit that was evenly distributed across the substrate. The platinum cobalt particles on carbon were large and deposited in small agglomerates from both tested baths. Sonication of the bath during EPD resulted in smaller agglomerates that were more evenly distributed in comparison with deposits conducted without sonication.

The deposits were tested for electrocatalytic properties for the oxidation of ammonium sulfite to ammonium sulfate. Linear sweep voltammetry was used to compare the electrocatalytic activity of cobalt ferrite and platinum cobalt nanoparticles deposited on graphite paper using EPD. Cobalt ferrite was deposited at 35V for 60 s from a 100% ethanol bath. Platinum cobalt was deposited with an applied voltage of 13V for 15 s from a CTAB bath. The deposit densities varied from 0.3 mg/cm^2 to 0.8 mg/cm^2 depending upon the EPD bath chemistry and material deposited. As shown in **Figure 15**, both cobalt ferrite and platinum cobalt nanoparticle deposits show enhanced electrochemical activity compared to graphite paper; that is, a higher current density for all voltages scanned. Further EPD was conducted and deposits tested by LSV (current density vs applied voltage).

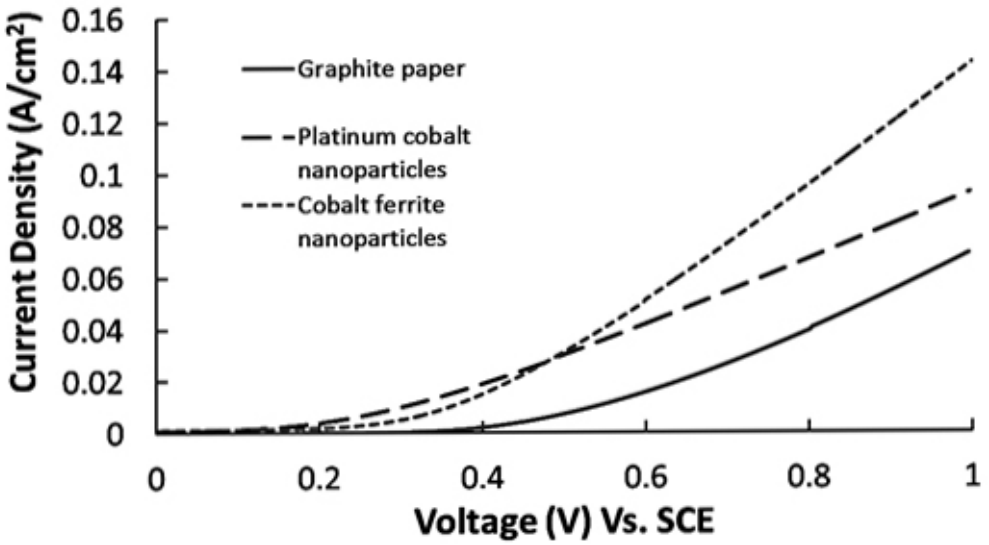

Figure 15. Electrocatalytic Activity of EPD Deposits Showing Current Density vs. Voltage

Figure 16 compares the LSV of cobalt ferrite (CF) and platinum cobalt (PC) nanoparticles deposited on graphite paper using EPD from ethanol (E) and CTAB baths at a concentration of 1 mM (CHigh) or 0.05 mM (CLow). The EPD conditions were an applied voltage of 30V for either 1 or 2 min. The measured current ranged from 6 mA to 69 mA with deposit weights ranging from 0.42 mg to 0.92 mg. All deposits showed electrochemical activity greater than the blank graphite paper. The platinum cobalt deposit from an ethanol bath showed the highest electrochemical activity, greater than the three deposits of cobalt ferrite.

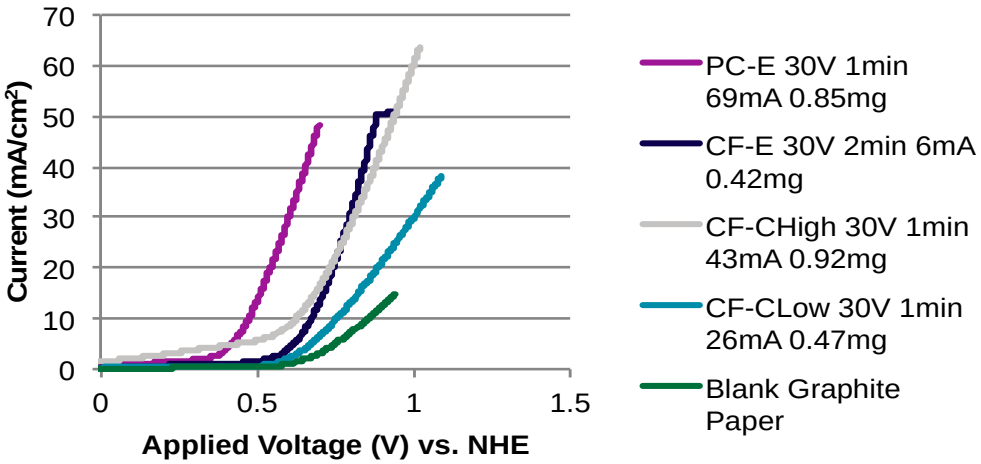

Figure 16. Electrocatalytic Activity of EPD Deposits on Graphite Paper Showing Current Density vs. Voltage

Figure 17 compares the LSV (current density vs. applied voltage) of cobalt ferrite (CF) nanoparticles deposited on graphite felt using EPD from ethanol (E) and CTAB bath at a concentration of 1 mM (CHigh) or 0.05 mM (CLow). The EPD conditions were an applied voltage of 21- 40V for 1 - 2 min. The measured current ranged from 29 mA to 219 mA with deposit weights ranging from 6 mg to 14.6 mg. A much larger number of nanoparticles could be deposited on the 3-dimensional felt. All deposits showed electrochemical activity greater than the blank graphite felt. The cobalt ferrite deposit from low concentration CTAB bath showed the highest electrochemical activity.

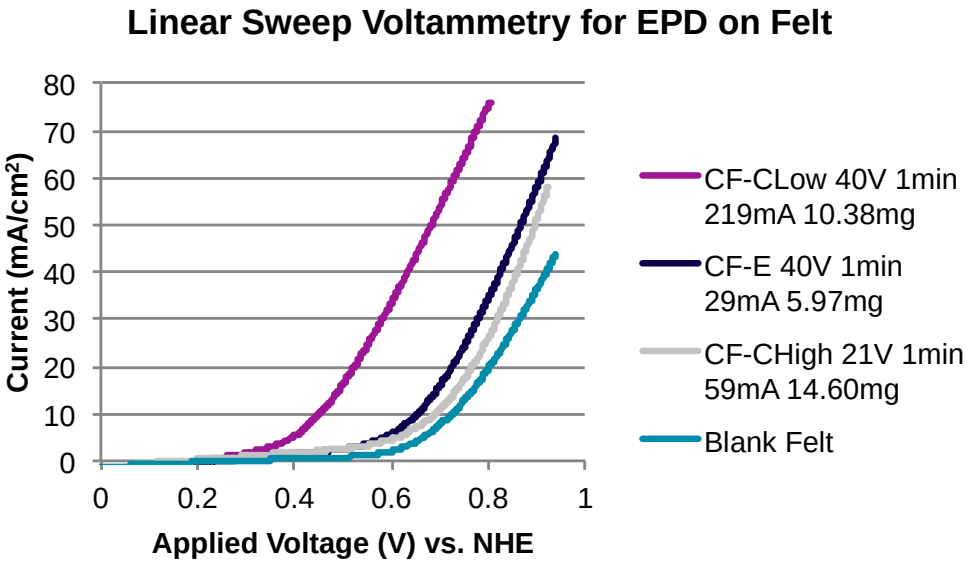

Figure 17. Electrocatalytic Activity of EPD Deposits on Graphite Felt showing Current Density vs. Voltage

The deposits were also examined by scanning electron microscopy (SEM). **Figure 18** compares the SEM images of the cobalt ferrite samples which were the most electrochemically active with blank substrates. From these micrographs and others, it was concluded that deposits with minimal exposed substrate, as a result of thick depositions with slight cracking, tended to have better electrocatalytic activity compared to sparse, thin deposits.

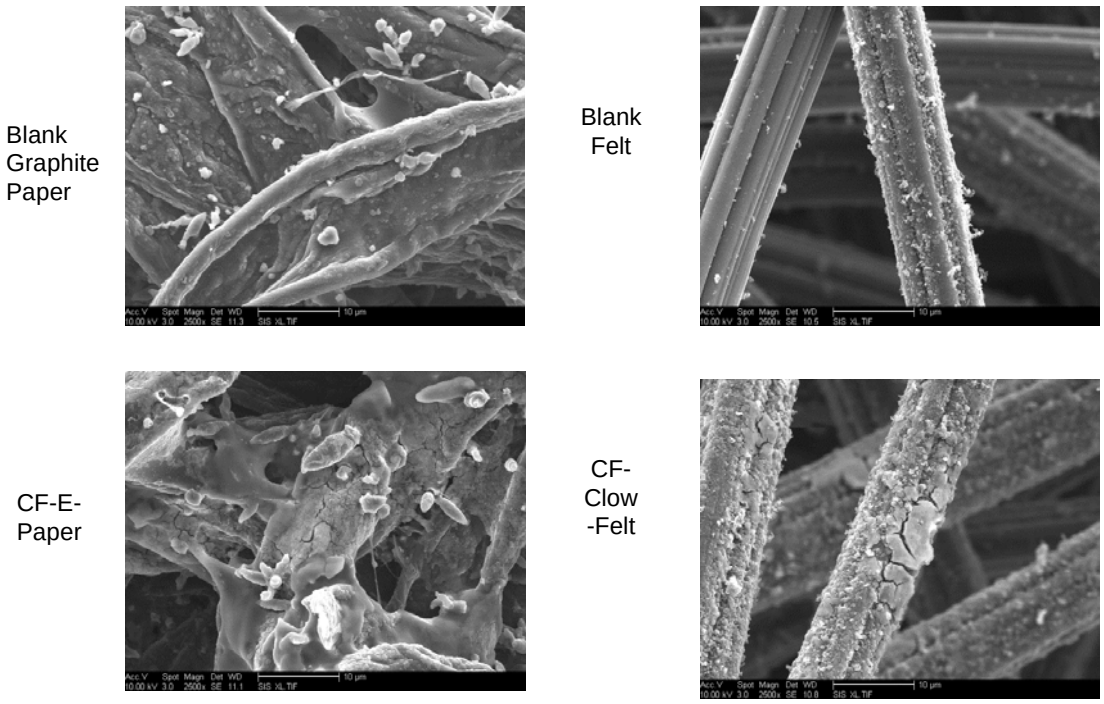

Figure 18. SEM Micrographs of Cobalt Ferrite Nanoparticles Deposited on a Graphite Paper and Felt Substrates Compared to the Blank Substrates

3.2.2 Membrane Testing

The ideal electrochemical process for the oxidation of sulfite and cathodic generation of hydrogen would have no separator, as this would afford the lowest cell voltage. Early in our investigations, there were indications that this might indeed be possible in an alkaline environment where hydrogen evolution was found to be a preferable reaction to the reduction of sulfite. This is quite different from the acidic environments (such as the hybrid sulfur process) where SO_2 can easily be reduced to sulfur. At high pH values, we found that undivided cell operation was possible, but only at low temperatures. As the temperature of the cell was increased to >60^{o}C significant sulfite reduction products were seen and the corresponding Coulombic efficiency for hydrogen was diminished. Clearly, if a high temperature is to be employed then a separator is indeed necessary.

We tested both anion and cation selective membranes as both separators and electrolytes (i.e. when used as a support for the MEA). The requirements for a membrane in this system are to have a low resistance and be stable at high temperature. The temperature requirement is to accommodate the need to run the entire cell at the highest practical temperatures thereby increasing the kinetics of the anodic reaction. This puts an additional constraint on the membrane in that it must also exhibit low sulfite transfer from the anolyte to the catholyte even at high temperature.

It was observed that membranes that had been exposed to elevated temperature (>100^{o}C) showed orders of magnitude increases in the flux of sulfite. This continues to be the case even if the membrane is returned to room temperature, indicating that the temperature

excursion "permanently" changes the membrane. Indeed, testing of an electrochemical cell with a Nafion 212 membrane at 128°C showed such a high rate of flux of sulfite across the membrane that the Coulombic hydrogen production efficiency was significantly reduced. (Sulfite transferred to the catholyte compartment can form dithionite, thiosulfate, sulfur and sulfides). As a screening tool, we have exposed membranes to elevated temperature and pressure for several days and then measured sulfite flux at room temperature. The flux measurements are made without any current passing in a cell so that the sulfur species in the receiving side could be analyzed.

Table 5 shows the performance of Nafion 212 (DuPont) and a cross linked membrane from Fumatech FX7050. It can be seen that the flux of sulfite across the NR212 membrane increased by approximately a factor of 50 after conditioning at 120°C for three days. Testing in an electrochemical flow cell confirmed these data and showed the membrane to be unsuitable for this application due to diminished hydrogen production efficiency.

Table 5. Sulfite Flux Measurements for DuPont Nafion and FuMaTech Membranes at Room Temperature After Pre-conditioning as Shown

Membrane and Pre-conditioning	Sulfite Flux $\mu mol/m^2/sec$
Initial Membrane of Interest	
NR212 untreated	21
NR212, Boiled 2hr DI water	720
NR212, 120^0C and 85psi for 3 days	970
Membrane Used in 500-Hour Test	
FX7050, boiled DI water 0.5hr	250
FX7050, 120^0C, 85psi (in 1M $(NH_4)_2SO_3$) 3.5days	190
FX7050, 120^0C, 85psi (in 1M $(NH_4)_2SO_3$) 18hr	240
New Developmental Membrane (DuPont™)	
NAF E113901-45 as received	1.3
NAF E113901-45 boiled 2hr DI water	94
NAF E113901-45 120^0C, 80psi for 7.75 days	9.2

The cross-linked membrane from FuMaTech (FX7050) performed much better at the elevated temperature showing almost the same sulfite flux before and after conditioning. This membrane was used in our long-term (500 hour) testing described in section 3.2.3.

Subsequent to completing the initial long-term testing, we received a developmental membrane from DuPont thought to have better stability at high temperatures. This membrane has shown very good performance even after treating at 120^{o}C for 7.75 days showing flux numbers that are significantly lower than the other membranes. This membrane has also been tested in the full electrochemical cell and the results are reported in section 3.2.4.

Table 6 shows the resistance of the two Nafion membranes tested together with a Nafion 115 membrane for comparison. Note that at a current density of 100 mA/cm^2, a resistance of 1.4 Ohm cm^2 would result in a voltage drop of 140 mV. The resistance is significantly less at elevated temperatures.

Table 6. Ex-Situ Resistance Measurements at Room Temperature in 2M Ammonium Sulfite

Membrane	Resistance (Ω.cm^2)
Nafion 115	1.4
Nafion NR112	0.9
NAF E113901-45 (after 7.75 day soak at 120^{o}C)	1.4

3.2.3 Long-Term testing of Electrochemical Cell Components

A 500-hour durability test was successfully completed using an electrochemical cell comprising a Pt/Co catalyzed anode on a carbon felt substrate and a Pt/C MEA cathode on a FuMaTech FX-7050 cation exchange membrane. The test was run at 100 mA/cm^2 for a total of 550 hours of electrolysis time, at a temperature of 100^{o}C. This temperature required the use of a pressure vessel to keep the electrolytes from boiling. The simplest way to accomplish this was to put the electrochemical cell into a pressure vessel. The cell used in this test was a 25 cm^2 cell, which is housed in the chamber to the right shown in **Figure 19**. The anolyte and catholyte tanks are shown on the far left and center respectively. The anolyte was initially 2M ammonium sulfite, and the catholyte a solution of 0.5M ammonium hydroxide and 1M ammonium sulfate. The ammonium sulfate was added to maintain a reasonable osmotic pressure balance across the membrane. The system was pressurized with nitrogen, and hydrogen gas generated in the catholyte was scrubbed through the anolyte solution thereby removing any entrained ammonia and maintaining the pH of the anolyte throughout the batch.

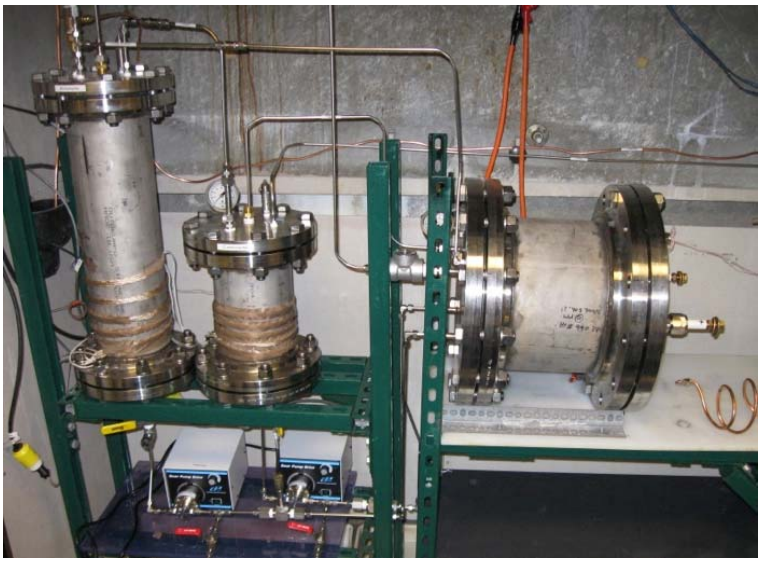

Figure 19. Test Rig for Operation of Electrochemical Cells at High Temperature and Pressure; The Electrochemical Cell is Housed in the Chamber to the Right Which is Maintained at Pressure Facilitating Operation at 130°C

The durability testing was done as four consecutive batch electrolyses with each experiment being run to approximately 90% conversion of sulfite to sulfate. The coulombic efficiency for hydrogen production was 94% and the cell voltage increased reproducibly and consistently over each batch by an amount predicted from thermodynamic calculations based on the conversion (1.09 – 1.17V). **Figure 20** shows excellent reproducibility for the change in concentration of sulfite for the four consecutive batches as a function of charge passed. Note that as the electrolysis proceeds, there is also a concentrating effect in the anolyte as water transfer accompanies the transport of cations across the cation exchange membrane. We measured the water transfer rate to be 3.1 moles/mole of charge passed which is consistent with observations in other electrochemical systems.

The purpose of the durability test was to demonstrate the stability of the electrocatalysts and the membrane. This can be assessed by looking for changes in coulombic efficiency and cell voltage as a function of electrolysis time. The coulombic efficiencies were consistent over the entire run. Given the small changes in cell voltage as a function of conversion, the cell voltage needs to be compared at the same anolyte conversion for each batch. This was done towards the end of each batch and showed that the cell voltage was 1.139V +/- 6 mV, or 0.5% variation between batches, again showing excellent stability over the 550-hour test. The cell voltage vs. charge passed is shown overlaid for all four batches in **Figure 21**.

Previous attempts to run durability tests at elevated temperature (100-130°C) with the Nafion 212 membrane were abandoned due to high sulfite transfer and subsequent reaction at the cathode. Using the FX-7050 membrane, the sulfite flux averaged 170 µmole/m^2/s over the entire test.

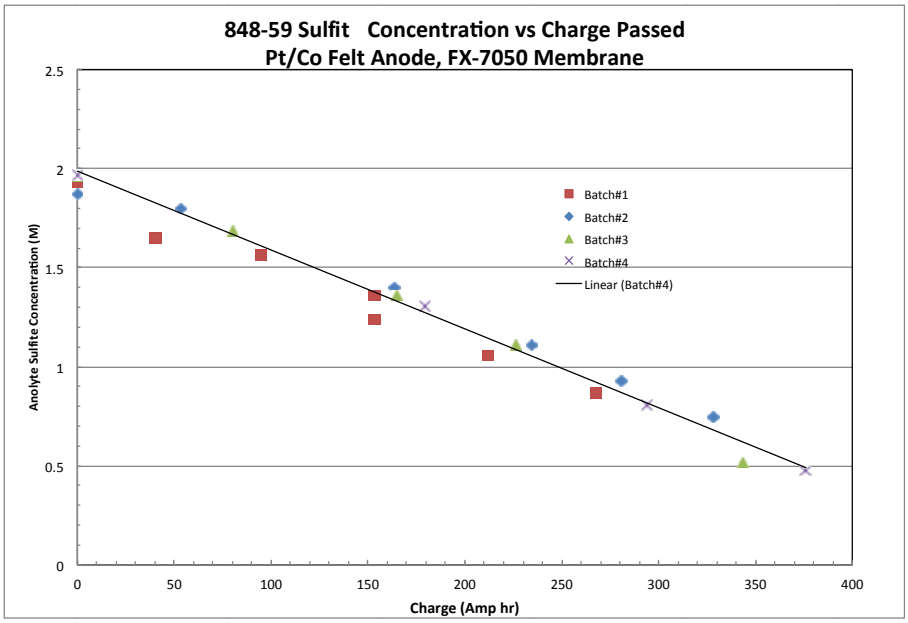

Figure 20. Sulfite Concentration in the Anolyte as a Function of Charge Passed for Four Consecutive Batches Totaling 550 Hours of Electrolysis

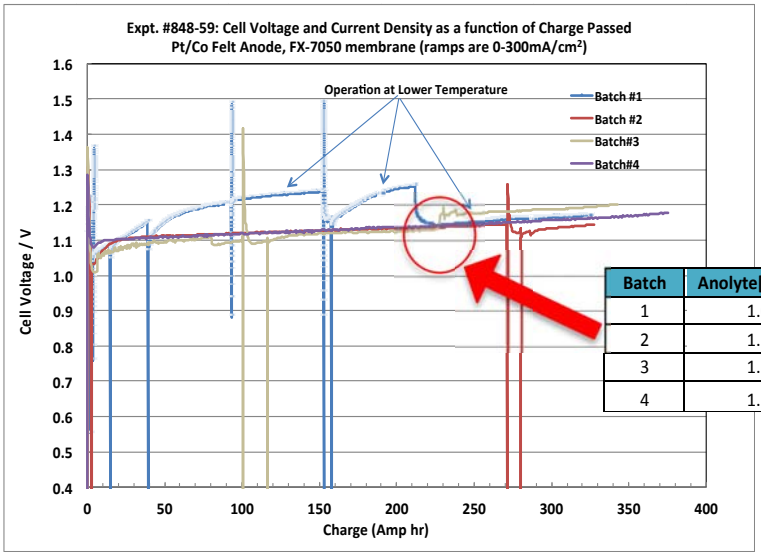

Batch	Anolyte[SO_3] (M)	Measured Anolyte pH	Voltage (V)
1	1.02	9.7	1.146
2	1.16	7.7	1.137
3	1.12	8.4	1.131
4	1.12	8.3	1.141

Figure 21. Cell Voltage vs. Charge Passed for Four Consecutive Batches Totaling 550 hours of Electrolysis

3.2.4 Membrane and Catalyst Modifications

After running the long-term test described above, we made further improvements in the cell operation by incorporating the best oxidation catalysts and running at higher temperatures. Operation at higher temperature has required better membranes. As discussed above, the standard membranes available from DuPont (e.g. Nafion 212) show unacceptable increases in sulfite flux as the temperature increased above 100^{o}C. As shown in **Table 6** above, a developmental membrane provided to us by DuPont was shown to have a lower sulfite flux. When this membrane was incorporated into an electrochemical cell, the initial performance was found to be improved over the Nafion or FuMaTech membranes in terms of sulfite flux, but the cell voltage increased significantly as the temperature was ramped from 100^{o}C to 130^{o}C. This has been attributed to dehydration of the membrane at elevated temperature.

Alternate separators have been investigated in an attempt to allow operation at 130^{o}C . These have included nanoporous separators and cation and anion exchange membranes from various supplies and of different chemistries. Work with polybenzimidazole membranes from FuMaTech showed very low sulfite transport and stability to over 200^{o}C. However, these membranes require either high acid or caustic strength to remain conductive. In our tests, the FuMaTech AM membrane initially performed well after being conditioned in acid, but its resistance slowly increased in the moderate pH sulfite solutions.

We also investigated several techniques to modify the membrane by "filling" it with solids in an effort to maintain conductivity and/or reduce sulfite flux. We tried two filling techniques, one with zirconium phosphate [11] and the other with furfuryl alcohol [12]. We also tried casting a membrane from a Nafion solution that also incorporated molybdenum phosphate [13]. Of the methods tried to date, the zirconium phosphate treatment has been the most successful. **Table 7** shows the sulfite flux comparison for the zirconium phosphate filled membrane compared to the as-received material. While the flux is slightly higher, this increase is less than would be expected considering that the measurement was done at 90^{o}C compared to the other measurements at room temperature.

Table 7. Sulfite Fluxes for DuPont Developmental Membrane

Membrane and Pre conditioning	Sulfite Flux µmol/m^2/sec
New Developmental Membrane (DuPont™)	
NAF E113901-45 as received	1.3
NAF E113901-45 120^{0}C, 80psi for 7.75 days	9.2
NAF E113901-45B zirconium phosphate treatment (883-76) then 130^{0}C for 66 hours	47 (at 90^{o}C)

These membrane modifications have enabled us to operate the developmental membrane from DuPont at 120°C. This has been coupled with the Rh catalyzed anode[3] put onto the membrane as an MEA using an ink of supported Rh on carbon (170 µg Rh/cm^2). The cathode side was the Pt on Carbon (375 µg/cm^2) and the cell was a fuel cell type arrangement. This combination has given the best voltages to date of 0.8V. The sulfite flux in these experiments was 77µmole/m^2/s and the coulombic hydrogen efficiency was measure at >95%. This voltage is an initial voltage from short term experiments and further work is needed to assess long term durability

Figure 22 shows the approximate voltage contributions to the overall voltage for the cell. When compared to the initial work (see **Figure 12**) it can be seen that there has been a significant improvement in several of the contributing cell voltages; however, the anode overpotential is still the largest factor.

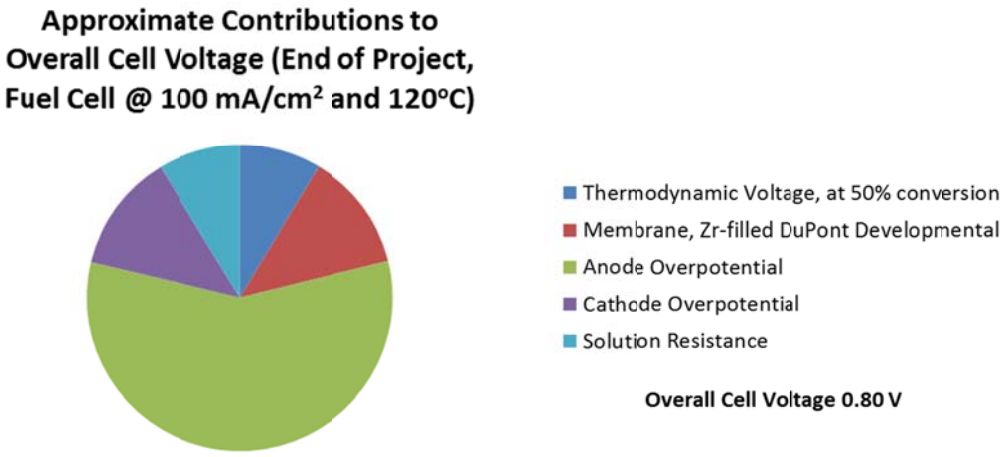

Figure 22. Approximate Breakdown of Cell Voltage for Cell Operating at 100 mA cm^{-2} with Zr-Phosphate Filled Membrane and Rh Catalyzed Anode

Figure 23 summarizes the progress made during this development program in terms of the overall cell voltage. Again, this chart illustrates the large contribution of the anode overpotential to this reaction. Nevertheless, we have been able to achieve a 43%

[3] The double-sided MEA was made by preparing separate platinum and rhodium inks from carbon supported catalyst material (20% Pt on carbon and 5% Rh on carbon). The ink was prepared by taking 1.5 g of catalyst solid, 6 g of 10% Nafion solution and about 20 g of ethanol (added to facilitate the use of an airbrush). The membrane was sprayed evenly with the Rh ink over the required surface area, allowed to air dry (removes the majority of the ethanol) and the weight monitored until the desired weight loading was obtained. The process was repeated for the platinum ink. The MEA was then pressed at about 40 psi and 130°C for 30 seconds between Teflon sheets.

reduction in cell voltage through a combination of electrocatalyst, membrane and cell development improvements.

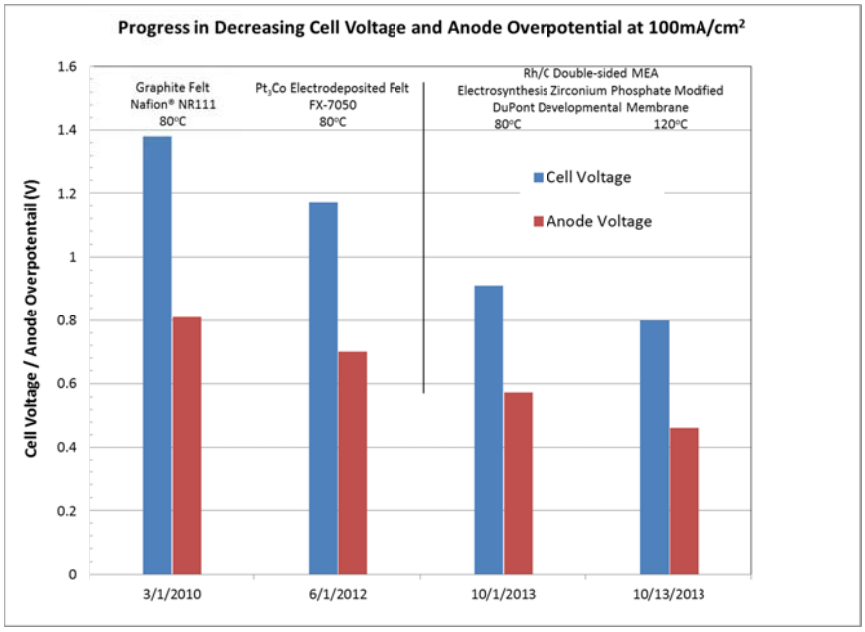

Figure 23. Progress Over Project in Decreasing Cell Voltage and Anode Overpotential

3.3 Oxygen Production with Zinc Sulfate

The oxygen evolution subcycle was investigated using TG/DTA-MS, TPD-MS, IC, GCMS-MS, and UV-vis spectrometric methods. Tests showed that the chemistry of the ammonium sulfate/zinc oxide reaction has fast reaction kinetics and generates ammonia, H_2O and zinc sulfate with no undesirable byproducts, and that the evolution of ammonia and water vapor occurs below about 500°C, while evolution of sulfur dioxide and oxygen is observed only above about 700°C. These results confirmed the facile chemistry and simplicity of the high temperature oxygen production steps of the SA cycle.

Experiments involving the high temperature reactions were conducted at FSEC using a Perkin-Elmer Diamond™ TG/DTA coupled to a Pfeiffer ThermoStar™ quadrupole mass spectrometer (MS). In some experiments, gas samples were taken at the posterior of an Altamira AMI 200 catalyst characterization instrument capable of TPD/TPR/TPO using a gas sampling syringe and were analyzed on a GC-MS system (JEOL GCmate-II GC/MS-MS). Typical results are presented in **Figure 24** to **Figure 26**.

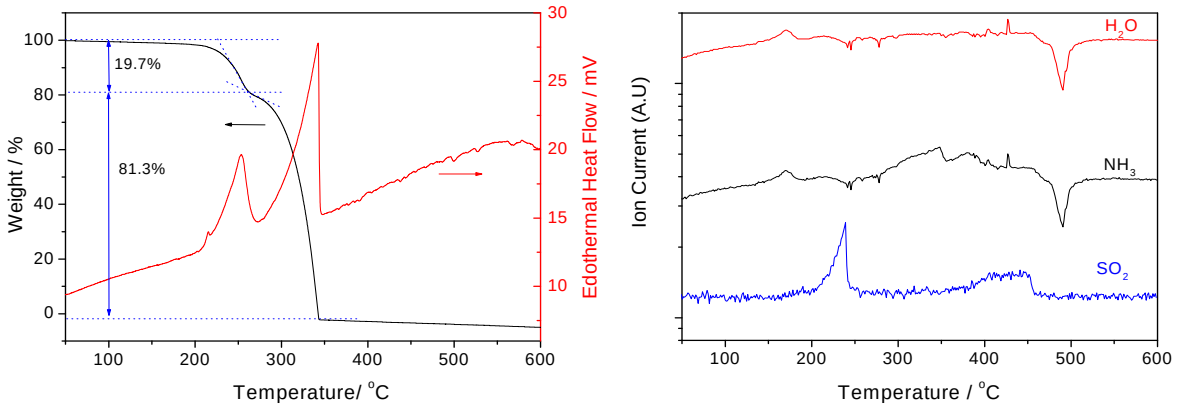

Figure 24. TG/DTA/MS Analyses of Pure $(NH_4)_2SO_4$ Decomposition; Heating Rate = 5°C/min

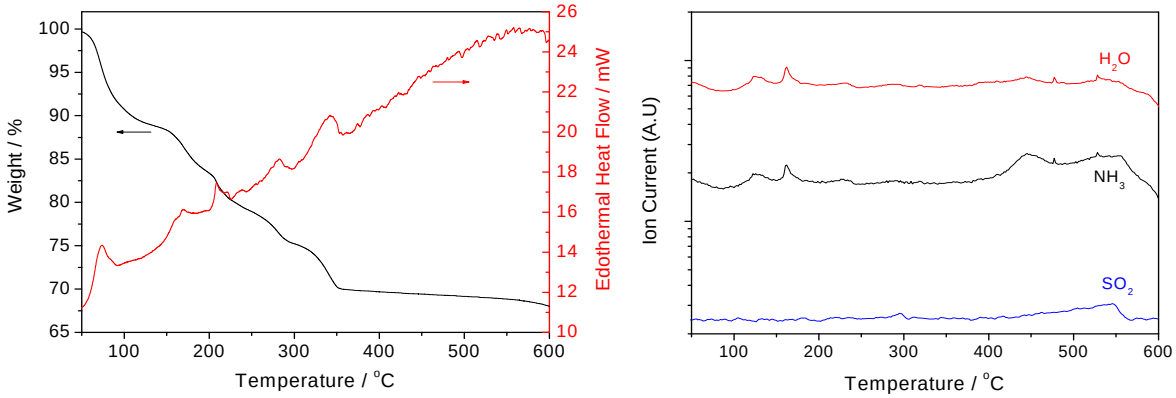

Figure 25. TG/DTA/MS Analyses of ZnO + $(NH_4)_2SO_4$ Decomposition, Mixture Molar Ratio x= ZnO:$(NH_4)_2SO_4$ = 1.5:1; Heating Rate = 5°C/min

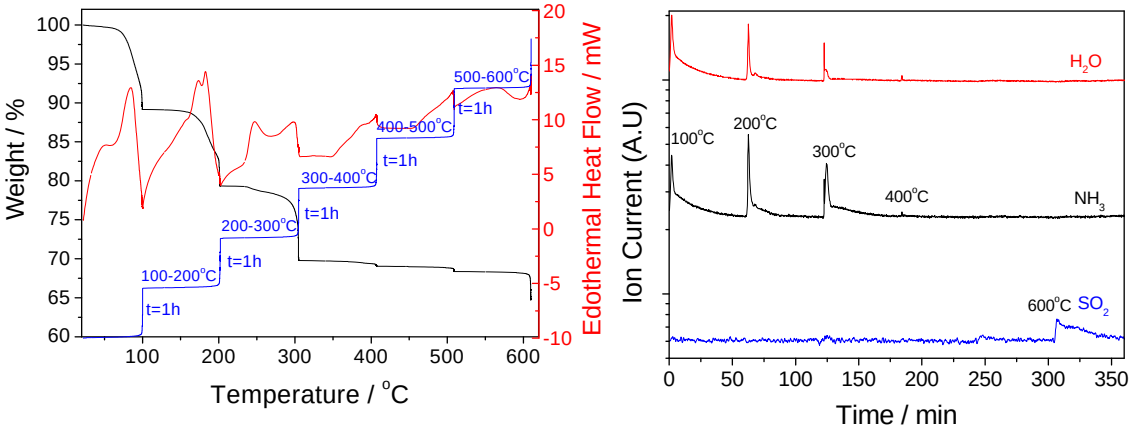

Figure 26. TG/DTA/MS Analyses of ZnO + $(NH_4)_2SO_4$ Decomposition; Mixture Molar Ratio x= ZnO:$(NH_4)_2SO_4$ = 1.5:1, Sample was Rapidly Heated (100°C/min) to a Constant Set Point (100°C, 200°C, 300 °C, 400 °C, 500 °C, and 600 °C) and Held at that Temperature for One Hour

The data of **Figure 24** to **Figure 26** indicate that:

- The main products of $(NH_4)_2SO_4$ decomposition (with or without added ZnO) were NH_3, H_2O, and SO_2 only (presence of oxygen was not monitored). Furthermore, the GC/MS-MS confirms that only NH_3 and H_2O were present in the products during the low temperature (lower than 500^oC) reaction.
- The decomposition mechanism of $(NH_4)_2SO_4$ in the presence of ZnO appears to differ from that of pure $(NH_4)_2SO_4$. When zinc oxide is present sulfur dioxide is released from $(NH_4)_2SO_4$ decomposition at higher temperatures (500-600^oC), while SO_2 evolves at much lower temperatures (less than 450^oC) when pure $(NH_4)_2SO_4$ is reacted. From process development point of view, it is advantageous to conduct $(NH_4)_2SO_4$ decomposition in the presence of added ZnO to allow a more facile separation of NH_3 from SO_2.
- The heating rate appears to have a significant effect on the decomposition of $(NH_4)_2SO_4$ in the presence of added ZnO. From process development point of view, it is advantageous to conduct $(NH_4)_2SO_4$ decomposition at low temperatures to allow complete NH_3 and H_2O removal, and then increase the reactor temperature (~900^oC) to evolve SO_2 and O_2.

The data presented above are in good agreement with the TPD-MS results presented in **Figure 27**. Again, it can be seen that the $(NH_4)_2SO_4$ decomposition products in the presence of ZnO at 250^oC are NH_3 and H_2O only (oxygen was not monitored). No evidence of N_2O, NO or SO presence was detected – as predicted from the chemical equilibrium calculations.

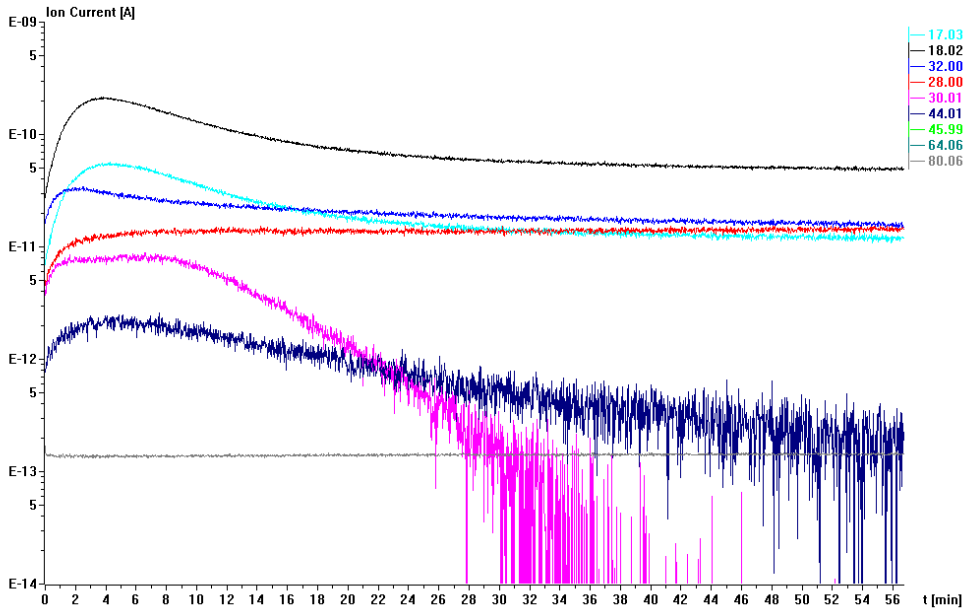

Figure 27. TPD-MS (TPD Instrument Linked to a Pfeiffer ThermoStar^{TM} Quadrupole Mass Spectrometer) Analyses of ZnO + $(NH_4)_2SO_4$ Decomposition at 250^oC; Mixture Molar Ratio x= ZnO:$(NH_4)_2SO_4$ = 1.5:1

3.4 Oxygen Production with All-Fluid Potassium Salt Sub-Cycle

Experimental work was performed at UCSD to demonstrate that the potassium sulfate/potassium pyrosulfate molten salt all-liquid/gas high-temperature sub-cycle proposed by FSEC was feasible. Initially, small samples were tested in a TGA/RGA system, but results were mixed. Therefore, a reactor system was built, as shown in **Figure 28**, capable of processing up to ~10 g of reactants to study the evolution of gaseous products under more realistic operating conditions. A residual gas analyzer was used to detect the gases from the reaction. As shown in **Figure 29**, RGA analysis of oxygen generation sub-cycle experiments were conducted to show the evolution of ammonia and water vapor at ~465°C, followed by evolution of sulfur trioxide at 500°C.

In addition to the chemical experiments, some basic data was recorded on the physical properties of the molten salts involved in the reactions. The viscosity of the molten salt streams that would be entering and exiting the mid-temperature reactor was measured. The melting points and densities were also measured. It was determined that the molten salts are liquid at the temperature levels proposed for the process, and it should be easy to pump these molten salts, with measured viscosities below ~8 cP as shown in **Figure 30**. Additionally, the melting point of the molten salts can be adjusted by addition of sodium salts to the potassium salt mixture. It was determined that it should be easy to pump these molten salts with viscosities below 5.5 cP at 450^{o}C.

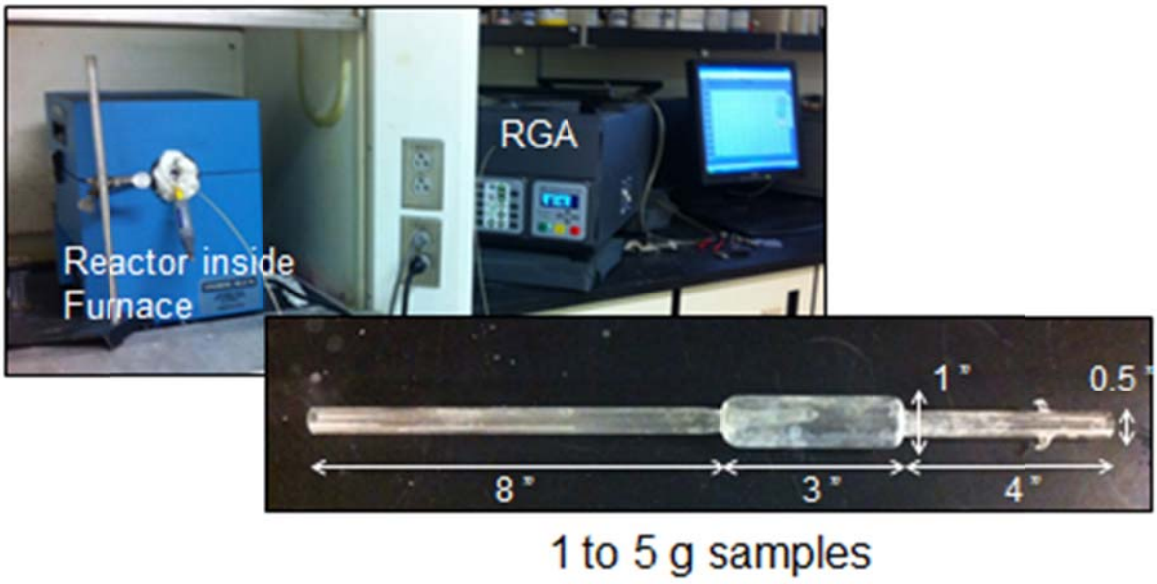

Figure 28. Thermochemical reactor system

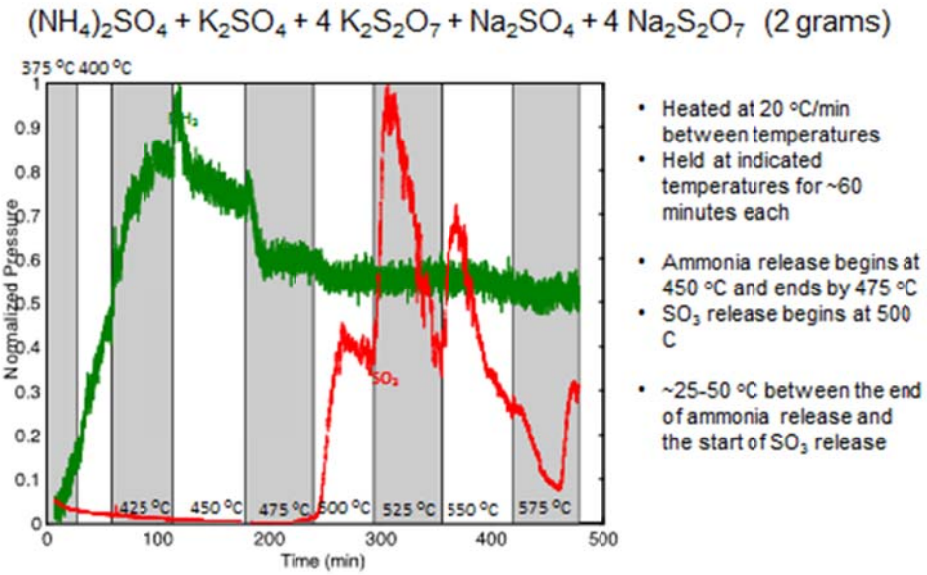

Figure 29. RGA Analysis of Oxygen Generation Sub-Cycle

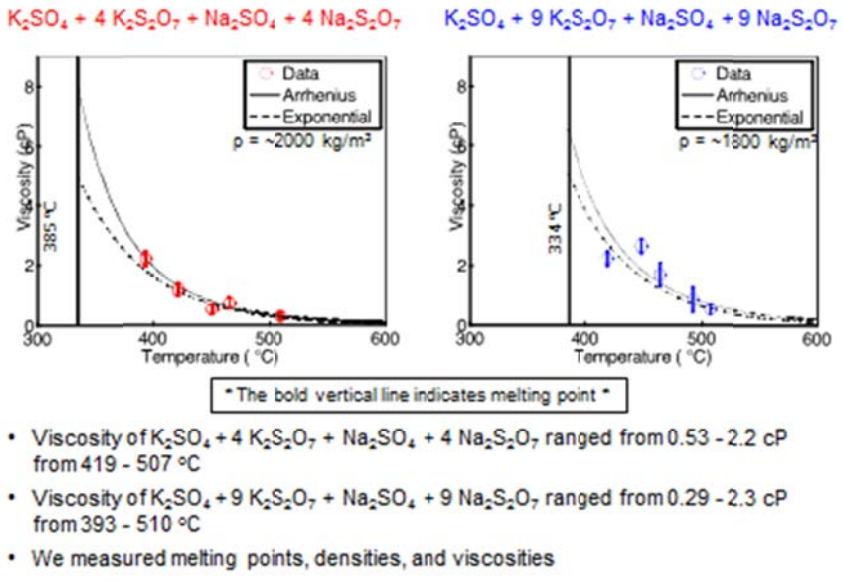

Figure 30. Data Showing Molten Salts Can be Easily Pumped

3.5 Thermochemical Cycle Analysis and Modeling

3.5.1 Stages of Process Development

The flowsheet of the SA process has undergone several iterations in reaching its present state. **Figure 31** traces the evolution of the process through the early stages when the process development was modeled by FSEC.

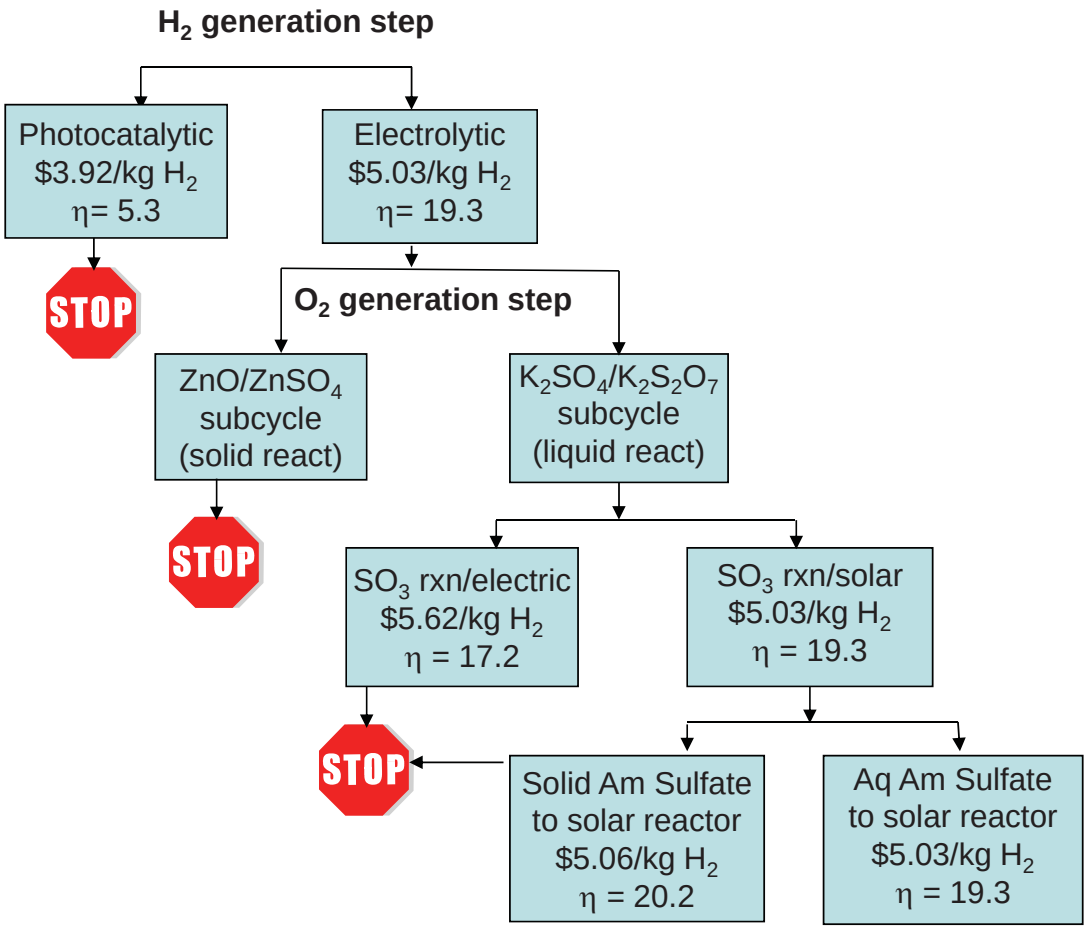

Figure 31. Evolution of the Sulfur-Ammonia Thermochemical Hydrogen Process

The sulfur-ammonia process splits water in two steps, a high temperature step in which oxygen is generated through the thermal decomposition of sulfur trioxide (or a surrogate),

$$SO_3(g) \rightarrow SO_2(g) + \tfrac{1}{2}\, O_2(g)$$

and a low temperature step in which hydrogen is liberated through the redox reaction of water with ammonium sulfite,

$$(NH_4)_2SO_3(aq) + H_2O(l) \rightarrow (NH_4)_2SO_4(aq) + H_2(g)$$

As originally conceived, the solar spectrum was to be split, with the high energy photons used to promote hydrogen generation on a photocatalyst while the infra-red portion of the spectrum was used to generate oxygen through the decomposition of zinc sulfate,

$$ZnSO_4 \rightarrow ZnO + SO_2 + \tfrac{1}{2}\, O_2.$$

The zinc sulfate being formed through the reaction of zinc oxide with ammonium sulfate,

$$(NH_4)_2SO_4(aq) + ZnO + H_2O \rightarrow ZnSO_4(aq) + 2NH_4OH(aq)$$

Figure 32 shows the overall flow diagram for this process. Unfortunately, devices capable of splitting the solar spectrum and directing it toward the two energy uses are very expensive and the decision was made to employ a solar tower to power the thermal portion of the process and a separate one sun photocatalytic array for the hydrogen liberation step. Since the photolytic step can make use of only a fraction of the solar spectrum, the overall solar energy to hydrogen energy efficiency fell below the DOE targets so the program changed direction to explore the electrolytic option. Even though the solar to hydrogen efficiency was low, the process did have a relatively low hydrogen cost and the photocatalytic process may warrant further investigation.

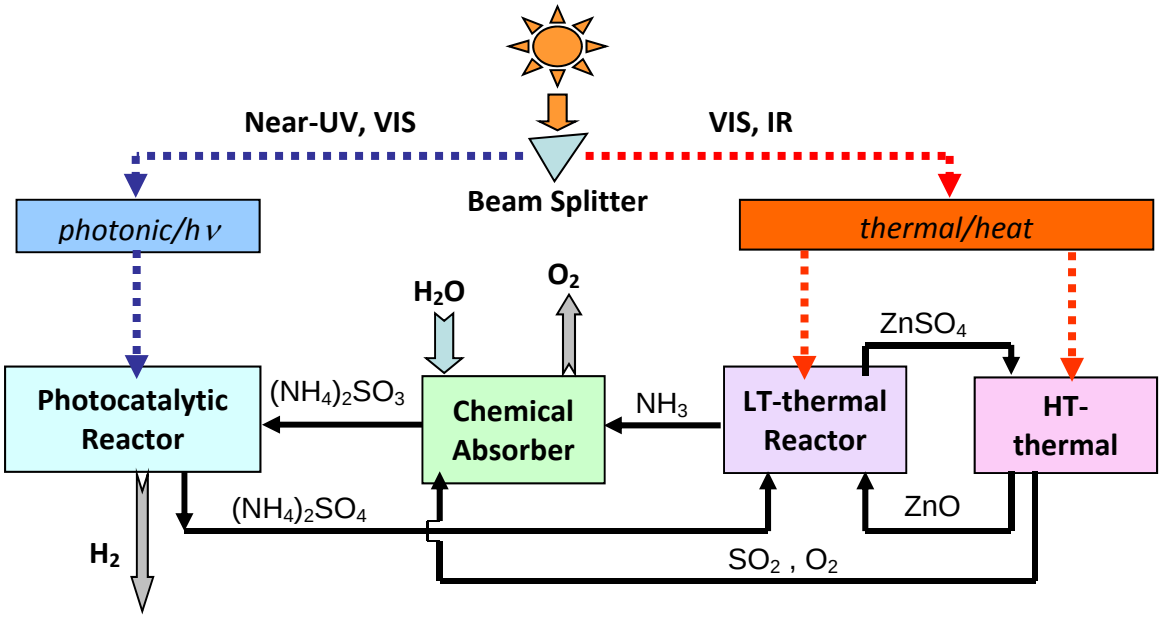

Figure 32. Photocatalytic Version of SA Process with Zinc Oxide Subcycle

The overall hydrogen liberation reaction via electrolysis is the same as for photocatalysis but the mechanism is entirely different. Details of the electrolysis are given in Section 3.2 and a simplified flow diagram for this version of the process is given in **Figure 33**.

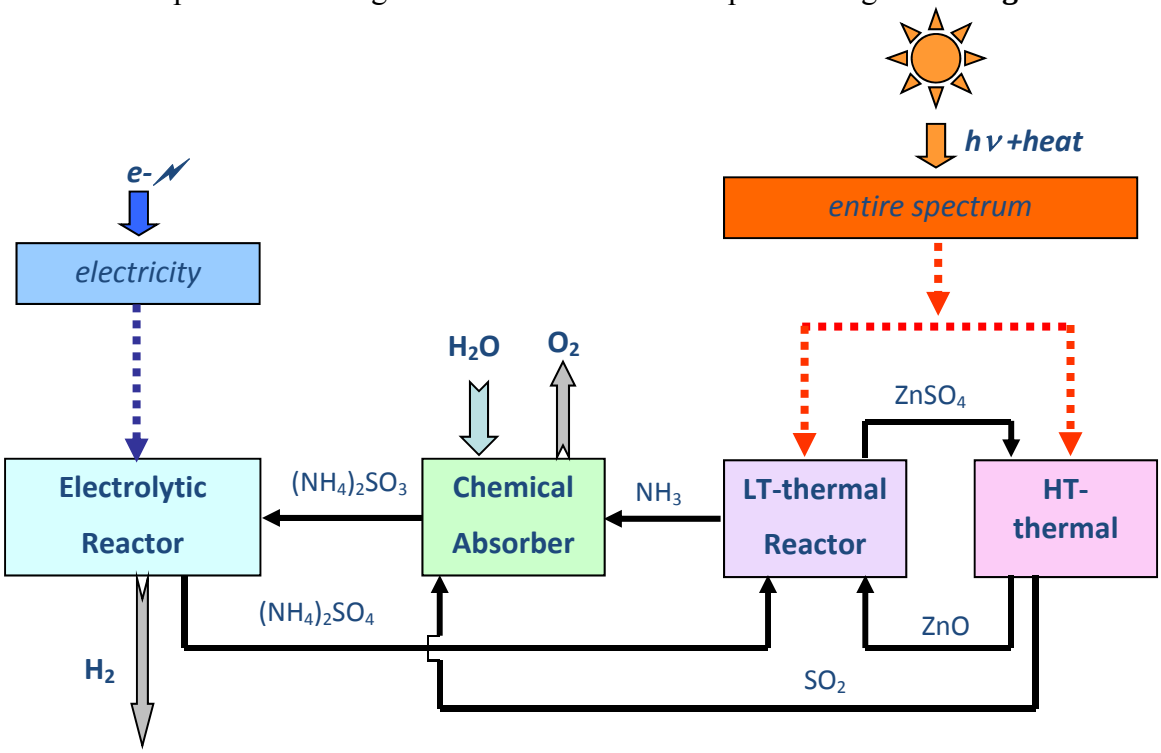

Figure 33. Electrolytic Version of SA Cycle with Zinc Oxide Subcycle

Both of these versions of the process have a common problem. It is difficult to retrieve the zinc sulfate without evaporating all of the water in which the ammonium sulfate is dissolved. If a sulfate could be precipitated from solution harvesting the dry sulfate would be relatively straightforward. Unfortunately, the insoluble sulfates ($BaSO_4$, $CaSO_4$) require temperatures in excess of 1600°C. This means that all the water and ammonia must be evaporated away from the metal salt requiring a great deal of energy. Additionally, solids handling is very expensive in terms of maintenance, downtime and manpower. Once it was discovered that an all-fluids process was possible and its applicability to the S-A process was evaluated, the metal sulfate process option was abandoned.

The all-fluid version of the S-A process (**Figure 34**) relies on the ability of potassium sulfite to absorb sulfur trioxide from ammonium sulfate to form potassium pyrosulfate accompanied by the vaporization of the ammonia and the containing water:

$$(NH_4)_2SO_4(aq) + K_2SO_4(l) \rightarrow 2NH_3(g) + K_2S_2O_7(l).$$

At higher temperatures the potassium pyrosulfate liberates sulfur trioxide and at still higher temperatures the sulfur trioxide decomposes into sulfur dioxide and oxygen. This process variation does not eliminate the necessity of vaporizing all of the water accompanying the ammonium sulfate but it does eliminate the solids handling and allows the sulfur trioxide decomposition to occur at lower temperatures than with the metal sulfate. It also permits power recovery from the vaporized water and ammonia. Not shown on the simplified flow diagram is the scheme used to recover the energy from the vaporized water and ammonia. The low temperature reactor was operated at 400°C, 9 bar while the chemical absorber was operated at one bar. A power recovery turbine was used to recover energy from the hot gases.

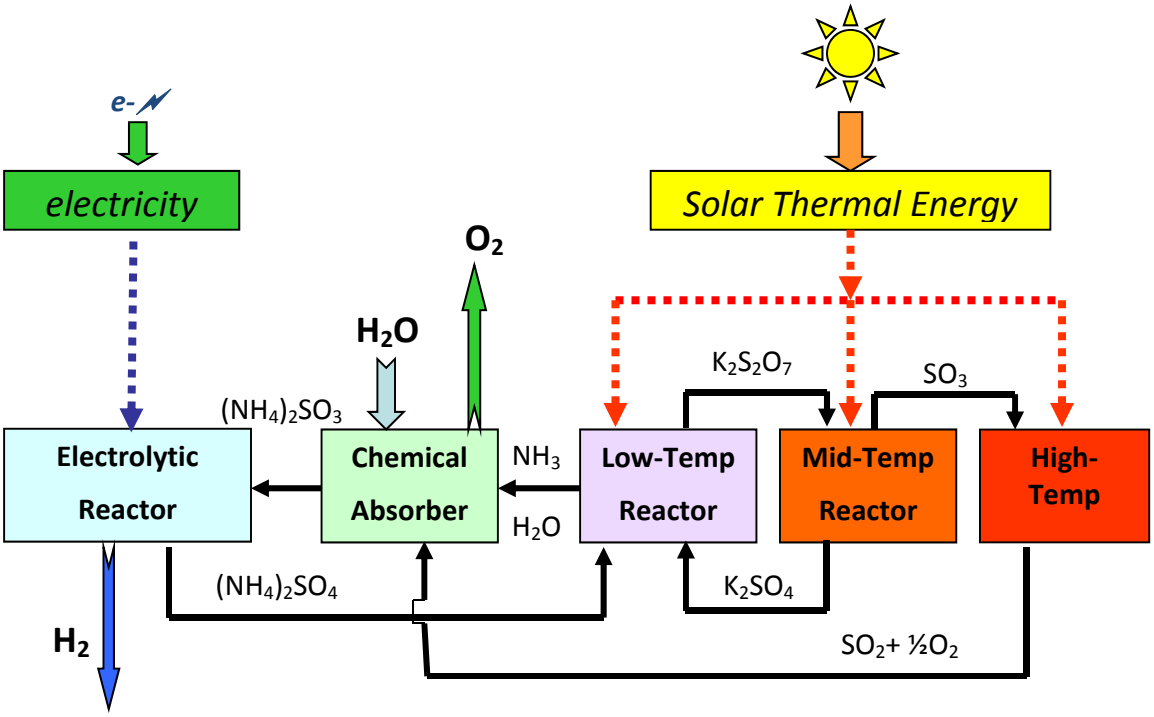

Figure 34. All-Fluid Version of the SA Process

Upon making these significant changes in the process, changes in the team were necessary and new subcontractors were added. A fresh thermodynamic based analysis of the process feasibility was conducted. This study used the computational tool HSC Chemistry and incorporated the database. **Figure 35** shows the flow diagram used in the assessment. The assessment assumed that the hydrogen plant would operate "around the clock" and not just during daylight insolation. All waste heat was assumed to be recovered in a separate steam power plant. Thermal storage for the "around the clock" operation was via the hot potassium sulfate/potassium sulfite molten salt mixture. The power recovery system was not designed but the efficiency of heat to power conversion was a parameter of the analysis. The Second Law efficiency was calculated as a function of the electrolyzer voltage and the overall efficiency of electrical production from waste heat. For a second law efficiency calculation the hydrogen is valued at its Gibbs Energy.

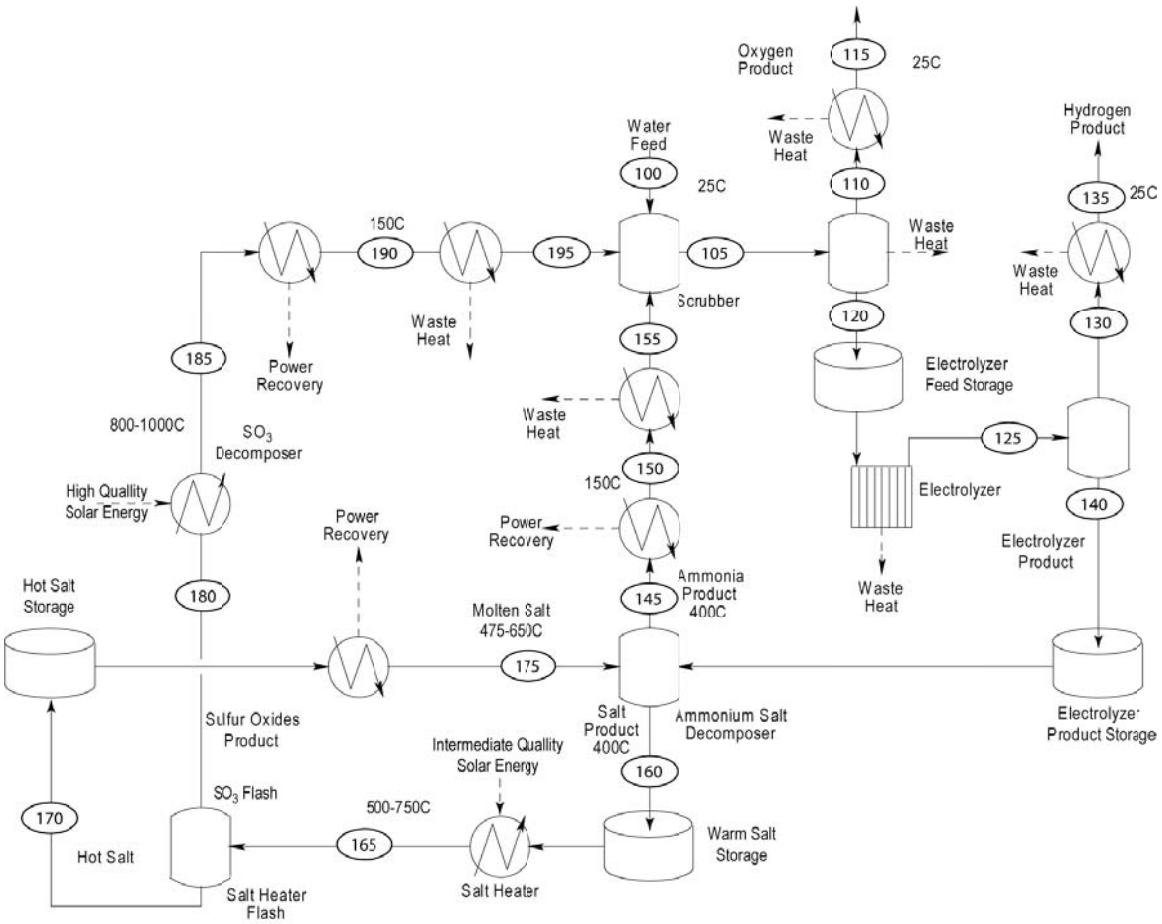

Figure 35. Flow Diagram for Thermodynamic Assessment

When valuing hydrogen at its Gibbs Energy, the theoretical maximum efficiency is that given by Carnot. In this analysis both hydrogen and electricity are of equal value. These results are presented in **Figure 36** to **Figure 38** for SO_3 decomposer temperatures of 800°C, 900°C and 1000°C, respectively. The comparison of these projections with the ultimate results of the design study is quite good if one assumes the lowest electrical production efficiencies considered.

There were a number of changes initiated with this study that were carried forward into the subsequent detailed analysis. Although the power recovery on the chemical vapors of the low temperature reactor gave high efficiency, its use cannot be justified on practical grounds. Not only would development costs for a power recovery turbine on a corrosive stream be excessive, the stream would contain some sulfur dioxide from the decomposition of ammonium sulfite. The ammonium sulfite would reform upon cooling and condense on the turbine blades leading to potentially catastrophic failure. The arbitrary stoichiometric mid-temperature reactor was replaced by a true thermodynamic reactor on the basis of literature data. Moreover, composition of the potassium

sulfate/sulfite salt was chosen on the basis of the equilibrium SO_3 vapor pressure at the operating temperature.

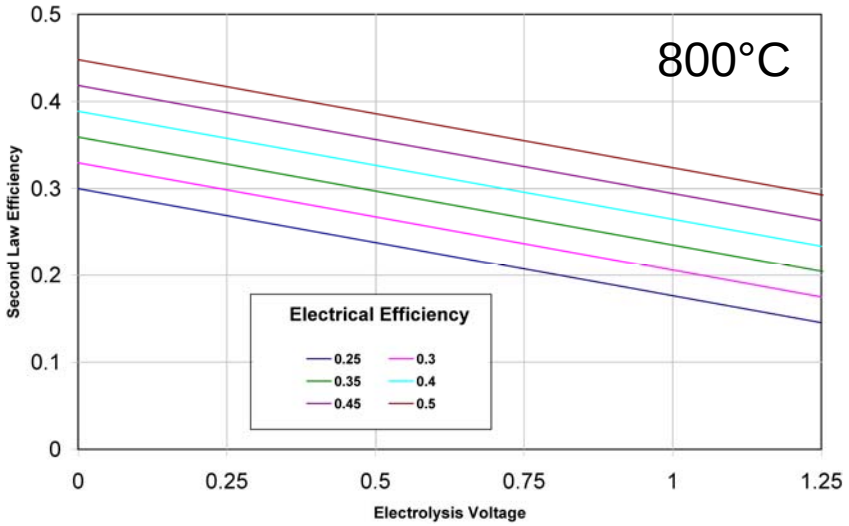

Figure 36. Second Law Efficiency for an 800°C Decomposer

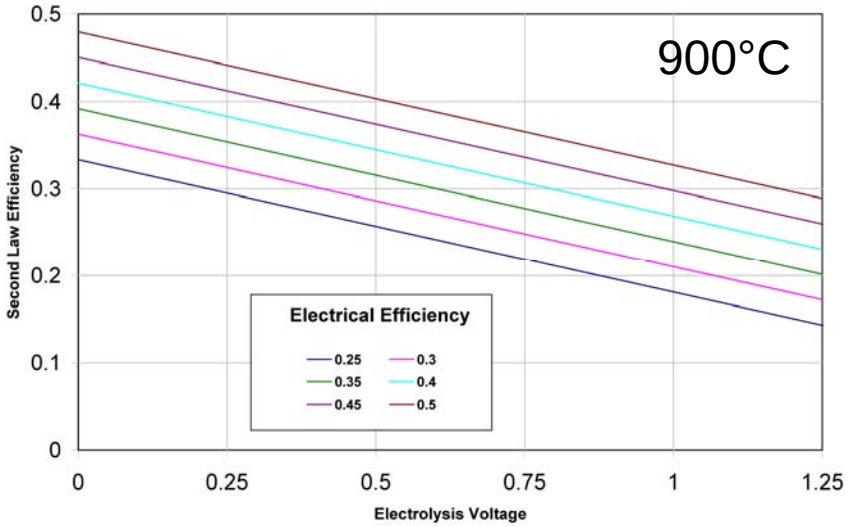

Figure 37. Second Law Efficiency for a 900°C Decomposer

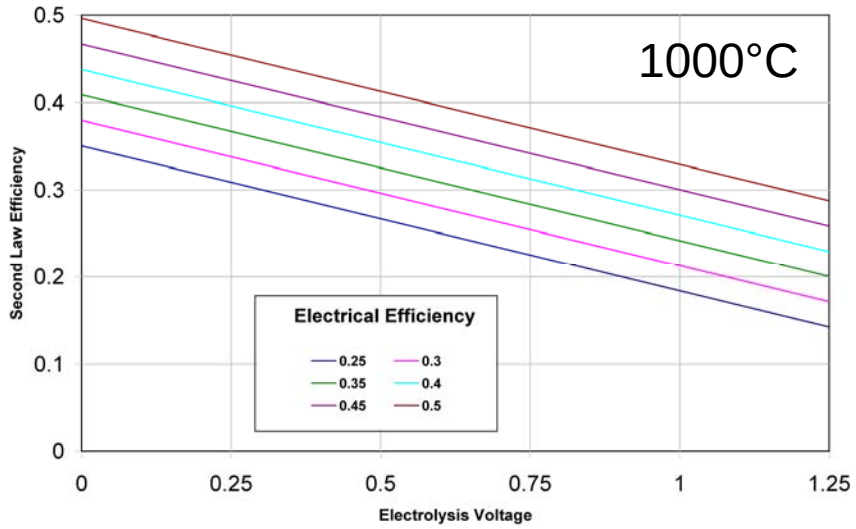

Figure 38. Second Law Efficiency for a 1000°C Decomposer

Starting with the thermodynamic analysis, the process was completely redesigned using equilibrium thermodynamic models and steam power plants designed for maximum efficiency. One major change was the replacement of the molten salt thermal storage with a phase change storage system based on sodium chloride. Also, in the course of the analysis it was observed that only 13% of the total energy requirements were for SO_3 decomposition. Changing the process to use electrical heat for SO_3 decomposition simplified the solar interface by requiring a single receiver (at lower temperature) and, most importantly, allows the complete plant, not just the hydrogen generating portion of the plant, to operate ”around the clock”.

3.5.2 Final Process Design

Figure 39 shows the simplified block flow diagram of the final process. A more detailed process flow diagram of the final process is shown in **Figure 40**. This is still a simplified form of the actual Aspen Plus flow diagram. For clarity it leaves out the equipment used to purify and recover chemicals from the hydrogen and oxygen product streams. Details of the sodium chloride heat storage system are also not included.

The easiest way to comprehend the totality of the process is to follow the sulfur through the system. This is, in fact, the way that the process simulation actually proceeds. The best place to start is with the aqueous product of the hydrogen electrolyzer [unit 1 in **Figure 40**]. During the electrolysis, where hydrogen is generated, ammonium sulfite is transformed into ammonium sulfate. The theoretical electrolysis voltage approaches infinity as the ammonium sulfate fraction approaches one. Of course this can never happen as some other electrochemical process, such as oxygen generation will occur first. The electrolysis system will be controlled such that 95% of the sulfur will be as sulfate with the balance as sulfite. The water content of the stream is controlled by water addition to the process thus defining this stream in total. The electrolysis product is

heated by countercurrent contact with the gaseous product of the high temperature decomposer while flowing to the Low Temperature Reactor [unit 2 in **Figure 40**].

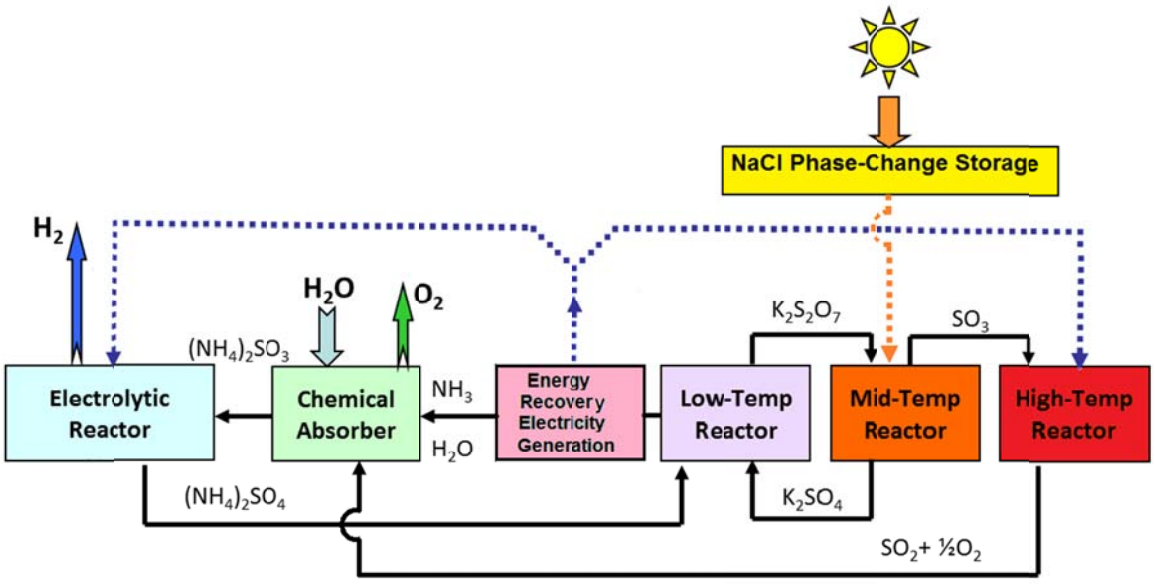

Figure 39. Block Flow Diagram of Final SA System

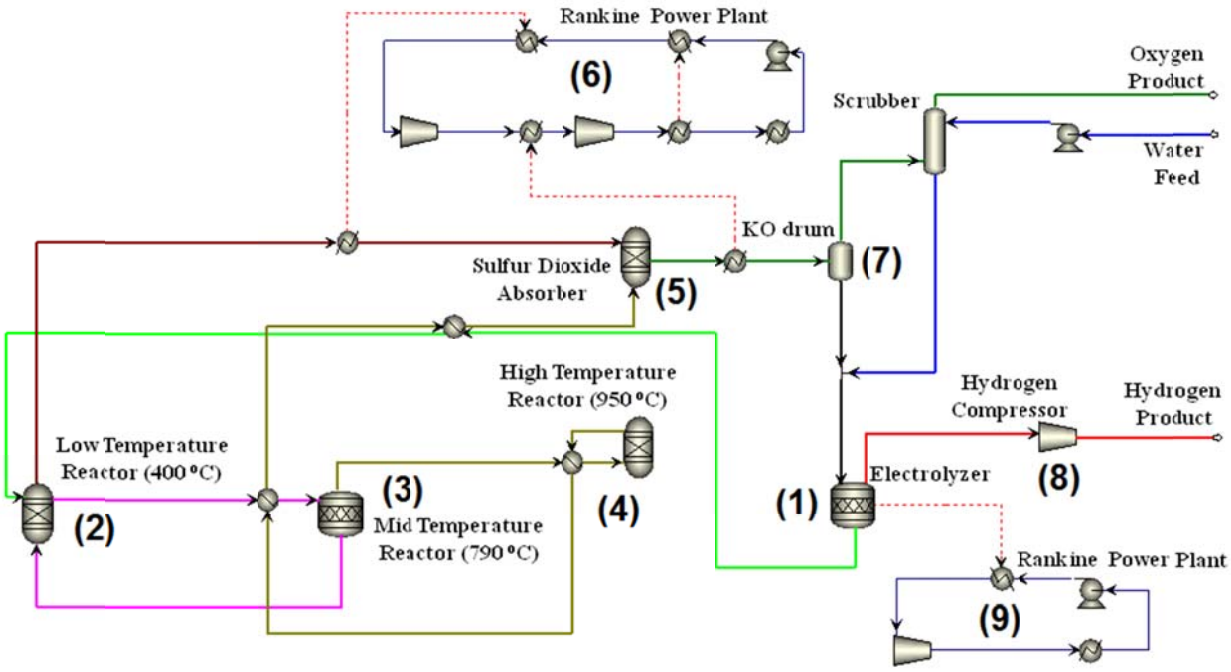

Figure 40. Process Flow Diagram of Final System

In the Low Temperature Reactor, or more properly the SO_3 absorber, SO_3 from the decomposition of ammonium sulfate, is absorbed in the sulfate-pyrosulfate molten salt. The salt is simulated in the model as a mixture of potassium sulfate and potassium pyrosulfate due to the availability of thermodynamic data but the potassium represents an equal molar mixture of potassium and sodium. The mixture is used to extend the possible operating range below the nominal 400°C temperature of the Low Temperature Reactor. The Low Temperature Reactor is adiabatic, the heat required to vaporize the ammonia and water being provided by the sulfate/pyrosulfate molten salt.

The molten salt is partially heated by recuperation of the decomposer off-gas but most of the heat is provided by heat exchange with the sodium chloride phase change energy storage system. This heat duty is shown associated with the Mid Temperature Reactor [unit 3 in **Figure 40**]. The Mid Temperature Reactor actually consists of a heat exchanger and a phase separator. The peak temperature of the Mid Temperature Reactor is limited by the melting point of sodium chloride to less than 801°C. All of the heat to the process is provided by this single thermal link to the storage system.

The highest temperature of the process is at the High Temperature Reactor (SO_3 catalytic decomposer) [unit 4 in **Figure 40**]. The decomposer is electrically powered using internal silicon carbide resistance elements so that the entire process can operate "around the clock" using stored energy. The SO_3 from the Mid Temperature Reactor is recuperated against the SO_2/O_2 product of the decomposer to minimize the amount of electric power required for decomposition. The decomposer only requires about 13% of the total heat input to the process. Once products leave the catalyst bed the reaction is frozen and the products cannot recombine as the stream is cooled. The operating temperature of the decomposer is the result of a tradeoff; at higher temperatures the reaction tends towards completion but at the expense of higher electrical consumption.

The decomposer product and the off-gas of the Low Temperature Reactor combine in the Sulfur Dioxide Absorber [unit 5 in **Figure 40**] to reconstitute the ammonium sulfite/sulfate feed to the electrolyzer. A great deal of heat is recovered, both from the sensible heats of the streams and from the heats of reaction and solution. This heat is recovered in the main Rankine Power Plant [unit 6 in **Figure 40**]. The oxygen remaining after the scrubber is cleaned of any remaining SO_2 or NH_3 in the Knock Out Drum and O_2 Scrubber [unit 7 in **Figure 40**]. All the water consumed by the process enters via this scrubber and a similar hydrogen scrubber (not shown) which is associated with the Hydrogen Compressor [unit 8 in **Figure 40**] used to deliver the product at pipeline pressures. Also note that the electrolyzer power is required to provide kinetic driving force and not chemical potential. This means that this power must exit the process as waste heat. This heat is recovered in a separate low temperature Rankine Power Plant [unit 9 in **Figure 40**].

A study with the Aspen Plus model showed that the best working fluid to use in Rankine cycles was ammonia in order to match the cycles to the process streams. Stoichiometric (RSTOIC) reactor blocks were used to simulate reactions with known extents of reaction and phase equilibrium data. Electrolyzer and mid-temperature reactor blocks were also

RSTOIC. Another RSTOIC reactor block was used to simulate a small side reaction in the absorber that involves dissolved oxygen. Gibbs (RGIBBS) reactor blocks were used to simulate reactions where kinetics were unknown. The chemical absorber, low-temperature and high-temperature reactors were RGIBBS blocks. Heat exchanger blocks were used to simulate heat exchangers. Coolers and heaters were used in the power-generating cycles, as well as to simulate heat exchangers between the main cycle and the Rankine cycles. Pumps were used to simulate pressure change in the liquid streams and in the Rankine cycles. Compressor blocks were used to compress the hydrogen product and to simulate the turbines in the Rankine cycles. Mixer and separator blocks were used to combine and separate material streams.

3.5.3 Efficiency

Different operating parameters were studied in order to maximize the plant's overall thermal efficiency. Plant pressure, ammonia salt concentration, and the high-temperature reactor operating temperature were varied to determine the combination of the operating parameters to achieve maximum overall efficiency. All studies were normalized to 1 kmol/s rate of hydrogen production so that they could be compared on a common basis.

The efficiency of the process was calculated based on DOE's working definition of efficiency. The efficiency is calculated by the following equation:

$$\eta = \frac{LHV_{H_2}}{Q + \frac{E}{\eta_E}}$$

where LHV_{H2} is the lower heating value of H_2 equal to 119.96 MJ/kg H_2, Q is the total heat input to the cycle, E is the total electrical input into the process, and η_E is the efficiency at which imported electricity is produced.

3.5.4 Pressure and High-Temperature Reactor Operating Temperature Studies

Plant pressure was varied from 7 to 13 bar. The high-temperature reactor operating temperature was varied from 900°C to 1200°C. The ammonia salt concentration was kept constant at 4 M and additional electricity needed was generated with 50% efficiency. Efficiency was higher at lower pressures. This is due to the fact that decomposition of sulfur trioxide is favored according to LeChatelier's principle, which increases the amount of hydrogen produced.

Figure 41 illustrates the effects of plant pressure and reactor temperature on plant efficiency. As plant pressure increased from 7 to 13 bar, the total power required decreased from 262 to 256 MW. At higher pressures, less water was lost to the oxygen scrubber, thus slightly less energy was required to operate the plant. At a constant pressure, as the high-temperature reactor operating temperature was increased the power generated by the Rankine cycles decreased. At a constant high-temperature reactor operating temperature, the power generated was higher at higher pressures. The low-temperature reactor ammonia vapor product, that is also the working fluid in the Rankine cycles, condenses at higher temperatures at high plant pressures, thus more energy is generated.

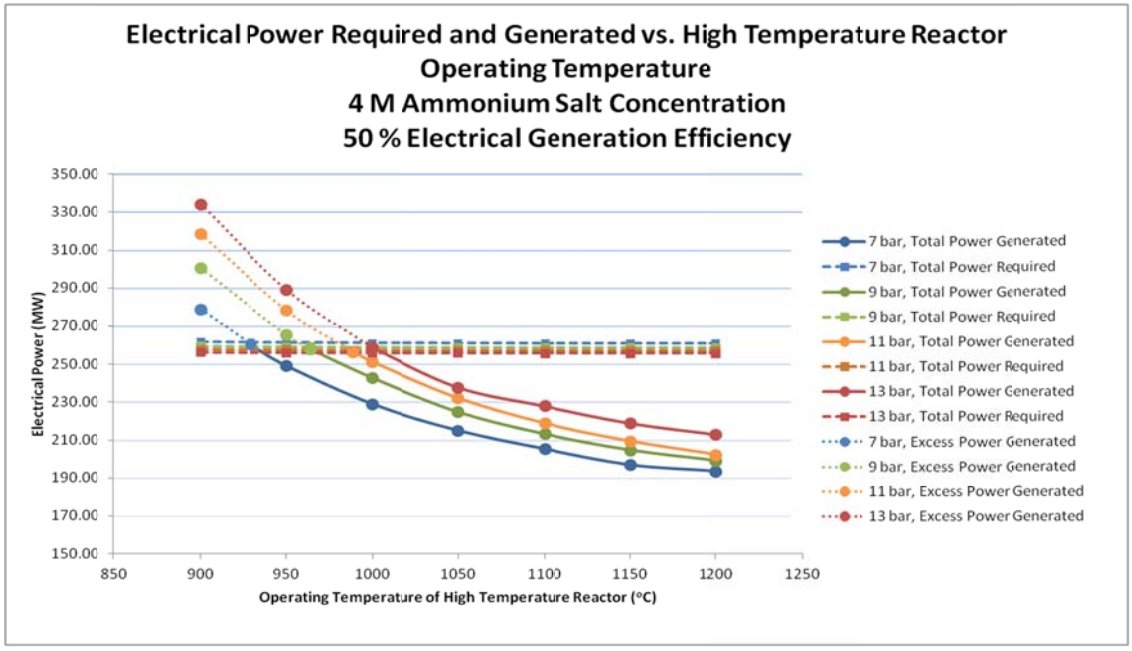

Figure 41. Effects of Plant Pressure and High Temperature Reactor Operating Temperature on Plant Efficiency

Figure 42 illustrates the effects of the plant pressure and high-temperature reactor temperature on electrical power required and generated. When the power required at a given pressure equals the power generated, no electrical power needs to be imported to the plant

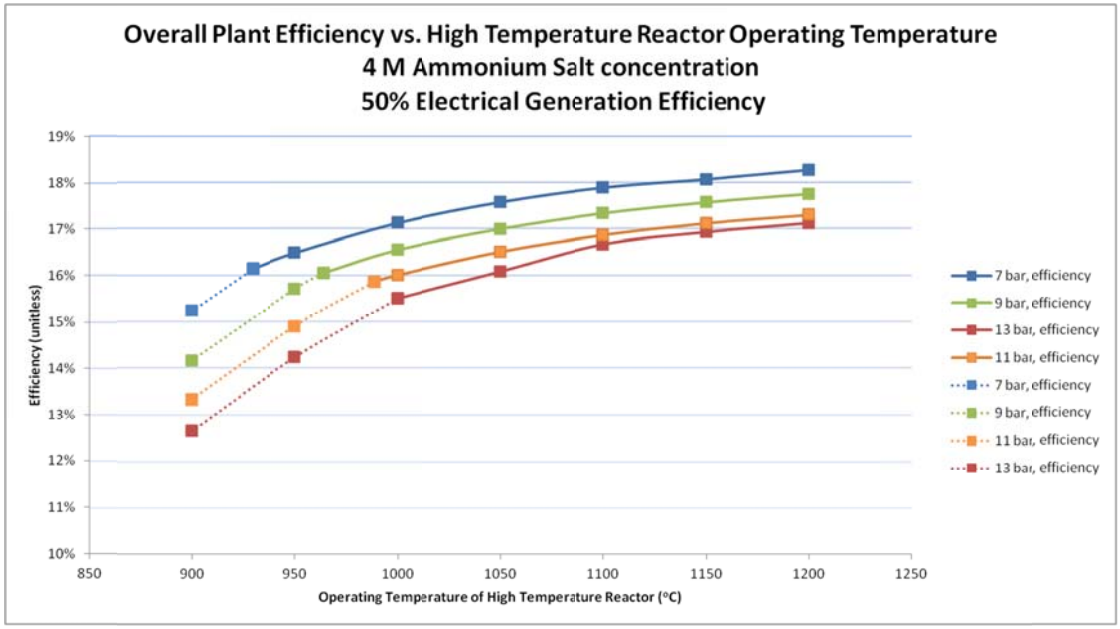

Figure 42. Effect on Electricity Required of High Temperature Reactor Operating Temperature and Pressure

At a 4 M ammonium sulfate concentration, plant pressure of 9 bar, and high-temperature reactor operating temperature of 1200 °C, an efficiency of 18% can be achieved with an additional 59 MW of energy generated with 50% efficiency. At 4 M ammonium sulfate concentration, plant pressure of 9 bar and the high-temperature reactor operating temperature of 966 °C, an efficiency of 18% can be achieved with no need to import additional electricity.

3.5.5 Ammonium Sulfate Salt Concentration Studies

Ammonium sulfate concentration was varied from 2 to 6 M while the plant pressure was kept constant at 9 bar. High-temperature operating temperatures of 1150°C, 1050°C, and 966°C, were considered. For all trials, the overall plant efficiency peaked at ~19%. As the ammonium sulfate concentration was increased, the efficiency increased, then peaked at ~19% and then decreased, as shown in **Figure 43**. Also, the same peak efficiency could be accomplished at either a lower ammonium sulfate concentration and higher high-temperature reactor operating temperature combination, or at a higher ammonium sulfate concentrations and lower high-temperature reactor operating temperature. For example, for both 5 M concentration at 1150°C high-temperature reactor temperature and 5.8 M ammonium sulfate concentration at 1050°C high-temperature reactor temperature the efficiency peaked at ~19%.

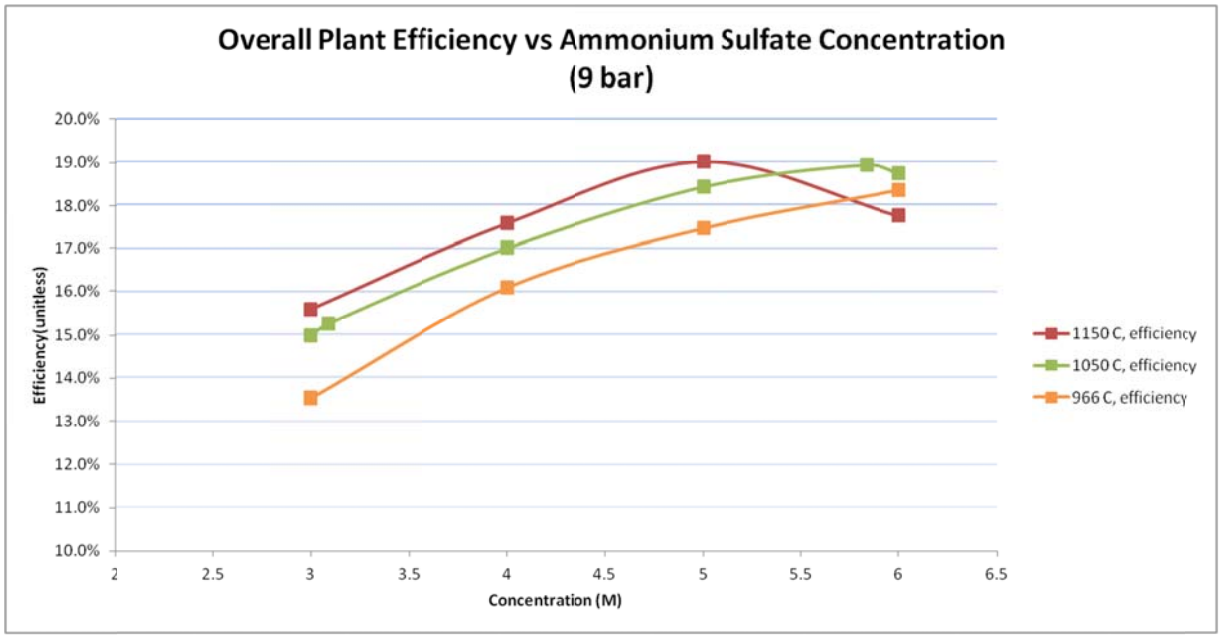

Figure 43. Effects of Ammonium Sulfate Concentration on Plant Efficiency

The effects of ammonium sulfate concentration on electrical power required and generated are illustrated in **Figure 44**. As ammonium sulfate concentration was varied from 2M to 6M, the amount of power required decreased by about 0.01 MW, as the pump work to pump the water feed decreased, as less water was circulating in the system at

higher ammonium sulfate concentrations. Power generation was reduced as the concentration increased, because less ammonia was circulating in the Rankine cycles. At higher high-temperature reactor operating temperatures, less power was generated and the intersection of power required and power generated occurred at higher concentrations.

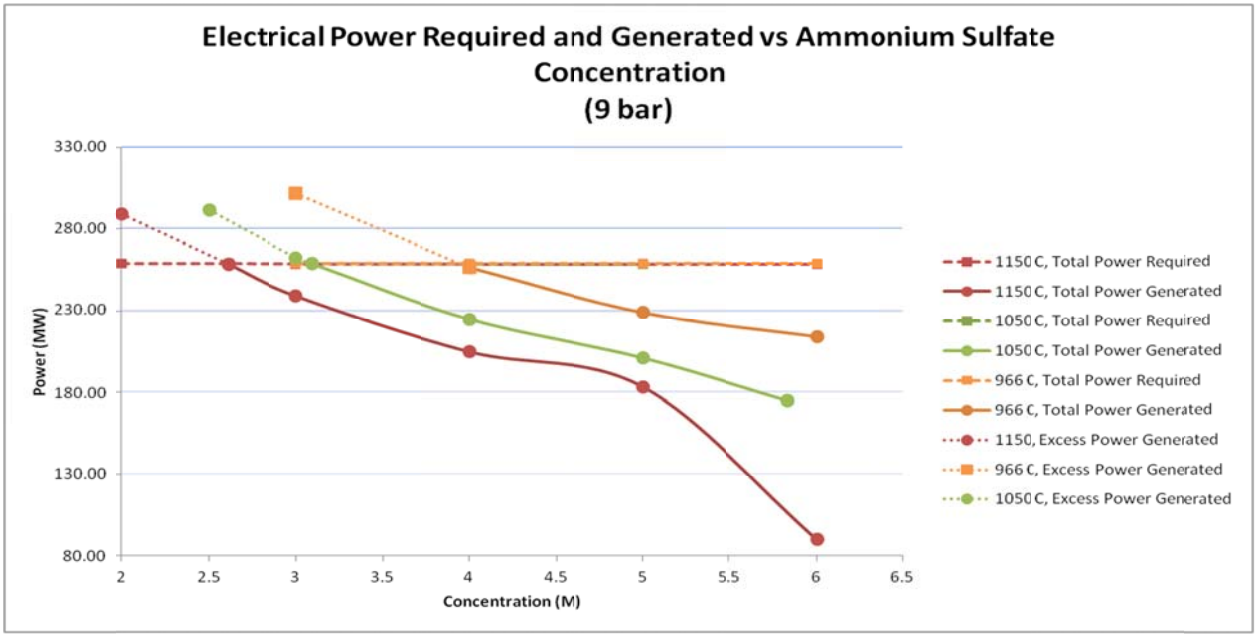

Figure 44. Effect of Ammonium Sulfate Concentration on Electrical Power Requirements

3.5.6 Mass and Energy Balance

Mass and energy balances were performed for the case with the following operating parameters: 4M ammonium sulfate concentration, 9 bar plant pressure, and 966 °C high-temperature reactor operating temperature. Both mass and energy balances were consistent. **Table 8** shows the simplified mass and energy balances, using the lower heating value (LHV) of hydrogen. Table A.1. in Appendix A has a detailed mass and energy balance that includes manually-torn recycle streams. Most of the energy losses were from the Rankine cycle condensers, as shown in **Figure 45**.

Table 8. Mass and Energy Balance (Energy Basis for Material Streams is LHV of Hydrogen)

Energy Balance			**Mass Balance**	
Energy In (MW)				**Mass In (kg/sec)**
Mid Temp. Reactor Solar Thermal Input	1489		Water Feed	20
Low Temperature Reactor Energy Input (Adiabatic)	0		**Total**	20
Electricity Import	0			
Water Feed	0			**Mass Out (kg/sec)**
Total (MW)	1489		Oxygen Product	18
			Hydrogen Product	2
Energy Out (MW)		% Subtotal	**Total**	20
Hydrogen Product Separator	21	2%		
Rankine Cycle 1 Condenser	999	83%		
Rankine Cycle 2 Condenser	162	13%		
Electrolytic Reactor Heat Loss	21	2%		
O2 product	0			
Subtotal:	1203			
H2 product	286			
Total (MW)	1489			

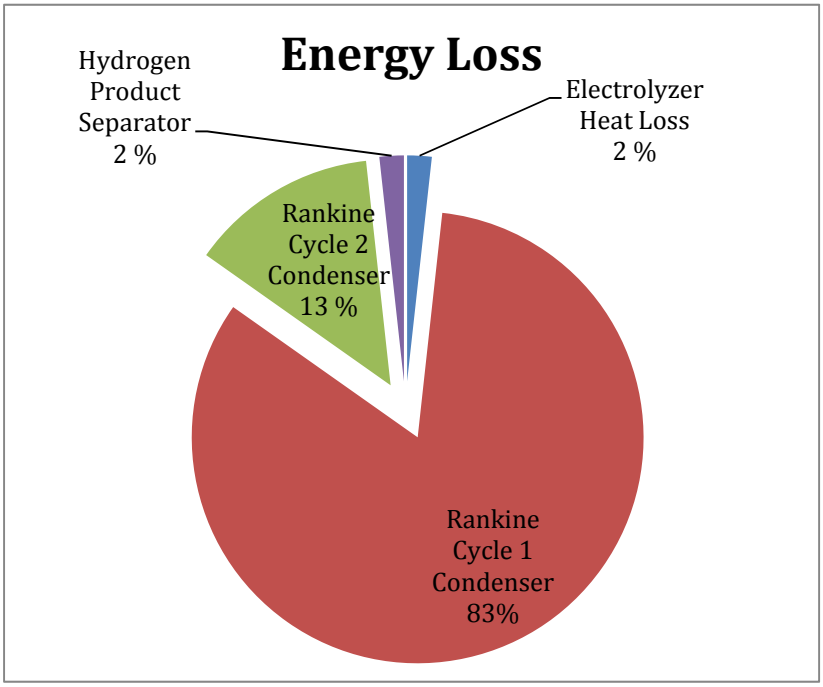

Figure 45. Pie Chart of Energy Losses of the SA Plant

3.6 Solar Concentrating System Analysis and Modeling

3.6.1 Solar Collector System Configuration

At the beginning of the project, results from the chemical experiments were evaluated and a set of requirements for the solar portion of the system was developed. Preliminary analysis of the characteristics and requirements of the solar collector field for the SA cycle were performed. There are competing requirements for the solar collector field:

- Due to the high temperatures involved in the oxygen evolution step, only concentrating systems are feasible for conducting those reactions. The difficulties of transporting, distributing, and processing solid materials in a field of dishes, and the scale of a large central hydrogen plant makes a heliostat/central receiver the most feasible option.
- The hydrogen evolution process involves one-sun illumination of the photoreactor near ambient temperature. This would be best accomplished with a flat-plate collector configuration that is also a photoreactor – fabricated using polymeric materials.
- The concept originally proposed used a beam-splitting approach to separate the high-energy photons utilized in the photoreactor from IR radiation used in the thermocatalytic reactions. This concept increases the solar energy-to-hydrogen conversion efficiency of the process by allowing the UV and IR portions of the spectrum to be used efficiently. So, consideration was given to the implementation of hot- or cold-mirror systems for splitting the solar spectrum directed to the reactors.

Several collector configurations were proposed and evaluated, involving dishes, heliostats, and hot and cold mirrors. The configurations were as follows:

- Dish concentrator with hot mirror reflector, thermal receiver at the focus, and photoreactors flat behind the parabolic dish.
- Dish concentrator with full spectrum mirrors and a thermal receiver at the focus, but with a cold mirror reflector near the dish focus and a cylindrical photoreactor concentric to the dish axis and outside the diameter of the dish.
- Conical concentrator with hot-mirror reflector, a line-focus thermal receiver along its axis, and a photoreactor flat behind the conical reflector.
- Heliostat field with hot mirror reflectors and a thermal receiver on the tower, with photoreactors on the heliostat behind the hot mirrors, or on the ground beneath the heliostats.
- Heliostat field with full-spectrum mirrors focused on a thermal receiver on the tower, with a separate field of flat-plate photoreactors.

These configurations are shown in the sketches of **Figure 46**.

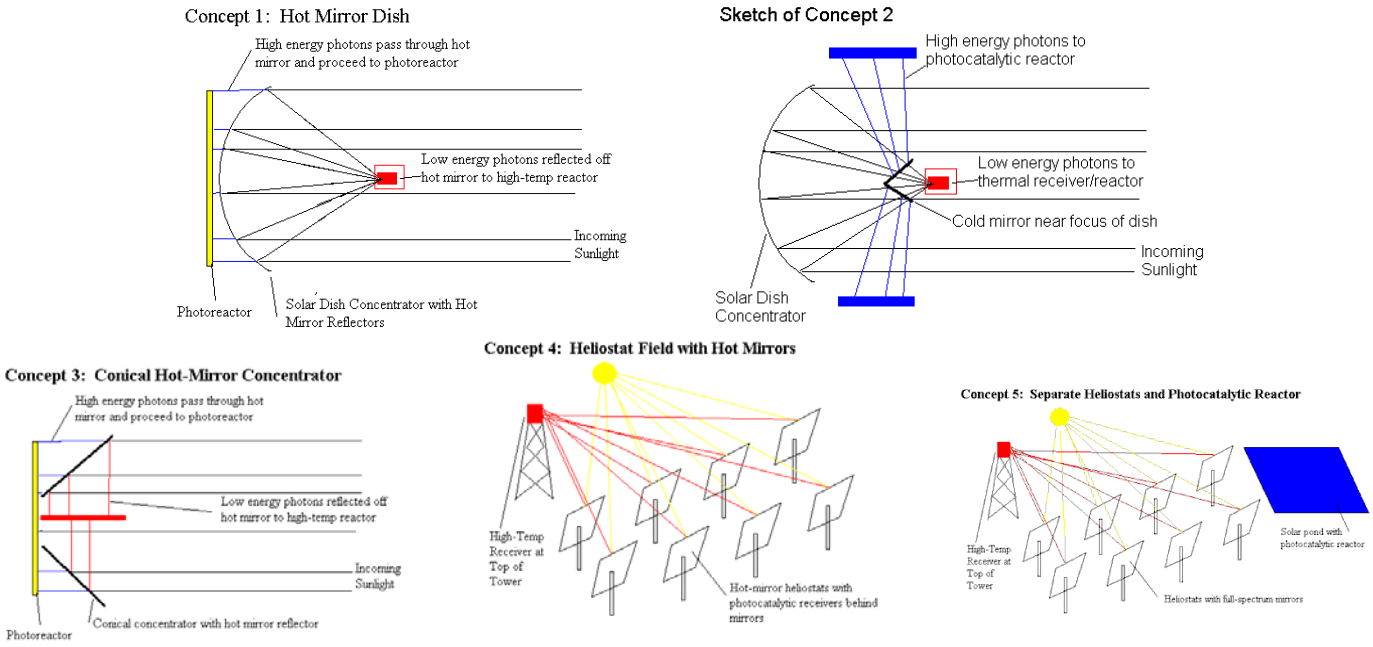

Figure 46. Preliminary Solar Field Configurations Evaluated by SAIC

A preliminary evaluation of the positive and negative features of each configuration was carried out, with the results shown in the following table:

Table 9. Collector Configuration Evaluation

Positive Features	Negative Features
#1: Dish concentrator formed from hot mirrors. Photocatalytic reactor directly behind hot mirrors. Thermal reactor at focus of dish.	
All solar components on a single tracker	Limited in scale-up to perhaps 100-200 sq.m unit size
Minimizes hot mirror area (about 110% to 120% of aperture area)	Reactors and other equipment must move with dish
	Difficult to keep photocatalytic reactors up to temperature
	Hot mirrors very costly; hard to produce in large sizes or quantity
	Complex shape (double-curvature) of hot mirrors could be costly

#2: Dish concentrator with full-spectrum mirrors. Conical cold mirror near dish focus at 100-500X concentration redirects high-energy photons to cylindrical reactor along axis around dish perimeter. Thermal reactor at focus of dish.

All solar components on a single tracker	Limited scale-up beyond 100-200 sq.m aperture size
Minimizes cold mirror area (1-2 sq.m) for 100 sq.m unit size	Reactors and other equipment must move with dish
Cylindrical photoreactor can be mounted parallel to sunlight at front edge of dish so it doesn't shade or block	Double reflection of high-energy photons, and reflection/transmission of low-energy photons will reduce total available energy for reactions 20-25%
Simple shape of cold mirror - cone	
Cold mirror has approx. 45 degree incidence angle which is preferred	

#3: Conical hot mirror with 45 degree opening angle. Photoreactor immediately behind hot mirror. Thermal reactor at line focus along axis of cone.

All solar components on a single tracker	Limited scale-up beyond 100-200 sq.m aperture size
Simple hot mirror shape (single curvature)	Reactors and other equipment must move with dish
Simple thermal reactor geometry (tube with screw feeder) for feeding solids	Conical concentrator can give 1200 suns, but linear receiver would be difficult to bring to temperature because of large view factor to outside (no cavity).
Can adjust solar flux on photoreactor by having it follow cone or having it flat at exit aperture of cone.	Hot mirrors very costly; hard to produce in large sizes or quantities
Hot mirror has 45 degree incidence angle	

#4: Heliostat field with fixed thermal reactor at top of tower. Reflectors are hot mirrors. Photoreactor behind mirrors on heliostats or on ground under heliostats.

Thermal reactor doesn't have to move; easier transport of materials to/from reactor	Need 20-40% more hot mirror area to make up for cosine effect
Easily scaled to large sizes (100MW+)	Need to disperse and collect chemicals through heliostat field
Heliostat field could be mounted (floated?) over "solar pond" photoreactor, allowing high-energy photons to go through	Photoreactors in different areas of the field will have differing solar input due to cosine effect
	Hot mirrors very costly; hard to produce in large sizes or quantity. Solar input varies significantly during the day

#5: Solar dish/power tower with full-spectrum mirrors and thermal receiver at focus. Separate photoreactor in the form of a solar pond.

No hot/cold mirrors needed	Doesn't directly utilize spectrum-splitting but still uses "quantum boost" in photocatalytic reactor
More effective heating of thermal reactor with retention of high-energy photons (+20%) and no transmission losses through cold mirror (+10-20%)	Lower solar "efficiency" because separate collectors take up ~twice the area
Low-energy photons and solar pond construction provide heat to maintain photoreactor temperature	
Most components can be on the ground; only feed to/from thermal reactor must be routed to dish	
Thermal system and photoreactor can be independently sized to match their outputs based on efficiency	
System cost minimized by elimination of hot/cold mirrors, reduction of dish size (-40%) and photoreactor size (-10% to -25%), uses low-cost photoreactor	
Potential for 24/7 co-generation or use of heat from thermal energy in solar pond at 80-90C (energy from thermal photons plus excess quantum energy from photocatalytic process)	
Scale up easy -- thermal dish becomes power tower, solar pond gets bigger	

Further evaluation of these configurations led to elimination of all the dish concentrator concepts for full-scale systems due to material handling difficulties and lack of scalability. The separate central receiver/reactor system was found to provide some flexibility that could reduce the cost of hydrogen produced at the expense of solar energy conversion efficiency.

Later, another configuration was identified, in which a flat cold mirror at the top of the tower, near the receiver, would re-direct the UV-visible light downward to a flat-plate or pond-based photoreactor on the South side of the tower. Those photoreactors would therefore receive about two suns of UV-visible light, enhancing the output of the photoreactor system. This configuration is shown in **Figure 47**.

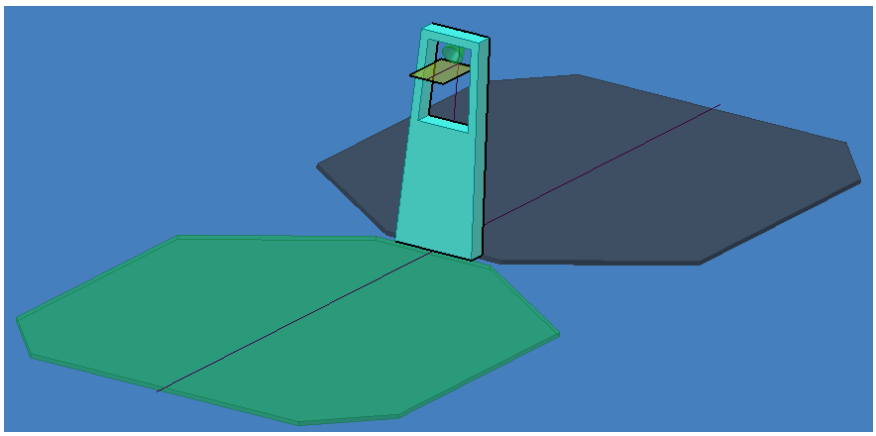

Figure 47. Solar Field Configuration with Cold Mirror Near Receiver and South-Field Photoreactor Field (Note: Left Foreground is North)

3.6.2 Solar Field Modeling

In order to quantify the performance of the solar field, a spreadsheet-based system performance model was developed by SAIC. The model divided the field into segments, and calculated the contribution of heliostats from each segment using TMY (Typical Meteorological Year) weather data [14]. That way, different field designs and shapes could be quickly and easily modeled and the total energy delivered by the field determined. Later, a storage element was added to the model, so that the effects of thermal storage could be included in the operational data.

TMY data for Barstow, CA was used for the analyses. TMY data sets are detailed, one-hour solar and weather data for a full year that are designed to typify a location as much as possible. As an example of the type of information available in the data files, **Figure 48** is a compilation of some of that data, showing the cumulative hours of sunlight as a function of the direct normal insolation level. The curves show that Barstow experiences about 1,800 hours per year of insolation levels above 800 W/sq.m. (red curve at 800 W/sq.m.), and over 6,000 hours per year with sunlight up to 600 W/sq.m. (blue curve at 600 W/sq.m.).

Similarly, **Figure 49** is a plot of the average direct normal insolation that can be expected in Barstow as a function of the sun elevation angle, including maximum values and values one standard deviation above and below the average. As shown in the figure, at a sun elevation angle of 30 degrees, one could expect about 640 W/sq.m. of direct normal insolation in Barstow, with a standard deviation of about 260 W/sq.m.

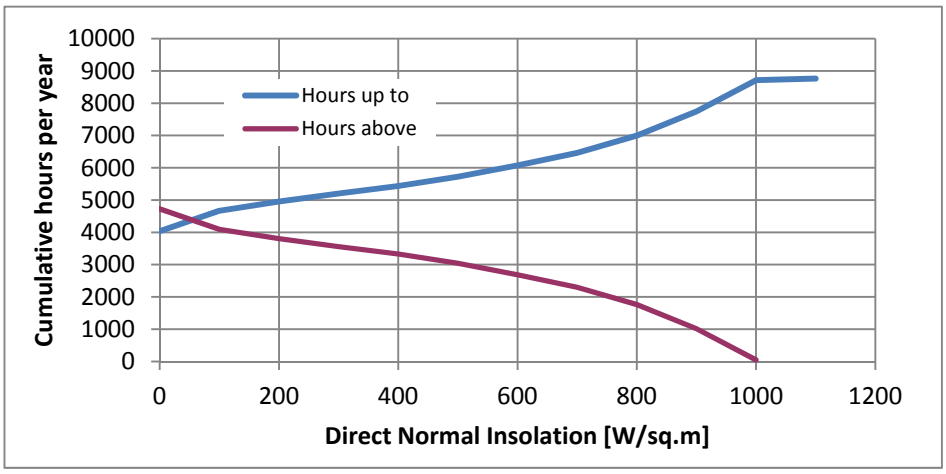

Figure 48. Compilation of Barstow, CA TMY Data

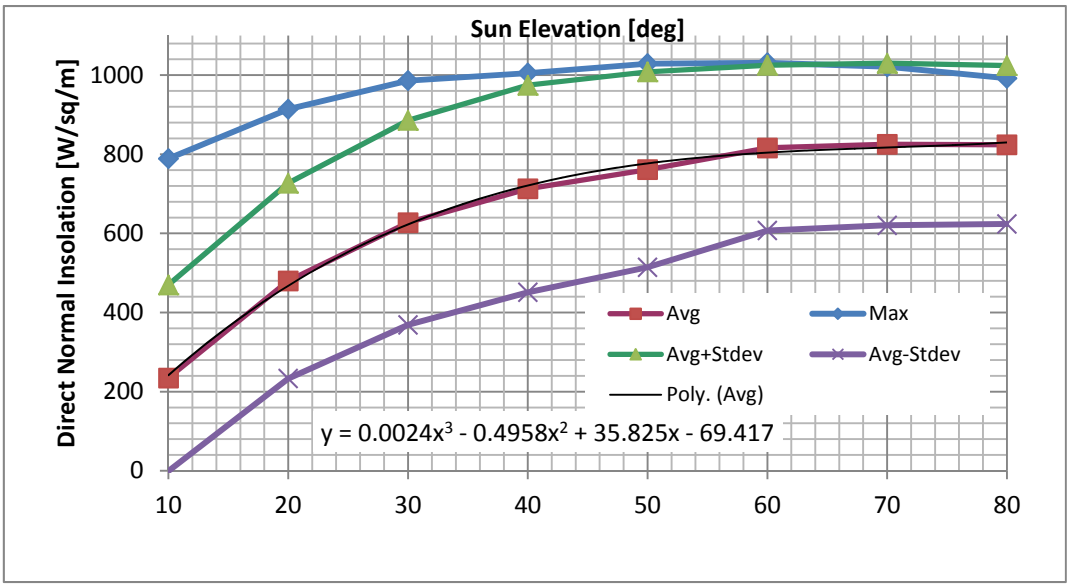

Figure 49. Direct Normal Insolation at Barstow, CA as a Function of Sun Elevation Angle (from TMY Data)

Using the TMY data, the performance of a heliostat in a particular location relative to a tower was calculated. The results of this single heliostat model included data such as that in **Figure 50**, which shows the distribution of energy delivery through the year for a heliostat at a particular location in the field.

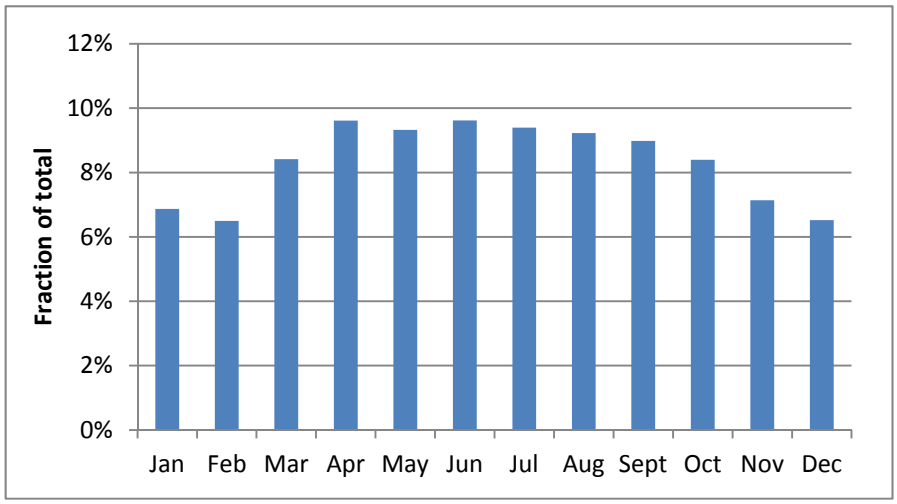

Figure 50. Monthly Distribution of Energy Output for a Single Heliostat

After completing analyses for heliostat locations all around a tower, the model result was a surface showing the energy delivery from a field of heliostats, including such considerations as atmospheric attenuation and the packing density of heliostats in different locations. **Figure 51** shows a plot of one of the outputs from the heliostat field model, in the form of the energy in kWh to be expected from a single square meter of heliostat reflector as a function of location around the tower (in tower heights). The tower location is at 0,0, and North is to the left in the figure. To aid in interpretation, the graph is colored with yellow showing high values and shading to blue at lower values. From this graphic one can see immediately the higher value of heliostats directly North of the tower.

	-7	-6.5	-6	-5.5	-5	-4.5	-4	-3.5	-3	-2.5	-2	-1.5	-1	-0.5	0	0.5	1
5																	
4.5																	
4							2,001	2,004	2,003								
3.5					2,009	2,021	2,030	2,036	2,040	2,037	2,025	2,007					
3			2,001	2,017	2,033	2,046	2,059	2,069	2,076	2,078	2,059	2,058	2,031				
2.5			2,016	2,035	2,053	2,070	2,087	2,102	2,113	2,119	2,118	2,105	2,083	2,053	2,001		
2		2,009	2,029	2,049	2,070	2,091	2,112	2,131	2,149	2,164	2,156	2,169	2,149	2,109	2,059		
1.5		2,017	2,039	2,061	2,084	2,108	2,131	2,156	2,180	2,204	2,224	2,211	2,199	2,188	2,116	2,034	
1	2,000	2,022	2,045	2,068	2,093	2,118	2,146	2,174	2,204	2,237	2,269	2,267	2,273	2,263	2,186	2,118	
0.5	2,001	2,023	2,047	2,071	2,096	2,123	2,152	2,183	2,217	2,254	2,297	2,321	2,361	2,319	2,185	2,188	2,023
0	1,999	2,021	2,044	2,068	2,094	2,121	2,149	2,181	2,215	2,255	2,298	2,344	2,367	2,352		2,204	2,021
-0.5		2,015	2,037	2,061	2,085	2,111	2,138	2,167	2,198	2,233	2,270	2,310	2,297	2,273	2,182	2,138	
-1		2,005	2,026	2,048	2,070	2,094	2,118	2,143	2,168	2,194	2,219	2,238	2,225	2,195	2,087	2,036	
-1.5			2,011	2,031	2,050	2,071	2,091	2,110	2,128	2,144	2,155	2,151	2,133	2,084	2,021		
-2				2,011	2,027	2,064	2,079	2,091	2,100	2,105	2,088	2,089	2,064	2,032			
-2.5					2,000	2,014	2,024	2,032	2,036	2,036	2,010	2,005					
-3																	

Figure 51. Expected Energy Delivery from Heliostats in a Central Receiver System at Barstow, CA

In addition to the graphical outputs, the model sums up the total energy, total concentration on the receiver, and other factors of interest in the design of a receiver/reactor and system.

The model was exercised to predict the size and output of the heliostat field needed for the solar thermochemical hydrogen system. As an example, **Figure 52** shows the hour-by-hour output from a solar field on a summer day and a winter day, which was used in calculating receiver and storage requirements and performance for the system.

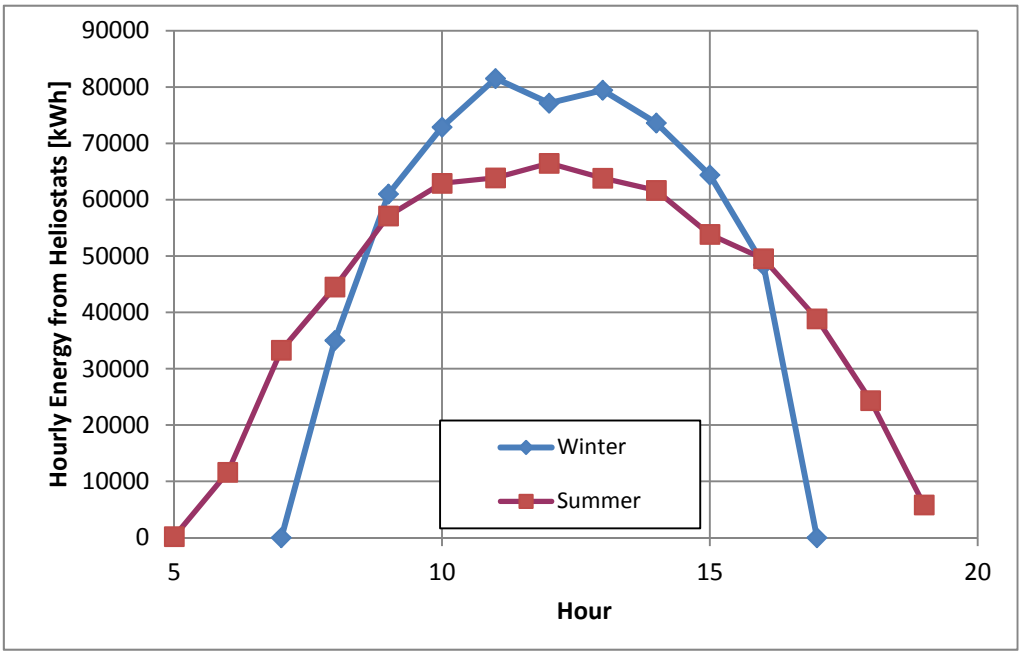

Figure 52. Hourly Energy Delivery from a Heliostat Field in Winter and Summer

3.7 Solar Concentrating System and Reactor Receiver Development and Design

3.7.1 Heliostat Cost Reduction

One clear conclusion from the initial collector evaluation was that the heliostats in a central receiver system are the major cost component of the system. SAIC identified a potential for cost savings in heliostat fabrication using glass-reinforced concrete (GRC) to replace much of the steel structure of the heliostats. Several design concepts were drawn together to produce a design with reduced system cost, as follows:

- Extremely low cost structural material (approximately $0.15/kg)
- Spray-up fabrication process on low-cost mold, with molded-in features such as ribs and mounting provisions
- Small size (10-15 m^2) to facilitate fabrication, transport, handling, installation, and maintenance
- Reduced wind loading due to ground-hugging design; sufficient mass in structure to limit foundation requirement for lift loads

- Factory assembled unit to reduce field installation labor
- Factory-produced, surface-installed concrete track foundation to minimize site preparation and installation costs while maintaining good accuracy
- Low-cost, low-power drive system
- Self-powered heliostat using PV panel for DC power to eliminate field power wiring
- Wireless communication to eliminate field control wiring

The result of all these innovations is a heliostat with a projected production cost well below $\$100/m^2$, compared to conventional heliostats at about $\$129/m^2$ for high volume production. **Figure 53** presents a computer image of a potential prototype design that was considered.

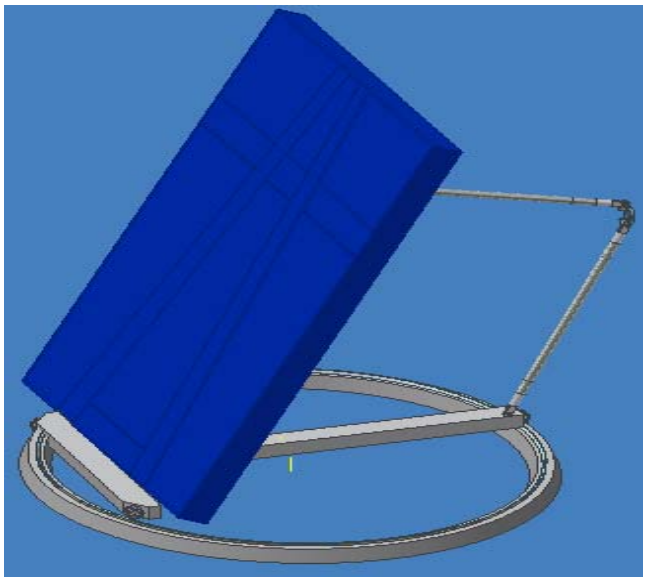

Figure 53. Glass-Reinforced Concrete Heliostat Design Concept

In order to test and quantify some of the design concepts, SAIC developed a design for, and fabricated, a half-scale prototype of the GRC heliostat concept. The prototype, although fabricated by hand, demonstrated many essential features of the concept, including molded-in reinforcements, simple mounting and drive mechanisms, and low-cost wireless controls. Unfortunately, planned operational testing of the completed prototype was not carried out due to budget constraints. Therefore, **Figure 54** shows a photo of the completed prototype GRC heliostat in the lab, but the unit was never tested.

Figure 54. Prototype GRC Heliostat

As part of the development of the GRC heliostat concept, a cost analysis was done for massproduction of the units.

Figure 55 shows a breakdown of the cost components of the heliostat if it were produced in large quantities. Due to the very low structure cost, the highest-cost items in the breakdown are the drive components (motors, gears, etc.) at 34% of the total cost, and the control electronics at 26% of total cost. The projected production cost, even at a very low production rate of only 100 heliostats per year, was less than $100/sq.m., significantly less than current-day production heliostats.

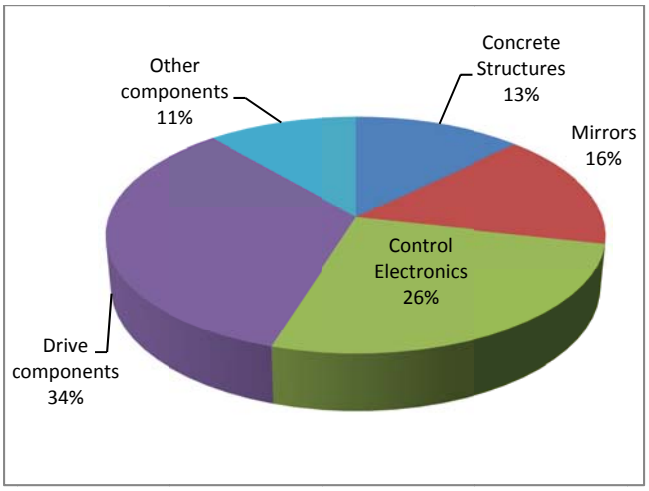

Figure 55. Breakdown of GRC Heliostat Costs

3.7.2 Reactor/Receiver Development

In the course of the project, several concepts for reactors and receivers were identified. Initial designs using the photocatalytic SA process also included concepts for very low-cost, efficient flat plate photocatalytic reactors. One design was developed based on earlier SAIC work on a solar water detoxification system. In that program, an air-mattress-type structure was used in tests of water detoxification, with heat-sealed thin films of polyvinylidene flouride (PVDF, trademark Kynar™) serving as the structure. PVDF has excellent weatherability and also high UV transmittance so it was seen as a good material for the photoreactors.

In terms of the high-temperature thermal reactors, standard solar central receiver designs were examined. For the SA process with ZnO subcycle, a reactor based on a solid particle receiver was contemplated to eliminate heat transfer issues from the solar receiver to the reactor components. After the all-liquid K_2SO_4 subcycle had been identified, receiver designs devolved to a more conventional molten salt design similar to solar central receiver power plants. Another concept that was examined for a period of time was separate low and high-temperature receivers to allow optimization of the heliostat field for the specific needs of the process.

Finally, the design of the chemical plant evolved to the final configuration, with phase change molten salt (NaCl) storage, continuous system operation, and electrical heating of the SO_3 decomposition reactor. Due to heat recovery and energy cascading within the process, the need for receivers at multiple temperature levels was eliminated, and the receiver design converged to a single sodium heat-pipe receiver system tied to the phase change storage system. This receiver system is detailed in the following section that describes the phase change storage system.

3.7.3 Phase Change Molten Salt Storage and Heat Transfer System

As the process modeling was being refined, heat exchange and energy cascading within the process were exploited to minimize the external heat required at intermediate temperatures. The resulting system had a need for energy at about 800°C, and all other heat needs were taken care of through heat recovery or cascading. To meet this energy need while providing for continuous operation of the chemical process plant, a phase-change storage concept was identified that appears to be a good match to the system requirements. This storage concept, first described and tested at lab scale by some Israeli researchers [15], is based on the phase change of sodium chloride salt (NaCl). The concept is pictured in **Figure 56** and described in the following paragraphs.

Sodium chloride salt melts at 801°C, making it an ideal match to the SA process needs. However, getting heat into and out of large volumes of phase change material can be challenging. Therefore, it was deemed important that the proposed concept also included a unique and efficient natural heat transfer system for getting energy out of the molten salt. That system operates as follows:

- A pool of molten sodium is allowed to float on top of the salt material, which it does readily due to the density difference between the materials and the low solubility of sodium in the NaCl melt. Note that the vapor pressure of sodium is almost atmospheric pressure at the temperature of the molten salt, so the containment vessel does not need pressurization.
- To extract heat from the system, liquid sodium evaporates from the surface of the NaCl, removing heat from the salt and causing it to solidify.
- The sodium vapor rises in the head space of the tank to a condensing coil or pipe, to which it gives up the heat like a sodium heat pipe, condensing and dripping back to the pool as a liquid.
- The NaCl that becomes solidified has a density much higher than the liquid NaCl, so it drops to the bottom of the tank naturally, exposing fresh molten salt to the pool of molten sodium.

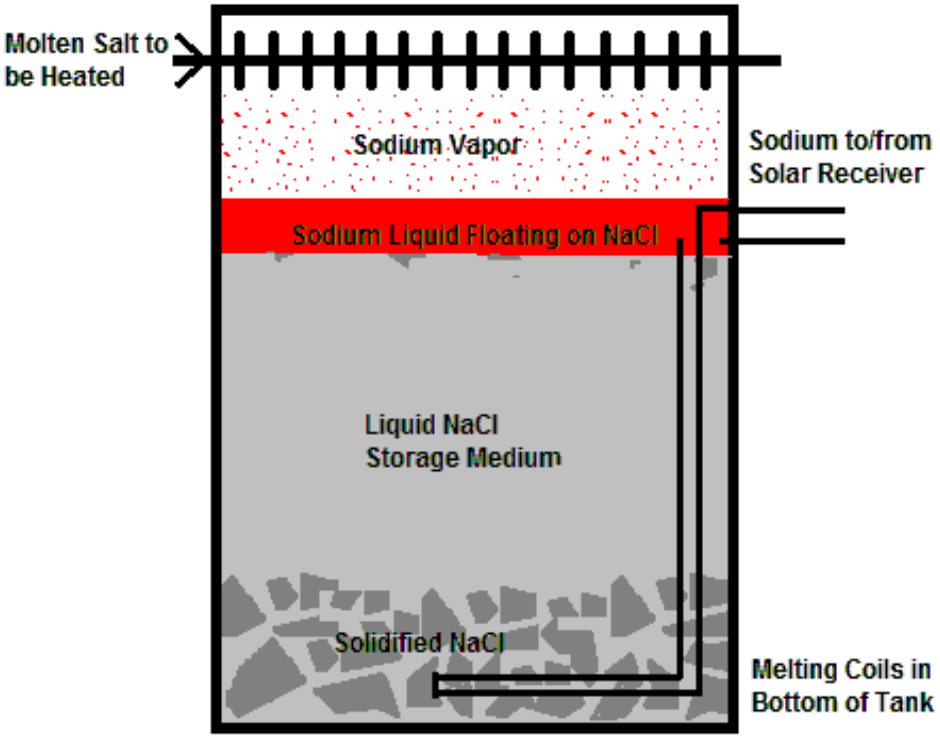

Figure 56. Molten NaCl Phase Change Storage Concept

Thus, the system includes a very efficient and naturally-driven heat transfer process. To put heat into the salt, a pumped sodium loop is envisioned, with coils at the bottom of the salt tank to melt the material, as shown in the figure.

As described above, the NaCl phase change system had been proposed and demonstrated at a laboratory scale by researchers in Israel. Research in the U.S. was also recently conducted by Infinia Technologies Corp. to evaluate the system for heat storage for a small dish/Stirling system. The testing at Infinia identified operational difficulties in the system, particularly with bridging of the solid salt across the top of the storage container during cool-down, leading to trapping and sequestration of the liquid sodium below solid layers of salt and a reduction in heat transfer.

To further investigate this phenomenon and address some potential solutions to the problem, UCSD engineering interns at SAIC looked at various characteristics of the phase change storage system and evaluated possible on-sun tests that could be conducted on the NaCl system using the SAIC dish concentrator system. The cost and complexity of working with the high temperature materials, sodium liquid, and other features of the tests made on-sun testing impossible in the budget and schedule available. However, the students were able to perform limited testing of a lower-temperature analog system, using paraffin for the phase-change material and isopropyl alcohol as the liquid heat pipe material, as described in the following sections.

3.7.3.1 Evaluation of On-Sun Testing Options

The objective of this activity was to design a prototype receiver to be placed on an existing 120 m^2 SAIC solar dish concentrator system in order to demonstrate proof of concept for the thermo-chemical production of hydrogen gas. The concept is to collect the thermal energy from the concentrated solar flux at the dish receiver and transport it to a thermal energy storage (TES) system, whence it can be delivered to the chemical process. The heat transport and TES systems are also applicable to generating electricity from concentrated solar power, as industry is currently researching improved methods for heat transport and storage.

The thermochemical SA hydrogen production process includes three separate reactors: one low temperature, one medium temperature and one high temperature. The thermal energy from the TES is used to drive the mid-temperature reactor at 790°C and electricity cogeneration within the chemical process will drive both the high temperature reactor and the electrolytic cell. A full scale system based on this concept would utilize a central tower receiver with a heliostat field, not a dish system. For this reason two parallel designs were undertaken; one using heat pipes and TES on the dish, which is better suited to a concentrating solar dish, and one with a pumped liquid metal loop with TES on the ground, which would more closely resemble the scaled up system.

3.7.3.2 Dish-Mounted TES System

The first design used heat pipes as the heat transfer mechanism to deliver thermal energy from the receiver cavity to the TES, which is situated directly behind the receiver at the focus of the dish. This design is illustrated in **Figure 57**.

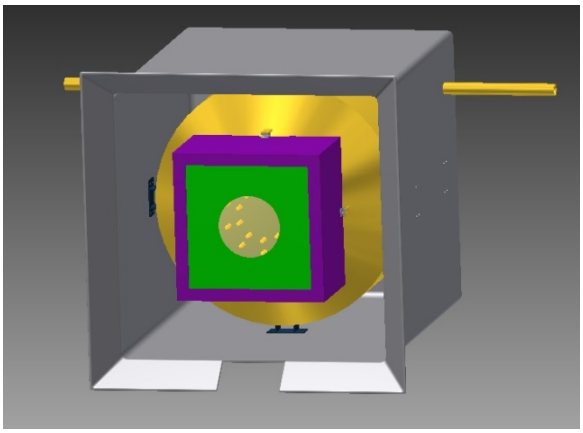

Figure 57. Solar Receiver with Heat Pipes and TES

The receiver cavity's geometry is that of a truncated cone in order to optimize solar flux and reduce convective losses. The aperture has a diameter of 25 cm, which is the same size as previous receivers used on the SAIC dish. The rear diameter of the cone is 45 cm, giving a rear area of 0.16 m^2 and a maximum solar flux of 622.5 suns. The linear distance from the aperture to the back plate of the receiver is 31.12 cm, meaning that the angle

from the generatrix lines to the axis of the cone is an angle of 18°. This value was chosen to ensure that the extreme rays from the dish, which approach the receiver at an angle of 36°, arrive precisely at the edge of the receiver's back plate. This ensures that the entire back plate of the receiver is directly heated, while minimizing spillage and convective losses by creating a deeper cavity.

The receiver cavity is constructed from a high temperature ceramic material such as Lava™ (alumina silicate) or Mycalex™ (glass-mica composite) which can not only withstand the extreme temperatures and intense solar flux found at the focus of the dish, but also act as thermal insulators, thereby reducing thermal losses and increasing the system's thermal efficiency. This component can be machined or molded into a single block, with the cavity hollowed out of the block, as shown in **Figure 58**. This would allow for suitable thickness to prevent significant thermal conduction and also present a large face of ceramic on the front of the receiver to act as a heat shield around the aperture.

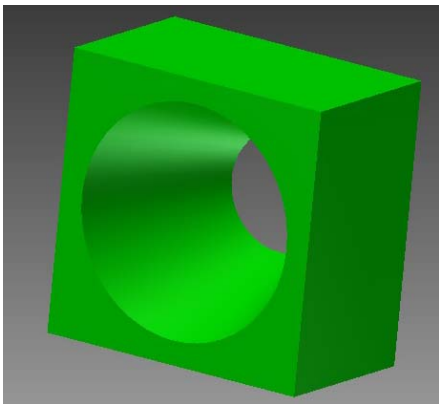

Figure 58. Ceramic Receiver Cavity (Rear View)

The thermal losses of the cavity are predicted to peak at 6.35 kW when the input from the dish peaks at 100 kW, neglecting conductive losses by assuming the cavity is well insulated and assuming that the cavity radiates as a black body at 900 °C. This value is likely conservative, because at the maximum flux of 100 kW the receiver orientation will be close to vertical which will minimize convective losses from the cavity. These values lead to a projected thermal efficiency of 93.65% for the receiver.

The back plate of the receiver (**Figure 59**) is constructed from a high temperature alloy such as Haynes 230™ that can withstand both high temperatures and intense solar flux. Heat pipes constructed of Inconel™ with sodium as the working fluid are embedded into the rear of the receiver back plate to act as the primary heat transfer mechanism. Heat also conducts directly through the back plate, but the thermal conductivity of most high temperature alloys is mediocre so the heat pipes will need to be designed such that they can carry the maximum heat input from the dish. It is estimated that approximately 22-25 1 cm inside diameter (ID) sodium heat pipes are needed to handle the heat load. The heat pipes incorporate sintered metal powder wicks in order to assist condensate return when

the receiver orientation is close to horizontal and also to increase the heat transfer coefficient in the evaporator section.

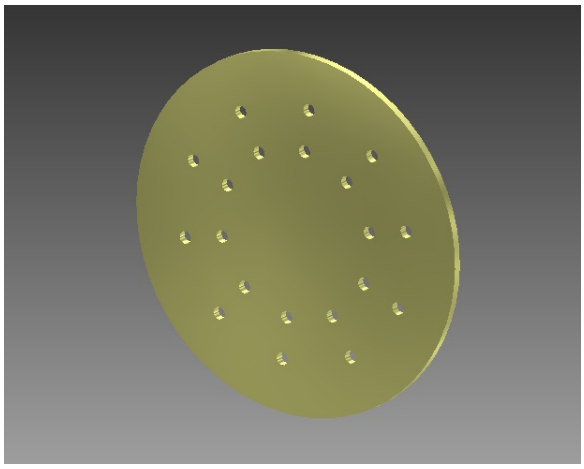

Figure 59. Receiver Back Plate with Mounts for Heat Pipes

One advantage of this design's configuration is that as solar flux increases during the middle of the day the orientation of the receiver and TES will approach vertical, meaning that as the heat transfer requirements of the heat pipes increases so will the gravity aided transport within the heat pipes. The condenser section of the heat pipes may also be designed with fins in order to ensure even heat transfer throughout the TES. The fin design will also have to accommodate movement of the molten salt within the TES due to natural convection and the freeze-thaw cycle.

The TES system uses a phase change molten NaCl/liquid sodium system to utilize the latent heat of fusion of sodium chloride and the excellent heat transfer characteristics of sodium. The molten salt absorbs the thermal energy transferred by the heat pipes, melting the salt at approximately 800°C. The liquid sodium floats on top of the molten salt as it is much lower in density and has negligible solubility in molten NaCl. The TES is under a slight vacuum at the equilibrium sodium vapor pressure at the operational temperature range of the TES (800°C). Sodium chloride undergoes a large volume increase upon melting, which causes the frozen salt to accumulate at the bottom of the TES during the freezing (energy extraction) portion of the cycle. The presence of a multitude of heat pipes within the TES helps to distribute heat evenly throughout the tank and prevent the formation of salt bridges.

The choice of TES shell materials needs to take into account several aspects of the working environment. The first requirement is the elevated temperature of 800°C or above that the shell will have to withstand. Since the tank will not be pressurized (at 800°C sodium has a vapor pressure close to atmospheric) the stresses on the tank will not be extreme, so several grades of stainless steel (such as 316L, 310 or 309) are able to provide the structural strength necessary at these temperatures. However, the corrosion of stainless steel by sodium chloride at these temperatures is not well documented, so it is

uncertain how well stainless will perform in this aspect. One option is to use a super alloy such as Inconel™ to construct the entire tank, which will provide better corrosion resistance and strength at high temperatures. This might add undue cost to the system, so an alternative is to use stainless steel and line the interior of the tank with fire bricks. This serves to insulate the tank, and also reduces the exposure of molten sodium chloride to the metal. As the molten salt moves through the cracks in the fire bricks toward the metal shell it will cool and freeze, creating a layer of solid salt around the perimeter of the tank (which will further aid in insulation due to the salt's poor thermal conductivity). Solid salt is far less corrosive that molten salt so this method may sufficiently mitigate this problem.

The heat transfer out of the TES is accomplished with a heat exchanger located at the top rear of the TES tank, as shown in **Figure 60**. This orientation keeps molten salt from coming in contact with the heat exchanger in all orientations; which must be avoided as the salt could freeze on the heat exchanger and form an insulating layer which would reduce heat transfer.

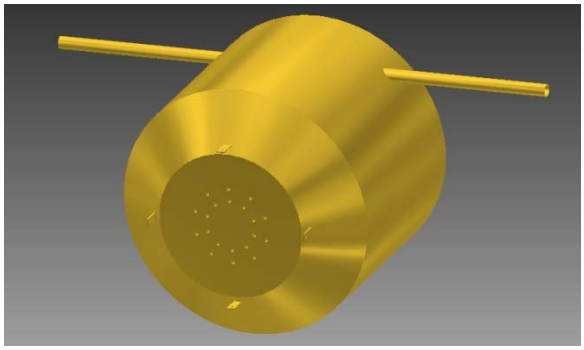

Figure 60. TES Tank with Secondary Heat Transfer Loop

The heat exchanger is a tube and fin type, single pass if possible. The liquid sodium layer floating on top of the molten salt vaporizes and then condenses on this heat exchanger, transferring its thermal energy before falling back into the liquid layer. There are many options for the working fluid of this secondary heat transfer loop such as nitrogen gas or propylene glycol, but neither water nor air should be used in close proximity with sodium due to the possibility of an explosive reaction. The purpose of this loop will be to simulate heat transfer to the chemical reactor and measure the heat transfer rate and thermal storage capacity of which the TES is capable.

The mounting of the TES and receiver to the dish arm incorporates flexible elements in order to account for vibrations arising from the high speed vapor transport within the heat pipes and for thermal expansion of the system.

3.7.3.3 Ground-Mounted TES System Configuration

The second design uses a pumped loop of liquid metal as the heat transfer mechanism to deliver thermal energy to the TES system on the ground as shown in **Figure 61**. The receiver cavity is identical to that used in the first design, except that the back plate of the receiver does not house heat pipes but is part of a flat plate heat exchanger through which the working fluid is pumped. The pumped loop system can only utilize the sensible heat of the working fluid, not the latent heat since there is no phase change involved. This leads to a fairly large flow rate in the loop when operating at the maximum flux output of the dish. Two working fluids were analyzed as possible choices for the system, sodium and lead-bismuth eutectic (LBE). Sodium has excellent thermal characteristics, high thermal conductivity (58 W/m*K) and heat capacity (1.26 kJ/kg*K) along with a fairly low density at high temperatures (SG ~ 0.75). Sodium has long been a candidate as a working fluid in fast breeder reactors so there is a good amount of data in the literature regarding its behavior at elevated temperatures. However, due to safety concerns of pumping large amounts of sodium through the system, lead bismuth eutectic was investigated as an alternative working fluid.

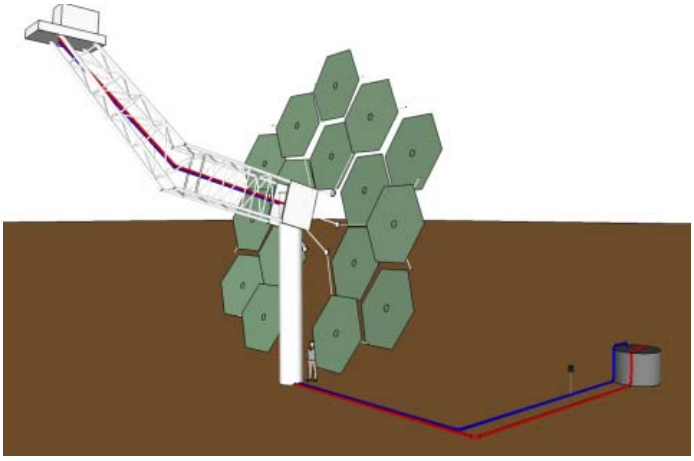

Figure 61. Dish with Pumped Loop to TES

LBE has poorer thermal conductivity (18.9 W/m*K) and heat capacity (0.15 kJ/kg*K) but due to its high density (SG ~ 10.5) the volumetric flow rate required is actually less than that for sodium, which lowers volumetric pumping requirements as long as a closed loop is employed. Even using LBE as the working fluid, the diameter of the pipe will have to be fairly large in order to keep pumping requirements reasonable. If a 2" ID pipe is used, the head losses are only 11.7', but if a 1.25" ID pipe is used the head losses jump to 186.6'. The high density of LBE causes the total pressure in the system to be significant, with a maximum value of 7.6 MPa for the 1.25" pipe and 2.15 MPa for the 2" pipe. These values give hoop stresses of 48.27 MPa and 13.42 MPa, respectively (using ANSI schedule 10 pipe). This is another reason that a large pipe diameter is necessary, as the hoop strain for the smaller pipe is excessive for stainless steel at these elevated temperatures.

Despite the pumping advantages, LBE was discarded as a candidate due to material compatibility issues. At elevated temperatures LBE erodes pipe walls due to the high solubility of many metals in liquid LBE; nickel is particularly soluble in LBE, which is unfortunate since most high temperature stainless steel grades and the super alloys contain high concentrations of nickel. Bubbling oxygen through the liquid metal flow can counter act some of this erosion by forming metal oxides which have limited solubility in LBE, but this technology is in the preliminary research phase[4]. Possible pipe materials include aluminum steel alloy and refractory metals such as tantalum or molybdenum. The aluminum steel alloy is possible because aluminum oxide is very rugged and may be capable of resisting LBE erosion, but this would require precise oxygen control and is not proven. Tantalum holds up well to the erosion, but it oxidizes into a powder when exposed to air at these temperatures and so would have to be encased in a layer of stainless steel to protect it from oxidation. Molybdenum oxide (MoO_3) forms readily at elevated temperature, and it is a gas above 500°C. Even if refractory metals prove resistant to erosion and can be formed in pipes sheathed in steel, it will be difficult to produce the flexible joints necessary to accommodate the dish's movement.

If the safety concerns about using sodium can be mitigated, then it is still a good candidate due to its excellent thermal properties. The pumping requirements are reasonable when a 2" ID pipe is used; with 32.66' of head losses (with a 1.25" pipe there are 521.74' of head losses). The maximum pressure in the system is also less due to sodium's low density and there are no material compatibility issues with stainless steel. The high thermal conductivity of sodium also makes designing heat exchangers less complicated.

There are several options for pumping the working fluid. Mechanical pumps are generally not used at this temperature range, although Wenesco Corp. claims that their pumps can operate safely up to 860°C. These pumps are designed for immersion only, so a small well would have to be designed around the pump and kept pressurized to maintain closed loop conditions. Mechanical pumps can meet the head and pressure requirements of the system and are a far less expensive option than electromagnetic (E/M) pumps.

E/M pumps are the usual choice for pumping liquid metals, but 800°C is outside of their normal operating range. The pumps can be modified to run at higher temperatures, but this adds to the cost. These types of pumps are also very inefficient (~10%) and have difficulty producing large pump heads or pressures. Another issue with these pumps is that at the elevated temperatures at which the system operates sodium begins to lose its electrical conductivity, the property on which E/M pumps operate.

Another option that was considered was to use pressurized gas, either to actuate a piston pump or to directly move the liquid. The actuated piston is capable of generating high pressures, although low flow rates mean that several pumps in parallel would likely be

[4] The authors thank Dr. Hosemann at UC Berkeley for his inputs on this topic

necessary. This configuration might be advantageous in that it will help smooth out the flow, but even with multiple pumps a surge tank would likely be necessary. The main issue with the actuated piston pump would be the seal on the piston. At these temperatures material options are limited, and even a small amount of molten sodium leaking past the seal could have serious consequences. An inert gas such as nitrogen or argon would have to be employed in the pump to avoid a sodium fire

If gas is used to directly pump the sodium, gas would inevitably bubble into the loop possibly adversely affecting both fluid flow and heat transfer in both the receiver and the TES. Perhaps of greater concern would be the entrainment of droplets of liquid sodium within the gas being vented out of the pumping chamber, allowing sodium to escape containment. With or without a piston, gas driven pumps would have low efficiencies. Some energy might be recovered from the exhaust gases by employing a closed Brayton cycle to generate electricity to reduce parasitic losses in the system.

The TES system in the pumped loop has several advantages over the on-dish storage option. Since the tank is on the ground, its size can be increased to provide as much storage as is useful for the dish's output. In addition, since the TES tank will not be moving and changing orientation with the dish, the heat exchanger design is much simpler and likely more efficient because it can be larger.

Additional measures designed to prevent salt bridging in the TES can be tested as well. An Archimedes screw as shown in **Figure 62** could be placed in the tank at the location of the salt/liquid sodium interface in order to mechanically mix the salt and prevent the formation of a crust. The length of the screw would account for the variation in salt height occurring when different fractions of salt are in the molten versus solid phase. The mixing would also promote an even heat distribution within the TES vessel. At some point the salt will freeze around the screw, causing the screw to stop, so a drive system

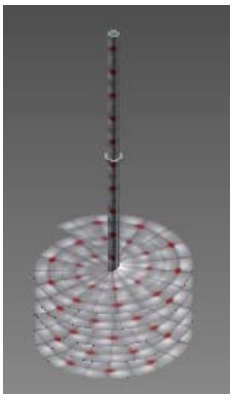

Figure 62. Archimedes Screw for TES Mixing

capable of withstanding this condition would have to be employed. One weak point of this design would be the seal around the shaft where it exits the TES vessel, and for this reason the screw may not be a viable option.

An alternative method of mechanical agitation would be to induce vibrations in the walls of the vessel, to disrupt the liquid interface and the interface at the wall of the vessel, the two starting points of crusting. Care would need to be taken that the vibrations are not too strong, so as to disrupt the floating sodium layer or the structure of the tank itself.

Heat pipes or thermosiphons can also be employed to prevent crusting by ensuring even heat distribution throughout the TES vessel. However, this solution is not straight forward because of the heat distribution characteristics of the molten salt. In order to prevent crusting heat needs to be delivered to the salt/sodium interface, but the location of the interface varies with the freeze-thaw cycle. Additionally, if the TES is functioning properly the frozen salt will sink to the bottom of the vessel, meaning that this will be the coldest location in the tank. So heat would have to be transferred from the middle of the tank instead of the bottom, but at some point the middle of the tank will also freeze, at which point the heat transfer to the salt/sodium interface will stop, leading to possible crusting.

An alternative design would use heat pipes as the primary heat transfer mechanism, instead of a liquid sodium pool boiler. Molten salt could still be used as the thermal storage medium, but heat pipes would extend all the way to the top of the vessel and connect with the heat exchanger directly.

Another option would be to have a funnel to catch the sodium condensate as it falls off of the heat exchanger fins and deliver it to near the bottom of the molten salt, where it would bubble to the surface thereby disrupting crust formation. The funnel would have to be designed such that the pressure head of sodium would be enough to overcome the NaCl liquid pressure throughout the freeze-thaw cycle.

3.7.3.4 Bench-Scale Phase-Change Storage Test

A bench scale demonstration of the TES system was constructed and tested at SAIC's Rancho Bernardo, California laboratories as shown in **Figure 63**.

The purposes of the demonstration were to achieve heat transfer both into and out of the TES vessel, demonstrating storage of thermal energy, and also to observe the formation of crusting in the vessel and to test countermeasures against the crusting. Paraffin wax and denatured alcohol were used as proxies for the molten salt and liquid sodium because the wax undergoes a large volume change upon melting and the melting point of the wax is close to the boiling point of the alcohol at atmospheric pressure. Additionally, the alcohol will float on top of the wax due to its lower density (S.G. 0.7 compared to S.G. 0.8) and the wax's insolubility in alcohol.

Figure 63. Setup for Bench Scale TES Demonstration

The test vessel was constructed of a 5" outside diameter (OD) polycarbonate tube, capped at both ends by machined aluminum blocks. The vessel was sealed at the bottom with high temperature silicone sealant, and at the top a rubber sheet was cut to fit and adhered to the aluminum with high temperature silicone. The vessel was to be held under a mild vacuum, so a hole was drilled into the tube wall and a copper sweat fitting was used to create a smooth fit with the tube wall. This fitting was sealed with two-part epoxy resin where it met the wall. The other end was soldered to a brass barb attached to a ½" hose. The hose attached to a tee fitting, equipped with two separate shut off valves; one of which was used to isolate the vacuum pump from the test chamber once vacuum was achieved, and the other was used to introduce a charge of alcohol without breaking the vacuum seal.

The heat source for the experiment was a 750W hot plate, adjusted to stay under the 130°C working temperature of the polycarbonate. Temperatures were monitored with a temperature logger equipped with a type K thermocouple. Heat transfer out of the top plate was measured by placing a 1000 mL flask of water on top of the vessel in good thermal contact with the top aluminum plate, and observing the temperature rise of the water. In one case maximum heat transfer was encouraged by using a 20 kg lead block that was stored in a freezer before placing it on top of the test vessel.

The procedure was to first prepare the test vessel by melting the wax and then letting it freeze, in order to achieve a uniform block of wax. A charge of alcohol was then added after the test chamber was evacuated with the vacuum pump. A crust was observed during the freezing portion of every thaw/freeze cycle, as shown in **Figure 64**. Once formed, the crust halts effective heat transfer, leaving a large percentage of the thermal energy untapped. With no countermeasures employed the crust began to form around the top edge of the wax layer roughly 25 minutes after heat addition was stopped, and the crust completely covered the surface within one minute.

Figure 64. TES Crust Formation in Test Vessel

Three copper/water heat pipes measuring 5 mm ID and 120 mm in length were soldered to a copper plate and placed in the test vessel in order to assist in heat transfer and prevent crust formation.

In the course of tests, the seal on the copper sweat fitting had to be repaired, as it was discovered that the alcohol vapor dissolved away the epoxy resin after only five hours of exposure, allowing a large portion of the alcohol to escape and contaminating the test vessel with dissolved resin. The fitting was resealed using high temperature silicone sealant and the alcohol was replaced in the test vessel.

The heat pipes appeared to help somewhat in the melting phase, transferring heat up away from the bottom plate and melting wax along their lengths, thereby creating an escape route for wax melting at the bottom of the vessel. During the freezing phase the heat pipes delayed but did not prevent crust formation (see **Figure 65**).

Figure 65. Crust Formation Around Heat Pipes

With the heat pipes in place, it took up to 20 minutes for a complete crust to form after the initial formation of a frozen ring of wax. This represented a significant improvement from less than one minute for complete crust formation without the heat pipes. Initially the copper plate to which the heat pipes were soldered was a solid round sheet, but it was found that the plate inhibited natural convection of the wax. The plate trapped a small layer of wax at the bottom plate where it became overheated and boiled, which was not desirable for the experiment. The plate was removed and a number of holes were drilled in it to remedy this problem. The heat pipes were placed back into the test vessel and it was observed that there was significantly less wax boiling.

The other countermeasure proposed for testing was a magnetic stirrer, used to simulate the mechanical agitation of an Archimedes screw. Unfortunately, the stirrer proved not to be powerful enough to agitate the contents of the test vessel, and so the method of mechanical stirring could not be tested as a crusting counter measure. Another issue in the test was the fairly large difference between the melting point of the wax (~ 60°C) and the boiling point of the alcohol (78.1°C, at atmospheric pressure). This meant that a large amount of heat addition was required even after all the wax was melted in order to boil the alcohol. A major cause of this issue was the failure of the test vessel to hold a vacuum for a long period of time. The leak due to the epoxy resin failure was found and repaired, but the port never sealed properly again after the initial failure. If the vessel was under a mild vacuum as planned the boiling point of the alcohol would have been lowered close to the melting point of the wax. This is another area where the heat pipes were useful; since the tops of the heat pipes protruded into the alcohol layer the heat pipes were able to transfer heat directly to the alcohol, bypassing the wax. It was documented that local alcohol boiling was occurring directly at the top of the heat pipes before all of the wax was melted. This would be advantageous in the actual system; in the case of a cold start heat transfer out of the TES could begin sooner with the addition of heat pipes in the vessel.

Overall, the bench scale demonstration achieved its objectives. The paraffin wax and denatured alcohol acted fairly well as proxies for the molten salt and liquid sodium, with the alcohol layer floating on top of the melted wax and the wax crusting similarly to the molten salt. Heat transfer by the alcohol was achieved, with stable boiling of the alcohol at the liquid wax/alcohol interface and alcohol vapor condensing on the top plate of the test vessel. No meaningful heat transfer values could be extracted because of the poorly insulated walls of the vessel and because of the intermittent heating of the hot plate, but it was confirmed that heat transfer was occurring by measuring the temperature change of both water and lead. Crust formation at the top of the wax layer was observed during every freezing phase and it was determined that although heat pipes assist in heat transfer, they only delayed and did not prevent the formation of a crust. When the bottom plate was kept insulated after removal from the hot plate (by placing the vessel on a wooden block) the wax froze at the wax/alcohol interface, forming a crust before freezing anywhere else in the vessel. This is contrary to what the large density difference between the solid and liquid wax indicates should happen, but is in agreement with experiments done on the molten salt/ liquid sodium TES.

3.7.3.5 TES On-Sun Test Conclusions

At this stage of the project the heat pipe receiver with storage on the dish seems the more feasible approach for an on-sun test than does the separated TES system, but this design will not scale easily to a larger system. The only remaining issues with this design are material decisions, detailed heat pipe design and cost. The pumped loop design better approximates commercial scale applications of this technology, but this design would have more issues to overcome to enable an on-sun test. Since LBE appears to be incompatible with known piping materials, it is not practical to consider LBE as a working fluid. Sodium as the working fluid does not suffer from the material compatibility issues, but safety is a major concern. Sodium reacts vigorously with water at all temperatures and at 800°C, auto-ignites in air. If these hazards can be reduced to acceptable levels, there are still hurdles to overcome in this system; the largest of which is pumping. The pumping requirements are higher for sodium than for LBE, although total system pressure is less, and the operating temperature of the system is problematic for pumps of all types. Another issue with the pumped loop is the amount of liquid metal required. If a 2" ID pipe is used 96.5 kg of sodium metal would be necessary, assuming the heat exchangers are not too large or complex.

The thermal storage system was shown to have the expected crusting issues during the bench scale demonstration. From the results of the test, it is recommended to include a number of heat pipes in the TES design to facilitate heat transfer and delay crusting. Mechanical stirring was not able to be tested, but would likely prevent crusting.

3.7.4 Solar System Heat Transfer Configuration

Figure 66 shows a schematic of the proposed configuration of the solar heat transfer system for the SA system. It is necessary to collect the heat at the receiver, transfer it to the phase change storage tank, and then transfer the heat from the storage to the SA chemical process plant.

Because of the high temperature operation of the system (800°C), the heliostat field is configured as a North-field arrangement. In order to deliver a nominal 50MW_{th} to the chemical plant, the heliostat field includes 231,600 m^2 of heliostat mirrors, and a 150m tower height. Using the NREL Solar Advisor Model (SAM), performance of the system in Barstow, CA is estimated as follows:

- 150 MW_{th} peak power to receiver
- 1196 MWh_{th} peak daily energy delivery (=50 MW spread over 24 hours)
- 32.3 MW_{th} average power over the year
- 44% solar-to-thermal efficiency

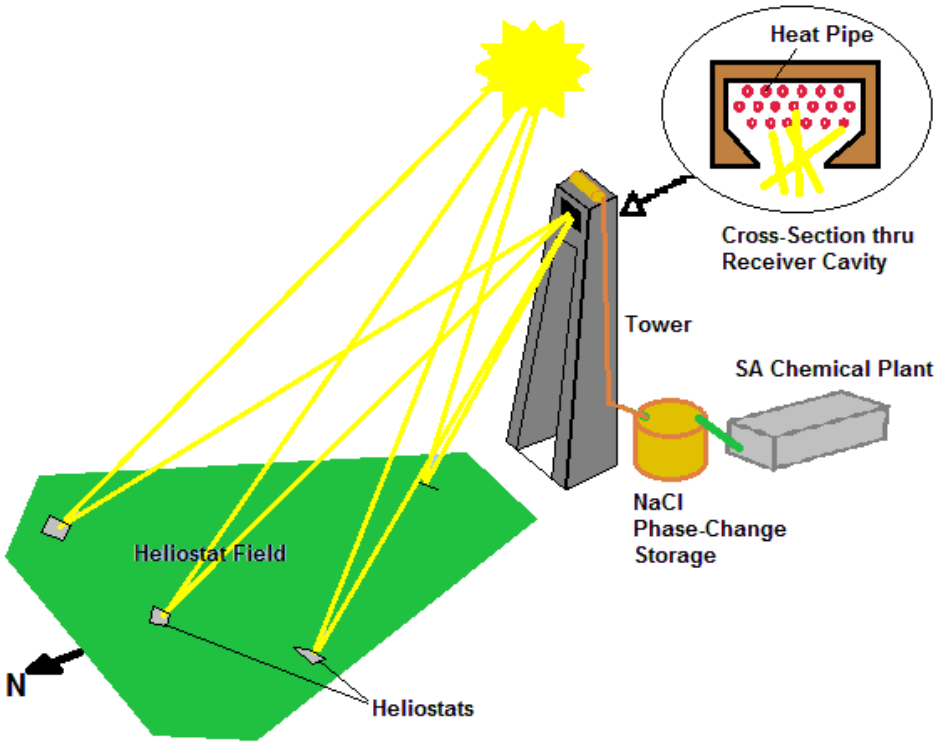

Figure 66. Proposed Solar System Heat Collection and Transfer Configuration

3.7.4.1 Receiver Configuration

Due to the high receiver temperature, a cavity receiver is proposed. Inside the cavity, vertical sodium heat pipes are arrayed in a grid arrangement, with their condensers terminating in a "steam drum" tank above the receiver. This arrangement allows the heat pipes to use gravity assist in returning the condensed sodium to the evaporators. Also, placing the sodium in multiple independent heat pipes segregates the material so that a single failure results in the release of only a small amount of sodium. The receiver would be designed with excess heat pipes, so that if one or more failed the ones around them could "take up the slack" and deliver the power to the steam drum with minimal difficulty.

3.7.4.2 Heat Transfer to/from NaCl TES

Between the TES tank on the ground and the steam drum on the tower, a pumped liquid loop system would be used. The working fluid is proposed to be sodium. This minimizes compatibility issues at the steam drum and interfaces easily to the TES tank. Using an all-liquid system, pumping losses will be limited to the fluid resistance of the flow. Finally, segregating the sodium from the receiver and the transfer loop minimizes the volume of sodium that could leak.

Between the TES and the chemical plant, the floating sodium "heat pipe" approach will be used, as described in Section 3.7.3. Either the molten salts can be pumped through pipes in the head space of the TES tank, or the mid-temperature reactor could be integrated into the top of the tank so that it could have a direct connection to the sodium vapor in the TES tank head space.

3.8 Hydrogen Production Economic Evaluation

3.8.1 Preliminary Economic Comparison to Hybrid Sulfur Process

At the beginning of the project, a comparison was made between the SA cycle and the hybrid sulfur (HyS) process that has been studied by Sandia Labs. In the Sandia analysis, a large central hydrogen production plant was designed, costs were estimated for the components of the solar and chemical plant, and the cost of hydrogen from the plant was projected.

To compare with the HyS process, adjustments were made to the plant configuration as follows:

- Estimated SA process efficiency vs. HyS process efficiency.
- Estimated solar field efficiency for 850°C receiver vs. 1100°C receiver.
- Estimated cost of plastic film solar photoreactors.
- Estimated present costs and performance characteristics of hot and cold mirrors.
- Estimated costs of GRC and conventional heliostats.

The results of this preliminary evaluation are summarized in the following table:

Table 10. Preliminary Economic Analysis of SA Process (Photocatalytic)

	Area of Solar Reflectors [sq. km]	Total Land area [sq. km]	Total Capital Cost [$M]	Projected Cost of H_2 [$/kg]
Baseline hybrid sulfur heliostat (Kolb)	1.30	6.50	381.2	$3.00
SA heliostat w/hot mirror	1.06	5.31	810.6	$4.12
SA heliostat-separate photoreactor	0.84	5.90	435.1	$2.33
SA advanced heliostat with separate photoreactor	0.84	5.90	417.4	$2.25

The photocatalytic SA process showed the potential to reduce the size of the heliostat field from 1.3 sq. km to 0.84 sq. km, and to reduce the land area (even with a separate photoreactor system) from 6.5 sq. km to 5.9 sq. km or less. These improvements were mainly due to the high efficiency of the SA process and the reduction in the temperature of the hot reactor, leading to higher solar receiver efficiency. The hot-mirror system showed slightly worse economics than the baseline system, mainly due to the estimated cost of the hot mirrors, but the systems with separate photoreactors showed significant reductions in the cost of hydrogen produced. Use of an advanced (GRC) heliostat

produced even larger savings. These results were encouraging regarding the potential for the SA cycle to deliver hydrogen cost-effectively.

3.8.2 Economic Optimization of Electrolytic Process

After the decision was made to change to the electrolytic SA process, an optimization analysis was performed using preliminary electrolysis data. The costs for the electrolytic process include the capital costs of the equipment and operating costs for electricity to drive the reaction. These cost components are related to the performance of the electrolytic cell components, in particular the overpotential vs. current density in the membrane. The overpotential is a monotonically increasing value with current density, and the cost of the system is proportional to the area of membrane, hence it varies inversely with the current density at which the membrane is operated for equal production of hydrogen.

An attempt was made in May 2011 to quantify the costs of the membrane and the cost of electricity for operation of the electrolytic cell. Then, the measured Voltage-current density curve was used to calculate the capital and operational costs as a function of the current density in the membrane. Finally, the capital costs were multiplied by a capital recovery factor to annualize them. The results of the study are shown in **Figure 67**.

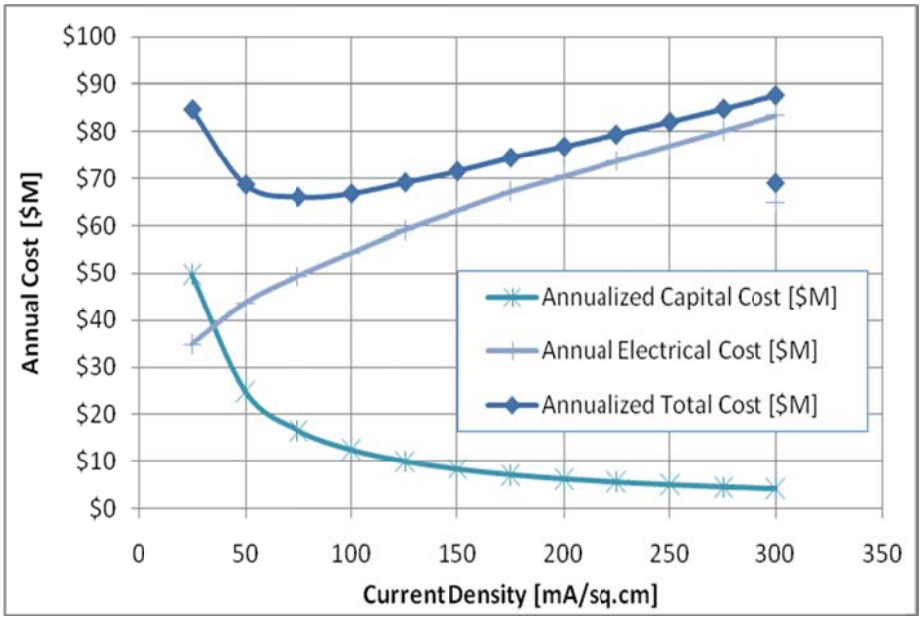

Figure 67. Results of Economic Optimization of Electrolysis Process

In the figure, the capital cost decreases with increasing current density because less area of membrane is needed. The electrical cost increases with current density due to increasing overpotential and therefore less efficient operation of the electrolytic cell. The sum of the two components is shown at the top of the graph, and has a minimum at a current density of about 75mA/cm^2. This value is a relatively low current density for

electrolysis systems, indicating that the cost of electricity (driven by the overpotential) is the larger driving force in the total cost. Therefore, efforts directed towards decreasing the overpotential could result in substantial cost decreases for the overall system.

3.8.3 Economic Analysis Updates

Over the course of the project the economic analysis of the SA system was updated several times using the DOE H2A cost analysis system. Over time, improved data became available on the performance of the electrolysis process and more definition was achieved on the equipment costs and chemical system performance using the Aspen Plus modeling. Also, the H2A analysis itself was updated during the course of the project, and data needed to be transferred each time to the new versions. A summary of the results of the H2A analyses over time is presented in the following table, and the paragraphs that follow present the details of each of the analyses. The data presented are all for the short-timeframe (2015) cost estimates.

Table 11. H2A Economic Analysis Results Over Time for the SA Process

Date of Estimate	**Estimated Hydrogen Production Cost [$/kg]**	Capital Cost	Decom-missioning Cost	O&M	Feedstocks	Raw Mat'ls	Byproducts	Other Variable Costs
10/8/2008	**$5.64**	$4.34	$0.01	$1.31	$0.00	$0.00	-$0.04	$0.01
11/27/11	**$7.74**	$6.70	$0.01	$1.03	$0.00	$0.00	$0.00	$0.00
8/16/12	**$11.74**	$9.53	$0.01	$2.17	$0.00	$0.01	$0.00	$0.02
3/15/13	**$11.89**	$9.77	$0.01	$2.07	$0.00	$0.01	$0.00	$0.03
8/27/13	**$10.91**	$8.96	$ 0.01	$1.90	$0.00	$0.01	$0.00	$0.03

3.8.3.1 October 2008

This version incorporated the first complete Aspen Plus cycle analysis and experimental data on the performance of the photocatalytic process. The photoreactors were configured as a separate field of Kynar™ flat-plate collectors, extending over an area of 9.6 km^2. The thermal part of the system was configured as a standard central receiver power plant with three million square meters of heliostats. The total capital cost of the solar collection system came to $635 million and the cost for the chemical plant equipment came to $380 million, for a total capital cost of $1.015 billion.

3.8.3.2 November 2011

In this version, the photocatalytic process had been replaced by electrolysis. The solar field continued to be a heliostat/central receiver configuration, but storage had been added to allow longer operation of the chemical plant each day. In this system, five central receiver plants were required to meet the DOE requirement of 100,000 kg/day average hydrogen production. For this particular design, the heliostat area totaled 3.9 million square meters and the solar system capital cost was $888 million. The

electrolysis system cost was $65 million, and the balance of the chemical plant was about $147 million. The total capital cost was $1.101 billion.

3.8.3.3 August 2012

This version was based on the 50MW_{th} modular solar/chemical plant design. The heliostat field for each module was 231,600 m^2, with a 150 m tower. The system also included a high-temperature phase-change storage system to enable continuous operation of the chemical plant with a 65% annual capacity factor. The chemical plant equipment costs were based on a more detailed enumeration and evaluation of the components, including heat recovery heat exchangers and power generation equipment. The capital costs for the solar collection system were about $40 million, for the storage system about $25 million, and for the chemical plant and electrolysis system about $13.4 million, for a total capital cost of $78.2 million for each module. Each modular solar/chemical plant was estimated to produce 5,700 kg/day of hydrogen, so for 100,000 kg/day 18 modules would be needed. This gave a total capital cost of $1.4 billion.

3.8.3.4 March 2013

This version included the same solar and chemical plant configuration as the previous one, with updated costs and performance information. The capital costs were estimated at $40 million for the solar collection system, $14.7 million for the solar storage, and $16.9 million for the chemical and electrolysis plant equipment, for a total of $71.4 million. Again, multiple modules would be needed to meet the DOE 100,000 kg/day requirement, for an estimated total capital cost of $1.428 billion.

3.8.3.5 Latest Estimate: August 2013

As further evaluation was performed, costs and performance data was updated. In this final update, the solar field efficiency was increased by changes in the operational parameters in the NREL SAM calculation that was used to estimate solar performance. The heliostat array was adjusted to 227,620 m^2, and the output per module was increased to 5,397 kg/day, so only 19 modular systems would be needed for 100,000 kg/day. Overall, the solar field cost dropped to $38.7 million, the storage system was estimated at $14.7 million, and the chemical and electrolysis systems were estimated at $16.9 million, for a total capital cost of $70.2 million per modular system. For the total DOE requirement of 100,000 kg/day, the capital cost was estimated at $1.33 billion. Thus, in contrast to earlier updates, the process and solar system performance improvements resulted in a lower estimated cost of hydrogen.

3.8.4 2025 H2A Cost Estimates

For the out-year (2025) cost estimates, projections were made as to potential and expected improvements to the process, chemical plant and electrolytic components, and the solar collection system. The cost of heliostats was assumed to drop from $126/$m^2$ to $75/$m^2$, which led to significant reductions in the solar plant cost because of their high impact on the system cost. Due to expected improvements in the membranes and catalysts used for electrolysis, the voltage needed for electrolysis was estimated to drop from 1.1V to 0.4V, and the current density was estimated to increase from 100 mA/cm^2 to 500 mA/cm^2.

When these projections were applied to the August 2013 cost estimate, the solar plant costs decreased to $24 million, with $10.3 million for the storage system. The chemical plant and electrolysis equipment costs dropped to $8.5 million, for a total capital cost of $42.8 million (down 39% from $70.2 million in the near-term estimate). With the projected increases in performance included, the estimated hydrogen cost from the SA cycle was $7.04/kg (down 35% from the $10.91/kg estimated in the near-term).

4 Conclusions

The SAIC team has made significant progress toward developing a cost-effective and efficient hydrogen production technology based on a solar thermochemical water-splitting cycle. A sulfur family cycle having ammonia as the working fluid and reagent has been developed. The sulfur ammonia (SA) cycle is a renewable and sustainable process that is unique in that it is an all-fluid cycle (i.e., with no solids handling). It uses a moderate temperature solar plant with the solar receiver operating at 800°C. All electricity needed is generated internally from recovered heat. While the SA cycle appears to be complex it consists of only three chemical reactions plus absorbers, scrubbers and heat exchangers. The plant would operate continuously with low cost storage and it is a good potential solar thermochemical hydrogen production cycle for reaching the DOE cost goals.

The long term stability of the complete electrochemical system has been demonstrated with a 500+ hour extended run. New membranes have been identified with up to two orders of magnitude lower sulfite fluxes (vs. the Nafion 112 membrane initially used) even after treatment at 140°C. Activities in this project have resulted in achieving a 43% reduction in cell voltage through a combination of electrocatalyst, membrane and cell development improvements.

The high-temperature oxygen generation step is an all fluid process requiring no solid particle handling. Lab results prove the sub-cycle feasibility. The NH_3 and SO_3 were demonstrated to evolve separately, so they can be separated thermally without complicated membrane separation. A lower salt melting temperature was achieved and it was demonstrated that the molten salts in the process have low enough viscosities to be pumped. The decomposition of SO_3 is proven technology. The entire process consists of elementary chemical engineering unit operations that have been in widespread industrial use for over 100 years.

The Aspen Plus® modeling was used to significantly optimize the SA process. Due to the variability of solar energy, a phase-change thermal-storage system with NaCl was incorporated, allowing continuous plant operation at 790°C. Rankine power cycles were designed to recover excess heat to efficiently generate electricity. Overall plant pressure was varied to optimize plant efficiency and power recovery. The solar configuration evolved to a 50 MW(thermal) central receiver system with a North heliostat field, a cavity receiver, and NaCl molten salt storage to allow continuous operation. The H2A economic model was used to optimize and trade-off SA cycle configurations. Parametric studies of chemical plant performance have indicated process efficiencies of ~20% [6] and identified areas for further research and study for future improvements to the cycle. All of the processes in the SA cycle have now been proven in the laboratory or have been fully demonstrated by others, but further optimization is still possible and needed.

5 Proposed Future Activities

The Sulfur-Ammonia thermochemical hydrogen process remains one of the most viable means for producing hydrogen using solar energy. Process improvements made in the course of this project have led to a design for a complete hydrogen plant that operates "around the clock" from stored solar heat. Although the current process efficiency is technically acceptable, an increased efficiency is needed if the DOE cost targets are to be reached. The amount of efficiency improvement is difficult to specify because it is dependent on many other factors. There are two interrelated areas in which there is the potential for significant efficiency improvements: electrolysis cell voltage and excessive water vaporization. Currently the Sulfur-Ammonia process requires the evaporation of large quantities of water. Methods to significantly reduce water evaporation are proposed for future activities. One of the process variations for future work is to make the system less basic (neutral pH), using ammonium bisulfite and ammonium bisulfate which have higher solubility, thus allowing a decrease in the amount of water which must be evaporated. It is possible to both decrease the cell voltage and decrease the amount of water that must be evaporated in the process.

Electrolysis membranes that permit higher temperatures and lower voltages need to be sought. But the major emphasis needs to be the reduction of the amount of water vaporized. The electrolyzer product could be cooled such that ammonium sulfate is crystallized out and sent to the low temperature reactor as a minimally-hydrated slurry. Reduction of the amount of water evaporated will result in improved process efficiency. A more radical departure from the current technology would be to replace the aqueous electrolyte with a low melting-temperature salt such as ammonium bisulfate/bisulfite. The salt would contain only enough water to provide melt stability and water (as steam) would be fed to the cathode as a source for hydrogen. The cell should operate optimally at about 200°C with a significantly reduced overvoltage. Ideally, this cell would have molten potassium hydroxide in the cathode compartment and a hydroxide transport membrane.

The oxygen half cycle also needs further development and improvement. The low temperature reactor could be operated in a semi-continuous mode. A small stream of electrolyzer product would be fed to a large reservoir containing molten sodium/potassium sulfate/pyrosulfate molten salt. Making runs at different reservoir temperatures, electrolyte flowrates and electrolyte compositions would permit full elucidation of the reaction kinetics.

6 Products and Technology Transfer Activities

6.1 Publications and Presentations

1. Ryan Tanakit, Wesley Luc, J. Talbot, "Electrophoretic Deposition of Cobalt Ferrite and Platinum Cobalt Nanoparticles as Electrocatalysts," Abstract 2306, for presentation at the 224th ECS Meeting in San Francisco, California (October 27-November 1, 2013).
2. Irina Rumyantseva, Nicole Shellhammer, Neil Verma, "Solar Hydrogen Production: Sulfur-Ammonia Cycle," Leidos and UCSD Team Internship Program (TIP) Summit, Leidos, San Diego, Oct. 1, 2013.
3. Kevin Fructuoso, Luke Batcher, "Solar Hydrogen Production: Salt Energy Storage," Leidos and UCSD Team Internship Program (TIP) Summit, Leidos, San Diego, Oct. 1, 2013.
4. Davenport R., Taylor R., Genders D., Symons P., Herz R., Talbot J., Brown L., Luc W., "Status of the Solar Sulfur Ammonia Thermochemical Hydrogen Production System for Splitting Water", Technical Paper and Presentation for the SolarPACES 2013 Conference, Las Vegas Nevada, September 17, 2013.
5. Luc, W., "A Continuous Solar Thermochemical Hydrogen Production Plant Design," M.S. thesis, University of California, San Diego, 2013.
6. Brown, L., Symons, P., Taylor, R., Presentation at the 2013 U.S. DOE Hydrogen and Fuel Cell Program and Vehicle Technologies Program Annual Merit Review and Peer Evaluation Meeting, Washington D.C., May 16, 2013. (PowerPoint presentation).
7. Wesley W. Luc, Richard K. Herz and Jan B. Talbot, "Design of a Solar Thermochemical Hydrogen Production Plant", Poster presented at the UCSD Jacobs School of Engineering Research Expo, April 18, 2013.
8. Jesse Littlefield, Mimi Wang, Lloyd C. Brown, Richard K. Herz and Jan B. Talbot, "Process Modeling and Thermochemical Experimental Analysis of a Solar Sulfur Ammonia Hydrogen Production Cycle," World Hydrogen Energy Conference 2012, *Energy Procedia* 29 (2012) 616 – 623
9. J. Littlefield, Solar Thermochemical Hydrogen Production Plant Design," M.S. thesis, (2012). Thesis defense on Nov. 19, 2012.
10. Tanakit, R., Luc, W., Solar Hydrogen Project, Poster presentation at the UCSD Jacobs School of Engineering Corporate Affiliates Program, La Jolla, California, September 27, 2012.
11. Tanakit, R., Luc, W., Solar Hydrogen Project, Presentation at the SAIC/UCSD Jacobs School of Engineering Intern Summit, San Diego, California, September 14, 2012. (PowerPoint presentation).
12. Taylor, R., Genders, D., Brown, L., Talbot, J., Herz, R., Davenport, R., Presentation at the DOE Sulfur Ammonia Cycle Phase 1 Go/No-Go Meeting Teleconference, August 27, 2012. (PowerPoint presentation).
13. Taylor, R., Genders, D., Brown, L., Talbot, J., Herz, R., Davenport, R., Presentation at the STCH Hydrogen Production Technology Team Review Meeting, La Jolla**,** California, July 10, 2012. (PowerPoint presentation).

14. Wang, M, "Study of the Thermochemistry for Oxygen Production for a Solar Sulfur-Ammonia Water-Splitting Process," MS thesis, University of California, San Diego (2012).

15. Taylor, R., Davenport, R., Talbot, J., Genders, D., Brown, L., Herz, R., Overview and Status of the Sulfur Ammonia Thermochemical Hydrogen Production System for Splitting Water, Presentation at the 19th World Hydrogen Energy Conference 2012, Toronto, Ontario, Canada, June 3-7, 2012.

16. Taylor, R., Davenport, R, Solar Field Design and Integration for Thermochemical Hydrogen Production Systems, Poster presentation at the 19th World Hydrogen Energy Conference 2012, Toronto, Ontario, Canada, June 3-7, 2012.

17. Littlefield, J., Wang, M., Adoum, M., Talbot, J., Herz, R., Brown, L., Process Modeling and Thermochemical Experimental Analysis of the Solar Sulfur Ammonia Hydrogen Production Cycle, Presentation at the 19th World Hydrogen Energy Conference 2012, Toronto, Ontario, Canada, June 3-7, 2012.

18. Littlefield, J., Wang, M., Talbot, J., Herz, R., Brown, L., Process Modeling and Thermochemical Experimental Analysis of the Solar Sulfur Ammonia Hydrogen Production Cycle, submitted to *Energy Procedia* (2012).

19. Wang, M., Talbot, J., Herz, R., Brown, L., "Melting Point and Viscosity of Molten K_2SO_4 + $K_2S_2O_7$ + Na_2SO_4 + $Na_2S_2O_7$ Mixtures", submitted to *Journal of Chemical and Engineering Data* (2012).

20. Genders, D., Symons, P., Brown, L., Electrochemical Oxidation of Ammonium Sulfite for the Sulfur Ammonia Thermochemical Hydrogen Production System, Poster presentation at the 19th World Hydrogen Energy Conference 2012, Toronto, Ontario, Canada, June 3-7, 2012.

21. Davenport, R., Taylor, R., Genders, D., Brown, L., Talbot, J., Presentation at the 2012 U.S. DOE Hydrogen and Fuel Cell Program and Vehicle Technologies Program Annual Merit Review and Peer Evaluation Meeting, Washington D.C., May 14-18, 2012. (PowerPoint presentation).

22. Littlefield, J., Herz, R., Brown, L., Solar Thermochemical Hydrogen Production Plant Design, Technical poster presented at the University of California, San Diego Jacobs School of Engineering Research Expo, La Jolla, California, April 12, 2012.

23. Taylor, R., Davenport, R., Woodard, K., Production of Hydrogen from Solar Energy, Technical paper and presentation at the 2011 World Energy Engineering Congress, Chicago, Illinois, October 13, 2011.

24. Luc, W., Woodard, K., Presentation at the SAIC and UCSD Team Internship Program (TIP) Presentations, Scaled Hydrogen Reactor Design and Electrode Catalyst Electrophoretic Deposition, Jacobs School of Engineering, UCSD, La Jolla, California, September 28, 2011. (PowerPoint presentation).

25. Taylor, R., Genders, D., Brown, L., Presentation at the STCH Technical Progress Meeting, Livermore, California, July 13, 2011. (PowerPoint presentation).

26. Davenport, R., Taylor, R., Genders, D., Brown, L., Talbot, J., Presentation at the 2011 U.S. DOE Hydrogen and Fuel Cell Program and Vehicle Technologies Program Annual Merit

Review and Peer Evaluation Meeting, Washington D.C., May 9-13, 2011. (PowerPoint presentation).

27. Wang, M., Ramzi, S., Talbot J., Thermogravimetric Study of a Solar Sulfur-Ammonia Thermochemical Water Splitting Cycle, Poster Presentation at the Jacobs School of Engineering Research Expo, University of California, San Diego, April 14, 2011.
28. Taylor, R., Genders, D., Davenport, R., Brown, L., Presentations at the STCH Technical Progress Meeting, University of Colorado, Boulder, October 27, 2010 (PowerPoint presentations).
29. Davenport, R., Taylor, R., T-Raissi, A., Genders, D., Muradov, N., Presentation at the DOE Annual Merit Review and Peer Evaluation Meeting – DOE Hydrogen Program and Vehicle Technologies Program, Washington D.C., June 8-11, 2010. (PowerPoint presentation).
30. Huang, C., T-Raissi, A., Choi, P., Muradov, N.Z. "Hydrogen Production via Electrolysis of Aqueous Ammonium Sulfite Solution," paper presented at the 18th World Hydrogen Energy Conference, Essen, Germany, May 16-21, 2010.
31. Taylor, R., T-Raissi, A., Fenton S., Davenport, R., Symons, P. Presentation at the STCH Technical Progress Meeting, Florida Solar Energy Center, Cocoa, FL, March 23-24, 2010. (PowerPoint presentation).
32. T-Raissi, A. "Thermochemical Water-Splitting Cycles for Hydrogen Production," Chapter in Energy Production and Storage – Inorganic Chemical Strategies for a Warming World, Encyclopedia of Inorganic Chemistry, R.H. Crabtree, Editor. *John Wiley & Sons Ltd*., 2010, in press.
33. Taylor, R., T-Raissi, A., Fenton S., Davenport, R., Genders, D. Presentation at Phase 1 Go/No-Go Meeting, DOE Golden Field Office, December 3, 2009 (PowerPoint presentation and Meeting Summary).
34. Taylor, R., Davenport, R., T-Raissi, A., Muradov, N., Huang, C., Fenton, S. "Solar Thermochemical Hydrogen Production via a Sulfur-Ammonia Cycle," *SolarPACES 2009 Conference*, Berlin, Germany, September, 2009.
35. Davenport, R., Taylor, R. "Low Cost Glass-Reinforced Concrete Heliostats," *SolarPACES 2009 Conference*, Berlin, Germany, September, 2009.
36. Yao, W., Huang, C., Muradov, N.Z., T-Raissi, A. "Photocatalytic H2 Evolution on Visible Light Illuminated CdS Supported Pd-Cr2O3 Nanocomposite Cocatalyst Using Re-generable Sacrificial Donor," Submitted for publication in *JACS*.
37. Huang, C., Linkous, C.A., Adebiyi, O., T-Raissi, A. "Hydrogen Production via Photolytic Oxidation of Aqueous Sodium Sulfite Solutions," to appear in the *J. Environmental Science & Technology*.
38. Mao, L., T-Raissi, A., Huang, C., Muradov, N.Z. "Thermal Decomposition of (NH4) 2SO4 in the Presence of Mn3O4," to appear in the *Int. J. Hydrogen Energy*.
39. Yao, W., Huang, C., Muradov, N.Z., T-Raissi, A. "Photocatalytic H_2 Evolution on Visible Light Illuminated CdS Supported Pd-Cr_2O_3 Nanocomposite Cocatalyst Using Regenerable Sacrificial Donor," Paper submitted to the *J. of the American Chemical Society*.

40. Yao, W., Huang, C., Muradov, N.Z., T-Raissi, A. "Photocatalytic H_2 Evolution on Visible Light Illuminated CdS Supported Pd-Cr_2O_3 Nanocomposite Cocatalyst Using Regenerable Sacrificial Donor," Paper submitted to the *J. of the American Chemical Society*.

41. Taylor, R. T-Raissi, A. Davenport, R. "Solar Hydrogen Production Through High-Efficiency Thermochemical Water Splitting with Photocatalytic or Electrolytic Steps," *SOLAR 2009* (ASES National Solar Conference), Buffalo, NY, 11-16 May **2009**.

42. Taylor, R., Davenport, R., T-Raissi, A., Muradov N., Huang C., Fenton S., Block D. "Solar Hydrogen Production Through Thermochemical Water Splitting with Photocatalytic or Electrolytic Steps," *National Hydrogen Association Conf. & Expo*, Columbia, South Carolina, April **2009**.

43. T-Raissi, A., Fenton, S. "H2A Analysis of the Photocatalytic Sulfur-Ammonia Cycle – Revised Analysis," delivered to TIAX, March **2009**.

44. T-Raissi, A., Taylor, R., Davenport, R. Presentation at the *STCH Meeting*, University of Nevada at Las Vegas, January 22, **2009**.

45. Taylor, R., T-Raissi, A., Davenport, R. Presentation at the *STCH Meeting*, DOE Golden Field Office, October 8-9, **2008**.

46. Taylor, R. and Davenport, R., "Solar Field Configuration for Thermochemical Hydrogen Production with Quantum Boost," presentation at the *WHEC2008 Conference*, Brisbane, Queensland, Australia, 15-19 June **2008**.

47. Taylor, R., Davenport, R., and T-Raissi, A., "Prospects for the Solar Thermochemical Production of Hydrogen from Water," poster presented at the *WHEC2008 Conference*, Brisbane, Queensland, Australia, 15-19 June **2008**.

48. Fenton, S., Huang, C., Muradov, N., and T-Raissi, A., "Flowsheeting a Solar-Driven Sulfur-Ammonia Water Splitting Cycle with $ZnSO_4$-ZnO Sub-Cycle," poster presentation at the *WHEC2008 Conference*, Brisbane, Queensland, Australia, 15-19 June **2008**.

49. Mao, L., Huang, C., Yao, W., T-Raissi, A., and Muradov, N., "Development of High Efficiency Photocatalysts for Solar Hydrogen Production, " presentation at the *WHEC2008 Conference*, Brisbane, Queensland, Australia, 15-19 June **2008**.

50. Mao, L., Huang, C., T-Raissi, A., and Muradov, N., "Zinc Oxide Mediated Thermal Decomposition of Ammonium Sulfate," presentation at the *WHEC2008 Conference*, Brisbane, Queensland, Australia, 15-19 June **2008**.

51. Huang, C., Illiassou, B., Mao, L., T-Raissi, A., Muradov, Z. "Development of Efficient Photocatalysts for Solar Hydrogen Production," *Proc. of 17th World Hydrogen Energy Conference*, 15-19 June **2008**, Brisbane, Australia.

52. T-Raissi, A., Huang, C., Muradov, N.Z., Mao, L., Fenton, S., Yao, W., Block, D.L., Illiassou, B., Taylor, R., and Davenport, R., "Solar-Driven Photocatalytically-Assisted Water Splitting," presentation at the *DOE Hydrogen Program Review Meeting*, 10 June **2008**, Crystal City, VA.

53. Davenport, R., Taylor, R., and T-Raissi, A., "Solar Concentrator Options for a Thermochemical Hydrogen Production Process," presentation at the *ASES SOLAR2008 Conferenc*e, San Diego, CA, 4-8 May **2008**.

54. Huang, C., T-Raissi, A., Fenton, S., Mao, L., and Muradov, N., "A New Family of Solar Metal Sulfate–Ammonia Based Thermochemical Water Splitting Cycles for H_2 Production," presentation at the *ASES SOLAR2008 Conference*, San Diego, CA, 4-8 May **2008**.

55. Taylor, R., Davenport, R., T-Raissi, A. "High Efficiency Solar Production of Hydrogen from Water," *NHA Annual Hydrogen Conference*, April **2008**.

56. T-Raissi, A., Huang, C., Muradov, N. "A New Solar Thermochemical Water Splitting Cycle for Hydrogen Production," *Proc. Int. Symp. on Materials Issues in A Hydrogen Economy*, Richmond, Virginia, Nov., **2007**.

57. Huang, C., Illiassou, B., T-Raissi, A., Muradov, N. "Preparation of High Efficiency Visible Light Activated Pt/CdS Photocatalyst for Solar Hydrogen Production," *Proc. SPIE-2007,* 6650 (Solar Hydrogen & Nanotech II), 665010/1-12, **2007**.

58. Huang, C., Mohajeri, N., Muradov, N., T-Raissi, A. "Solar Thermocatalytic Decomposition of Ammonium Sulfate," *Proc. Solar 2007 Conf.*, Cleveland, OH, **2007**.

59. Huang, C., T-Raissi, A., Muradov, N. "Efficiency of the Sulfur-Ammonia Solar Thermochemical Water Splitting Cycle for the Production of Hydrogen", *Proc. 3rd Int. Symp. on Energy, Information & Cybernetics (EIC),* Orlando, FL, July 18-11, **2007**.

60. T-Raissi, A., et al. *J. Solar Energy Engineering*, 129, 2, **2007**.

6.2 Inventions/Patent Applications

1. Huang, C., T-Raissi, A., Muradov, N.Z. "Solar Metal Sulfate – Ammonia Based Thermochemical Water Splitting Cycle for Hydrogen Production," UCF-645, Patent still pending before USPTO, Utility Patent Application No. 12/267,569, Nov., 8, **2008**.
2. Huang, C., Yao, W., Muradov, N.Z., T-Raissi, A. "Non-Pt Based Pd-Cr_2O_3/CdS Photocatalysts for Solar Photocatalytic Hydrogen Production," Provisional Patent filed March **2009**.
3. Huang, C., Tabatabaie-Raissi, A., Muradov, N.Z. "A Thermochemical Cycle for Production of Hydrogen and/or Oxygen via Water Splitting Processes," *Pub. No.: WO/**2007**/002614 International Application No.: PCT/US2006/024865.*
4. Huang, C., T-Raissi, A., Muradov, N.Z. "Solar Metal Sulfate – Ammonia Based Thermochemical Water Splitting Cycles for Hydrogen Production," *US Provisional Patent, Serial No. 60/986,820*, Nov., **2007**.

7 References

1. T-Raissi, A. “Water Splitting: Thermochemical,” in ENCYCLOPEDIA OF INORGANIC CHEMISTRY, ed. R. A. Scott, John Wiley: Chichester. Published 18 Jan. 2011.
2. T-Raissi, A. “Thermochemical Water-Splitting,” in ENERGY PRODUCTION AND STORAGE – INORGANIC CHEMICAL STRATEGIES FOR A WARMING WORLD, Crabtree, Robert H. 1st edition, John Wiley & Sons - ISBN 978-0-470-74986-9. Sept. 2010.
3. T-Raissi, A., et al. "Solar High-Temperature Water-Splitting Cycle with Quantum Boost," Proceedings of the FY 2009 U.S., Department of Energy (DOE) Hydrogen and Vehicle Technologies Program Annual Merit Review and Peer Evaluation Meeting (AMR), May 18-22, 2009 in Arlington, Virginia.
4. T- Raissi, A., Huang, C., Mao, L., Muradov, N.Z. “A New Solar Metal Sulfate – Ammonia Based Thermochemical Water Splitting Cycle for the Production of Hydrogen,” MATERIALS ISSUES IN A HYDROGEN ECONOMY – PROC. INTERN. SYMP. P. Jena, A. Kandalam, Q. Sun (Editors), World Scientific Publishing Co. Pte. Ltd., 2009, 15-45.
5. www.brightsourceenergy.com/, www.solarreserve.com/
6. Ryan Tanakit, Wesley Luc, J. Talbot, “Electrophoretic Deposition of Cobalt Ferrite and Platinum Cobalt Nanoparticles as Electrocatalysts,” Abstract 2306, for presentation at the 224th ECS Meeting in San Francisco, California (October 27-November 1, 2013)
7. H. Kim, S. Woo, I. Kim and S. Bong, *Abstracts of 218th ECS Meeting*, 2010. Abstract #688. D. Pletcher, and R.I. Urbina, *J. Electroanal. Chem.*, 43, (1997), 137.
8. P. Cox and D. Pletcher, *J. Appl. Electrochem.,* 20 (1990), 549.
9. T. Li, C. Yanhong, and J. Ma, in J.H. Dickerson and A.R. Boccaccini (Ed.), Electrophoretic Deposition of Nanomaterials, Springer, New York, 2012. Also method developed by University of California, San Diego
10. Z. Zi, Y. Sun, X. Zhu, Z. Yang, J. Dai, and W. Song, Journal of Magnetism and Magnetic Materials, 321, 1251-1255 (2009)
11. Wang, W.; Wang, G.; van der Vliet, D.; Chang, K.; Markovic, N.; Stamenkovic, V., Monodisperse Pt3Co nanoparticles as electrocatalyst: the effects of particle size and pretreatment on electrocatalytic reduction of oxygen. Physical Chemistry Chemical Physics. 2010, 12,6877-7296
12. J. Liu, H. Wang, S. Cheng and K.-Y. Chan, Chem.Commuin., (2004), 728
13. P. Dimitrova, K.A. Friedrich, U. Stimming and B. Vogt, Solid State Ionics, 150, (2002), 115
14. TMY Data files for various locations are available from www.nrel.gov
15. R. Adinberg, A. Yogev, and D. Kaftori, “High temperature thermal energy storage an experimental study,” *J. Phys. IV France*, 9, (1999), Pr3-89

8 Acronyms

CTAB	Hexadecyltrimethlyammonium bromide
DOE	U.S. Department of Energy
EDX	Energy-dispersive X-ray spectroscopy
E/M	Electromagnetic
EPD	Electrophoretic deposition
ESC	Electrosynthesis Company, Inc.
FSEC	Florida Solar Energy Center of the University of Central Florida
GC08	Cloth material used as a substrate for depositing catalyst
GRC	Glass-reinforced concrete
H2A	DOE supplied economic model
hv	Photon Energy
HyS	Hybrid Sulfur hydrogen production cycle
IR	Infrared
iR	Electrical resistive losses
LBE	Lead-bismuth eutectic
LHV	Lower Heating Value
LSV	Linear Sweep Voltammetry
M	Molar concentration
MEA	Membrane Electrode Assembly
NIR	Near Infrared
NREL	National Renewable Energy Laboratory
PV	Photovoltaic
RSTOIC	Stoichiometric
SA	Sulfur-Ammonia Thermochemical Water-Splitting Cycle (the cycle being developed)
SAM	NREL Solar Advisor Model
SAIC	Science Applications International Corporation
SEM	Scanning electron microscope
S.G.	Specific Gravity

STCH	Solar Thermochemical Hydrogen Program
TCHEME	Thermochemical Engineering Solutions Company
TES	Thermal Energy Storage
TMY	Typical Meteorological Year
UCSD	University of California, San Diego
UV	Ultraviolet
VIS	Visible

9 Appendix A – Aspen Plus Model Details

Table A.1 Detailed Mass and Energy Balance of the SA plant. (Includes manually torn recycle streams. Energy basis for material streams is that of formation from the constituent elements at their standard state.)

Energy Balance	**In (MW)**	**Mass Balance**	
Low Temperature Reactor	0		**In (kg/sec)**
High Temperature Reactor	99	water feed	20
Mid Temperature Reactor	1499	SULFATE	505
Heat into the Electrolytic Reactor	154	K2SO4	5279
Hydrogen product compressor	6	rank1 [1]	857
water pump	0	rank2 [11]	184
water feed enthalpy	-310	**Total (kg/sec)**	6845
Rankine Cycle 1 pump	14		
Rankine Cycle 2 pump	3		**Out (kg/sec)**
Mid Temperature Reactor Produc	2	O2	18
SULFATE	-6520	H2	2
K2SO4	-25535	SULFATER	505
rank1 [1]	-3286	K2SO4-R	5279
rank2 [11]	-707	rank1 [8]	857
Total (MW)	-34581	rank2 [55]	184
		Total (kg/sec)	6845
	Out (MW)		
Rankine Cycle 1 Turbine	241		
Rankine Cycle 2 Turbine	34		
Hydrogen Product Separator	21		
Condenser in Rankine Cycle 1	999		
Condenser in Rankine Cycle 2	162		
Electrolytic Reactor Heat Loss	21		
Oxygen Product	-19		
Hydrogen Product	9		
SULFATER	-6520		
K2SO4-R	-25535		
rank1 [8]	-3286		
rank2 [55]	-707		
Total (MW)	-34580		
difference	1		
difference (%)	0.003%		

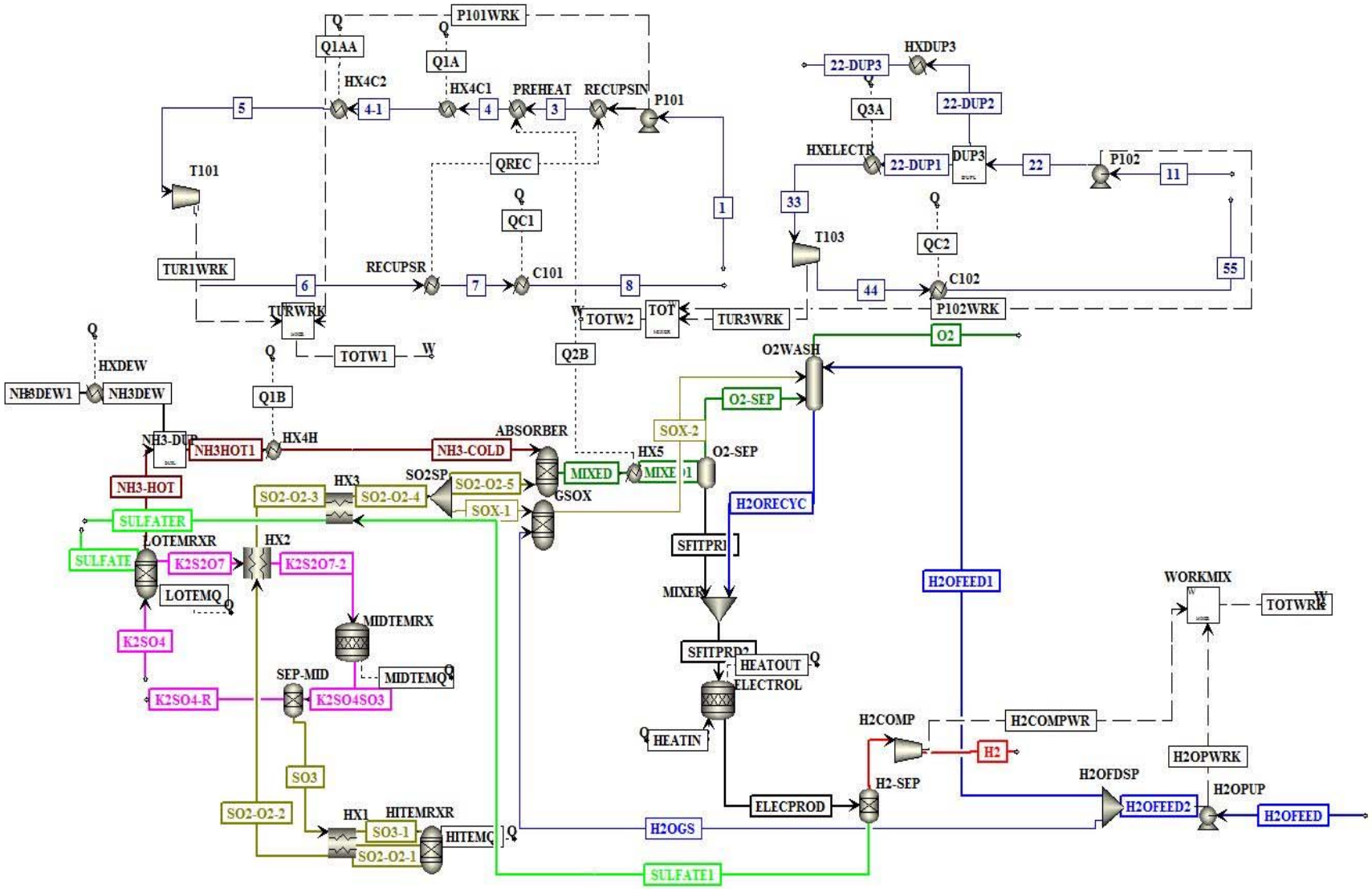

Figure A.1. Full Aspen Plus Process Flow Diagram for SA Cycle